NASA CR 174966

Modal Forced Vibration Analysis of Aerodynamically Excited Turbosystems

V. Elchuri

(NASA-CR-174966) MODAL FORCED VIBRATION ANALYSIS OF AERODYNAMICALLY EXCITED TURBOSYSTEMS Final Report (Aerostructures) 133 p CSCI 20K G3/39

N89-18696

Unclas 0192934

Aerostructures, Inc.
1225, Jeff. Davis Hwy., Suite 512
Arlington, VA 22202

FINAL REPORT

CONTRACT NAS3-24387

NATIONAL AERONAUTICS and SPACE ADMINISTRATION
Lewis Research Center
Cleveland, OH 44135

July 1988

NASA CR 174966

Modal Forced Vibration Analysis of Aerodynamically Excited Turbosystems

V. Elchuri

Aerostructures, Inc.
1225, Jeff. Davis Hwy., Suite 512
Arlington, VA 22202

FINAL REPORT

CONTRACT NAS3-24387

NATIONAL AERONAUTICS and SPACE ADMINISTRATION
Lewis Research Center
Cleveland, OH 44135

July 1985

SUMMARY

Theoretical aspects of a new capability to determine the vibratory response of turbosystems subjected to aerodynamic excitation are presented.

Turbosystems such as advanced turbopropellers with highly swept blades, and axial-flow compressors and turbines can be analyzed using this capability. The capability has been developed and implemented in the April 1984 release of the general purpose finite element program NASTRAN.

The dynamic response problem is addressed in terms of the normal modal coordinates of these tuned rotating cyclic structures. Both rigid and flexible hubs/disks are considered. Coriolis and centripetal accelerations, as well as differential stiffness effects are included.

Generally non-uniform steady inflow fields and uniform flow fields arbitrarily inclined at small angles with respect to the axis of rotation of the turbosystem are considered as the sources of aerodynamic excitation. The spatial non-uniformities are considered to be small deviations from a principally uniform inflow. Subsonic and supersonic relative inflows are addressed, with provision for linearly interpolating transonic airloads.

A stand-alone pre-processor program, independent of NASTRAN, has been additionally developed to generate the vibratory airloads on the blades of these turbosystems.

Both NASTRAN and pre-processor capabilities are operational on the CRAY 1-S computer system at NASA's Lewis Research Center.

The work was conducted under Contract NAS3-24387 from NASA LeRC, Cleveland, Ohio, with Mrs. Marsha Nall as the Program Monitor.

ACKNOWLEDGEMENT

The author takes this opportunity to commend the superb effort of Dr. P.R. Pamidi of RPK Corporation in implementing the developments presented in this report in NASTRAN on the CRAY 1-S computer system at NASA LeRC.

Technical cooperation extended by Mrs. Marsha Nall and Drs. Bob Kielb and Kris Kaza of NASA LeRC are gratefully appreciated.

Secretarial assistance provided by Mrs. Nancy Smith in the preparation of this report is sincerely appreciated.

TABLE OF CONTENTS

SECTION	TITLE	PAGE
	SUMMARY	i
	ACKNOWLEDGEMENT	iii
	LIST OF TABLES	vii
	LIST OF FIGURES	viii
1.	INTRODUCTION	1
2.	MATHEMATICAL FORMULATIONS	3
2.1	Problem Description	3
2.2	Approach	3
2.3	Coordinate Systems	9
2.4	Degrees of Freedom	14
2.5	Equations of Motion and Their Solution	15
3.	APPLIED OSCILLATORY AIRLOADS	25
3.1	General	25
3.2	Gust Amplitudes and Frequencies of Oscillatory Relative Inflow	26
3.2.1	Uniform Inflow	30
3.2.2	Non-Uniform Inflow	31
3.3	Grid Point Loads From Ocillatory Pressure Distribution Along Chord	34
4.	APPLICATION EXAMPLES	36
4.1	General	36
4.2	Examples	36
4.3	Structural and Aerodynamic Models	40
4.4	Boundary Conditions	40

TABLE OF CONTENTS (contd.)

SECTION	TITLE	PAGE
4.5	Applied Oscillatory Airloads	40
4.6	Analysis Steps for Each Operating Condition	43
5.	RESULTS AND DISCUSSION	46
5.1	General	46
5.2	Differential Stiffness	46
5.3	Natural Frequencies and Mode Shapes	80
5.4	Aeroelastic Stability	80
5.5	Vibratory Response to Aerodynamic Excitation	82
6.	CONCLUSIONS	89
7.	RECOMMENDATIONS	90
APPENDIX A	SWEEP EFFECTS IN SUPERSONIC AIRLOADS DUE TO OSCILLATORY BLADE MOTIONS	91
A.1	General	91
A.2	Definitions	94
A.3	Blade Degrees of Freedom	95
A.4	Normal Displacement, Downwash and Pressure Distribution in Terms of Chordwise Aerodynamic Modes	96
A.5	Generalized Airforce Matrices for Chordwise Aerodynamic Modes	99

TABLE OF CONTENTS (contd.)

SECTION	TITLE	PAGE
A.6	Transformation Between Aerodynamic and Structural Modal Coordinates	100
A.7	Generalized Airforce Matrices for Chordwise Structural Modes	103
A.8	Blade Generalized Airforce Matrix	104
APPENDIX B	CHORDWISE WEIGHTING MATRICES (SUPERSONIC)	105
APPENDIX C	AERODYNAMIC EXCITATION PARAMETERS	109
C.1	General	109
C.2	Inter-Blade Phase Angles	109
C.3	Rigid Hub/Disk, Uniform Inflow	110
C.4	Rigid Hub/Disk, Non-Uniform Inflow	112
C.5	Flexible Hub/Disk, Uniform Flow	113
C.6	Flexible Hub/Disk, Non-Uniform Inflow	114
	REFERENCES	116
	SYMBOLS	118

LIST OF TABLES

TABLE	TITLE	PAGE
4.1	Operating Conditions for SR-3 and SR-5 Examples	37
5.1	Natural Frequencies of SR-3 and SR-5 Turboprops	47
5.2	Comparison of Excitation and Modal Frequencies	85

LIST OF FIGURES

FIGURE	TITLE	PAGE
2.1	Advanced Turboprop in a Generally Non-Uniform Steady Inflow Field	4
2.2	NASTRAN Aerodynamic Model of Turboprop Blade for 2-D Cascade Theories (Ref. 6)	8
2.3	Coordinate Systems	10
2.4	Turboprop Axis Inclination Angle and Tunnel Coordinate System Orientation in Uniform Inflow Case	12
2.5	Cyclic Sector and Side Numbering Convention	16
2.6	Overall Flowchart of Modal Forced Vibration Analysis Capability for Aerodynamically Excited Turbosystems	23
3.1	Inlet Velocity Triangles for Determining Oscillatory Relative Inflow	27
3.2	Transformation of Oscillatory Pressure Distribution to Loads at Structural Grid Points	35
4.1	SR-3 Strain Gage Locations (Suction Side)	38
4.2	SR-5 Strain Gage Locations (Suction Side)	39
4.3	NASTRAN Structural and Aerodynamic Models of SR-3	41
4.4	NASTRAN Structural and Aerodynamic Models of SR-5	42
4.5	Overall Flowchart of Analyses Steps to Conduct Each of the SR-3 and SR-5 Examples	44
5.1	SR-3 Differential Stiffness Analysis-- Linear Solution	48
5.2	SR-3 Differential Stiffness Analysis-- Non-Linear Solution	49
5.3	SR-3 Mode 1	50
5.4	SR-3 Mode 2	51

LIST OF FIGURES

FIGURE	TITLE	PAGE
5.5	SR-3 Mode 3	52
5.6	SR-3 Mode 4	53
5.7	SR-3 Mode 5	54
5.8	SR-3 V-g, V-f Curves--Test Reading No. 190	55
5.9	SR-3 V-g, V-f Curves--Test Reading No. 273	56
5.10	SR-3 V-g, V-f Curves--Test Reading No. 277	57
5.11	SR-3 V-g, V-f Curves--Test Reading No. 278	58
5.12	SR-3 One-Per-Rev Stress Comparison--Test Reading No. 190	59
5.13	SR-3 One-Per-Rev Stress Comparison--Test Reading No. 273	60
5.14	SR-3 One-Per-Rev Stress Comparison--Test Reading No. 277	61
5.15	SR-3 One-Per-Rev Stress Comparison--Test Reading No. 278	62
5.16	SR-5 Differential Stiffness Analysis--Linear Solution	63
5.17	SR-5 Differential Stiffness Analysis--Non-Linear Solution	64
5.18	SR-5 Mode 1	65
5.19	SR-5 Mode 2	66
5.20	SR-5 Mode 3	67
5.21	SR-5 Mode 4	68
5.22	SR-5 Mode 5	69
5.23	SR-5 V-g, V-f Curves--Test Reading No. 8508	70
5.24	SR-5 V-g, V-f Curves--Test Reading No. 8511	71

LIST OF FIGURES

FIGURE	TITLE	PAGE
5.25	SR-5 V-g, V-f Curves--Test Reading No. 8607	72
5.26	SR-5 V-g, V-f Curves--Test Reading No. 8610	73
5.27	SR-5 V-g, V-f Curves with Refined Reduced Frequency Range (.10-.30)--Test Reading No. 8508	74
5.28	SR-5 V-g, V-f Curves with Refined Reduced Frequency Range (.10-.30)--Test Reading No. 8511	75
5.29	SR-5 One-Per-Rev Stress Comparison-- Test Reading No. 8508	76
5.30	SR-5 One-Per-Rev Stress Comparison-- Test Reading No. 8511	77
5.31	SR-5 One-Per-Rev Stress Comparison-- Test Reading No. 8607	78
5.32	SR-5 One-Per-Rev Stress Comparison-- Test Reading No. 8610	79
5.33	SR-3 One-Per-Rev Calculated Stress Response Comparison Between Cases	86
5.34	SR-5 One-Per-Rev Calculated Stress Response Comparison Between Cases	87
A.1	Some Definitions for Swept Blade Aerodynamics	92
A.2	Chordwise Aerodynamic Modes	93

1. INTRODUCTION

In a series of related efforts, NASA's Lewis Research Center has sponsored the development of a number of analytical capabilities addressing the static and dynamic problems of axial-flow turbomachines. To benefit from the state-of-the-art structural modelling and analyses techniques, these analytical developments have been implemented in the general purpose finite element program NASTRAN. These additional capabilities in NASTRAN, based on a unified approach to representing and integrating the structural and aerodynamic aspects of the turbomachinery problems, are listed below:

1. Static aerothermoelastic design/analysis of axial-flow compressors (Refs. 1-3),

2. Modal flutter analysis of axial-flow turbomachines (Refs. 1-3),

3. Forced vibration analysis of rotating cyclic structures, direct approach (Refs. 4,5), and

4. Modal flutter analysis of advanced turboprops with highly swept blades (Refs. 6,7).

The new capability discussed in this report for modal forced vibration analysis of aerodynamically excited turbosystems,

1. extends the direct (as compared to modal) approach forced vibration analysis capability listed above to treat the

dynamic response problem in terms of natural modal coordinates of the rotating cyclic structure of the turbosystem,

2. draws upon, and extends, the turboprop flutter analysis capability listed above for the generation of reactionary aerodynamic forces due to the vibratory motion of the turbosystem blades, and

3. requires the specification of imposed oscillatory airloads on the turbosystem. (As per NASA's requirements, the generation of oscillatory airloads for the purposes of the present contract has been accomplished by the development of an independent pre-processor program discussed in detail in Ref. 8 and briefly in Section 3 of this report.)

Mathematical description of the problem and its solution are presented in Section 2.

Application examples on two advanced turboprops at various operating conditions are given in Section 4.

Section 5 presents and discusses the results of Section 4 examples. Conclusions and recommendations are reported in Sections 6 and 7, respectively.

2. MATHEMATICAL FORMULATIONS

2.1 PROBLEM DESCRIPTION

Figure 2.1 shows a single-rotation advanced turboprop, as an example of turbosystems, operating in a generally non-uniform steady inflow field.

Although the absolute inflow field does not change with time, the rotation of the turboprop results in velocities with oscillatory components relative to the blades. Relative velocities with harmonic components at the rotational frequency also exist in uniform flow fields when the turboprop axis of rotation is misaligned with the absolute flow direction.

Given such operating conditions, it is desired to,

1. determine the oscillatory loading distributions over the blades of the turboprop at various excitation frequencies, and

2. determine the resulting vibratory response (displacements, stresses, etc.) of the turboprop.

2.2 APPROACH

Due to its eventual implementation as part of the Bladed Shrouded Disks Computer Program in NASTRAN at NASA LeRC, the approach adopted for the formulation and solution of the above

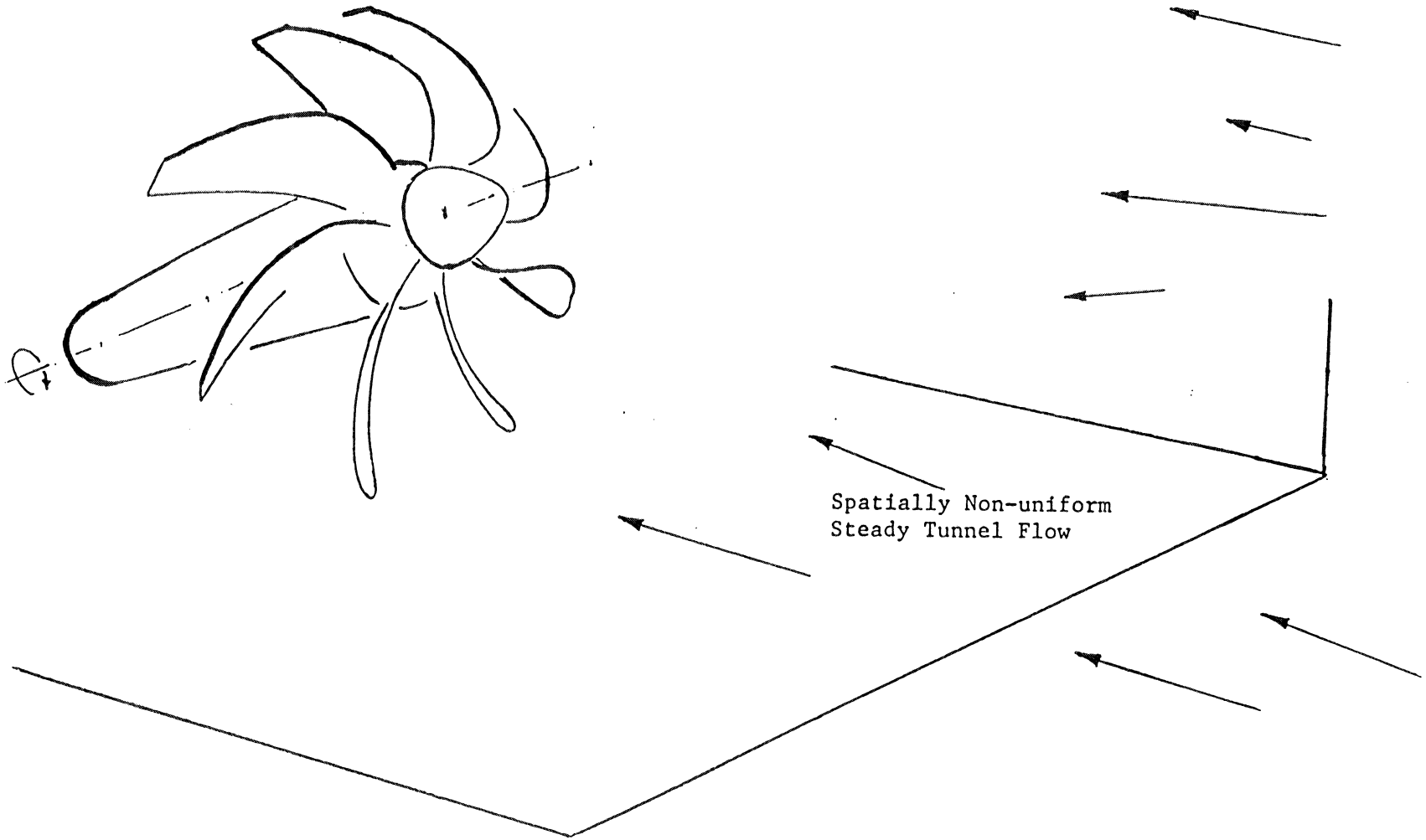

Figure 2.1 Advanced Turboprop in a Generally Non-Uniform Steady Inflow Field

problem is derived from those described in Refs. 4 and 6.

The following structural and aerodynamic aspects are considered in the theoretical development:

Structural Aspects

1. Structural representation

   - Structures of turbosystems are treated as tuned cyclic structures with identical mass, stiffness, damping, and constraint properties for all cyclic sectors. The structural modelling capabilities of NASTRAN for rotationally cyclic structures are admitted.

2. Hub flexibility in relation to that of blades

   - A relatively rigid hub effectively decouples the structural behavior of the blades, any one of which can then be modelled as an independent structural member coupled only aerodynamically with the other blades of the turboprop.

   - A hub of stiffness comparable to that of blades structurally couples the blades, in addition to their aerodynamic coupling. The structural behavior of the multi-bladed turboprop as a whole, as opposed to that of an individual blade, then influences the dynamic response of the turboprop. From a structural modelling viewpoint, however, with the use of analysis invoking

cyclic symmetry features (Ref. 4), it still suffices to model only a one-bladed segment of the turboprop.

3. Differential (or incremental) stiffness

   - The steady state loads, particularly centrifugal loads, acting on the relatively thin blades of advanced turbopropellers noticeably affect the geometry and effective stiffness of the blades. This, in turn, alters the relative inflow conditions at the blade leading edge, and also influences the natural frequencies of the turbopropeller blades at any operating condition. In general, the significance of the differential stiffness effects decreases with decreased rotational speed and increased elastic stiffness of the structure.

4. Coriolis and centripetal acceleration effects

   - These effects are present during vibrations of rotating turboprops, and are accounted for in the forced vibration analysis capability of the Bladed Disks Computer Program.

5. Use of normal modes of the turboprop in formulating and solving the dynamic response problem

   - The normal modes of tuned cyclic turbosystems can be grouped in mutually independent families corresponding to permissible circumferential harmonic indices. Hence, the total response of the turbosystem can be obtained by

combining the mutually independent responses for each of the applicable circumferential harmonics.

Aerodynamic Aspects

1. Aerodynamic modelling

   - This is essentially dictated by the unsteady aerodynamic theories used to determine the unsteady blade loading distribution. The Bladed Disks Computer Program presently utilizes two-dimensional cascade aerodynamics in a strip theory manner. The blade model, accordingly, is a series of chordwise strips stacked spanwise to cover the entire blade surface as shown in (Figure 2.2).

2. Two-dimensional cascade aerodynamics for oscillatory blade motion

   - Subsonic and supersonic aerodynamic routines, currently part of the Bladed Disks Computer Program, with modifications to account for blade sweep, if present, are used to generate the reactionary aerodynamic blade loading distributions.

3. Two-dimensional cascade aerodynamics for oscillatory relative inflow

   - Versions of subsonic and supersonic routines capable of handling oscillatory relative inflow conditions are used to generate the imposed aerodynamic loads on turbosystem

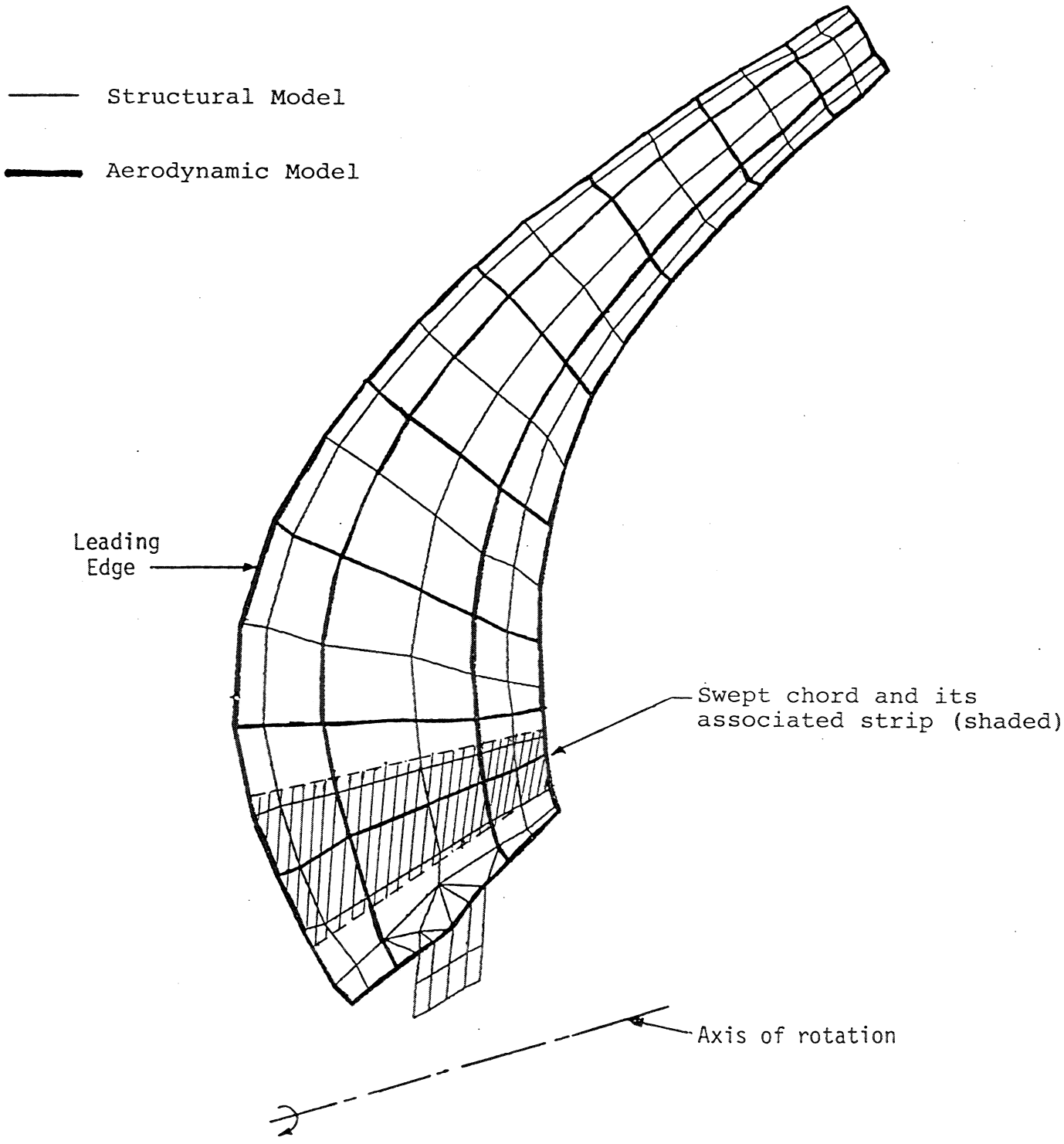

Figure 2.2 NASTRAN Aerodynamic Model of Turboprop Blade for 2-D Cascade Theories (Ref. 6)

blades.

4. Transonic aerodynamics

   - For both oscillatory blade motion and oscillatory relative inflow conditions, in the absence of corresponding two-dimensional transonic aerodynamic theories, the transonic blade loads are obtained by interpolating between subsonic and supersonic loads. For transonic relative Mach numbers at blade tip, the subsonic loads are extrapolated.

5. Causes of aerodynamic excitation

   - These are as described in Section 2.1, Problem Description.

6. Aeroelastic stability at a given operating condition

   - To ascertain that the dynamic response calculations are carried out at aeroelastically stable operating conditions, the modal flutter analysis capability of the present Bladed Disks Computer Program for advanced turbopropellers (Refs. 6 and 7) is used.

2.3 COORDINATE SYSTEMS

In order to conveniently pose and solve the aerodynamically forced vibration problem of turbosystems, a number of coordinate systems have been defined. Figure 2.3 illustrates these

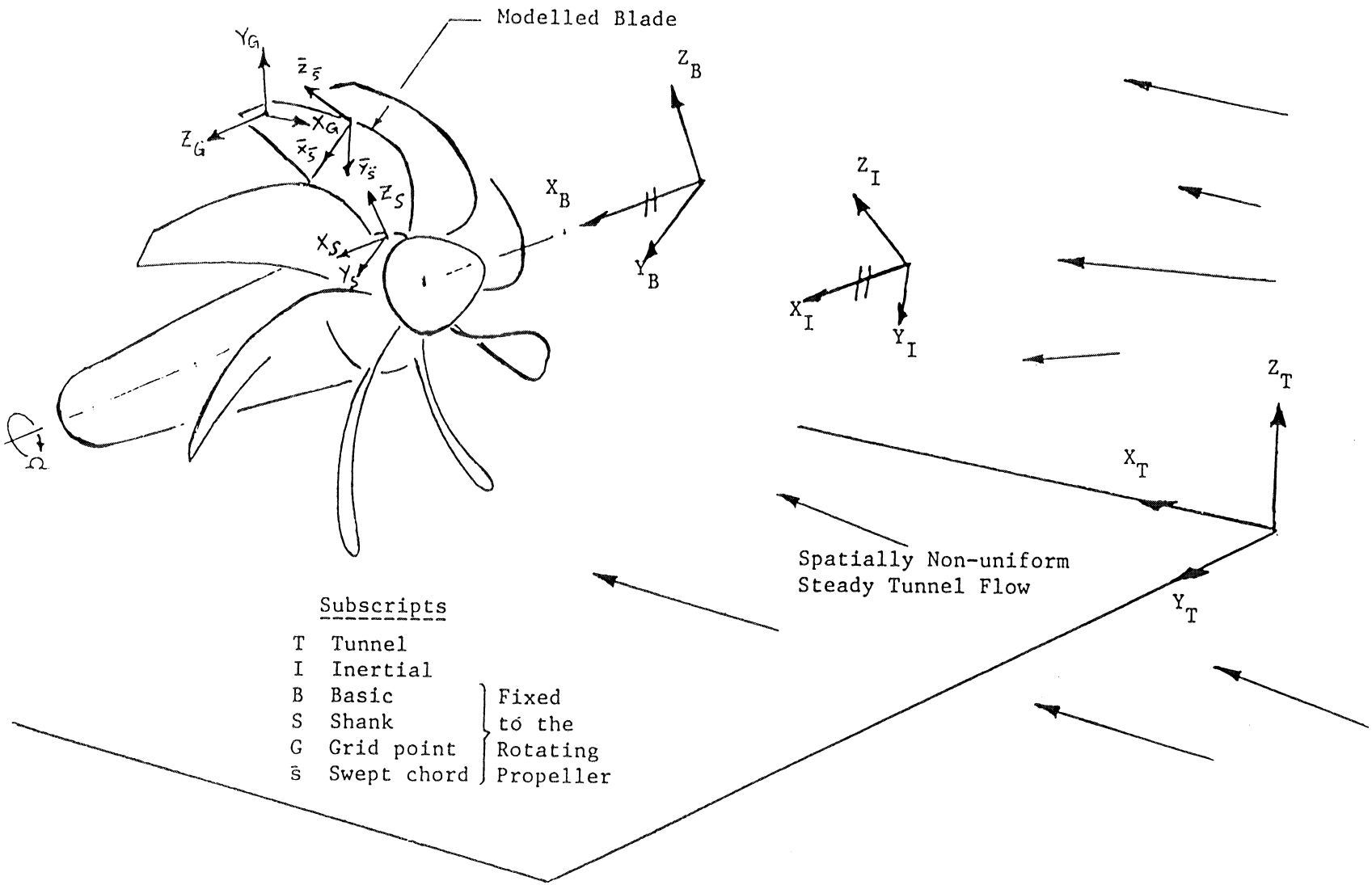

Figure 2.3 Coordinate Systems

coordinate systems for an advanced turbopropeller with its axis of rotation mounted at an angle with respect to the tunnel mean flow.

Each of these coordinate systems is described as follows:

- $X_T Y_T Z_T$ Tunnel coordinate system

  * This is defined to conveniently specify the velocity components of the spatially non-uniform tunnel free stream. It can be suitably oriented based on the available tunnel data. In the special case of aerodynamic excitation in uniform inflow, the tunnel coordinate system is oriented such that the $X_T Z_T$ plane is parallel to the $X_I Z_I$ plane of the inertial coordinate system as shown in Figure 2.4. The origin of the $X_T Y_T Z_T$ system is arbitrarily located. The inclination angle of the turbosystem axis of rotation with respect to the tunnel flow also lies in a plane parallel to $X_I Z_I$ plane. The uniform flow is directed along $+X_T$ axis.

- $X_I Y_I Z_I$ Inertial coordinate system

  * In the present problem, this coordinate system is used to relate the quantities in the tunnel and the basic coordinate systems. The orientation of this coordinate system is completely arbitrary except for the X_I axis to be parallel to, and in the direction of, X_B axis of the basic coordinate system described next. The zero

NOTES

1. Planes $Z_1Z_2Z_3$ and X_TZ_T need only be parallel to X_IZ_I
2. X_I axis is parallel to Z_3Z_2
3. X_T axis is parallel to Z_1Z_2
4. Uniform Inflow is along $+X_T$

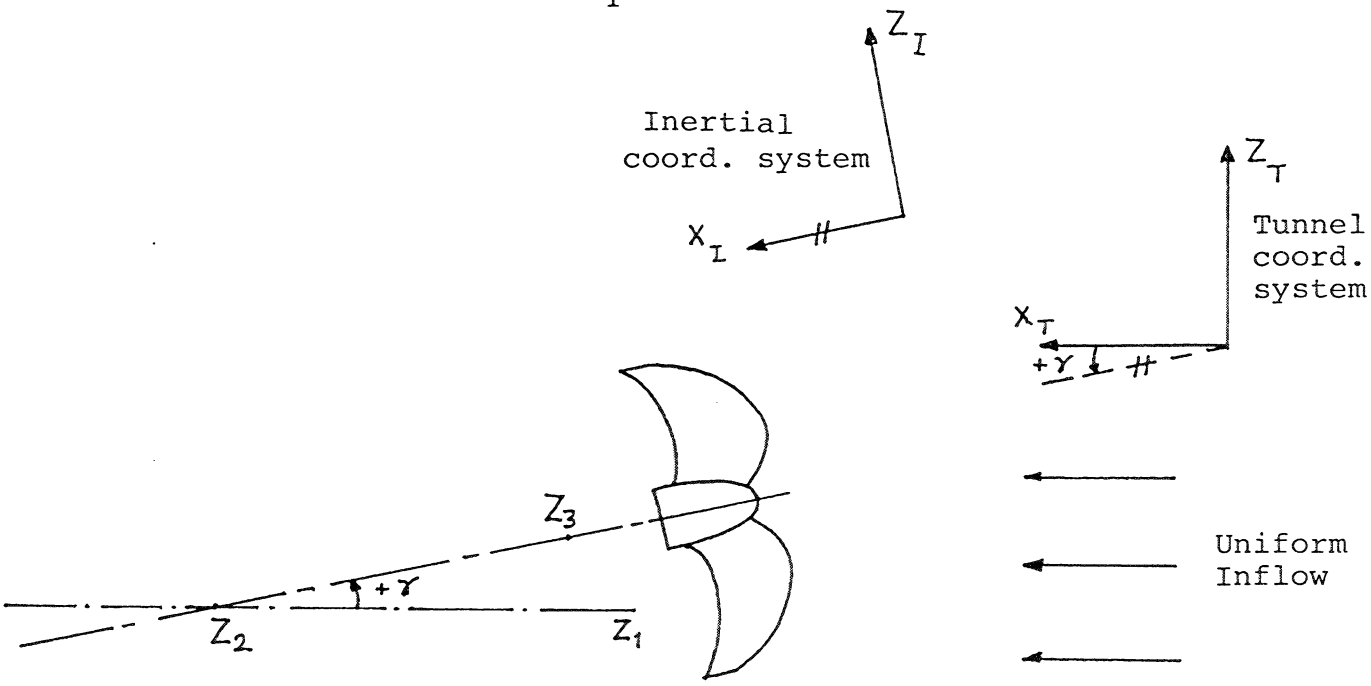

Figure 2.4 Turboprop Axis Inclination Angle and Tunnel Coordinate System Orientation in Uniform Inflow Case

reference for time/phase measurements is defined when the inertial and the basic coordinate systems are parallel.

All of the following NASTRAN coordinate systems are fixed to the rotating turbosystem.

- $X_B Y_B Z_B$ Basic coordinate system

  * This coordinate system has its X_B axis coincident with the turbosystem axis of rotation, and directed aftward. Location of the origin is arbitrary. The $X_B Z_B$ plane contains (approximately) the maximum planform of the modelled blade. The definition of this coordinate system is consistent with the theoretical developments of the 2-d cascade unsteady aerodynamics presently incorporated in the Bladed Disks Computer Program (Ref. 6).

- $X_S Y_S Z_S$ (Blade) shank-fixed coordinate system

  * The principal advantage of this shank-fixed coordinate system is in modelling changes in the blade setting angles by a simple 3 x 3 transformation matrix relating to the basic coordinate system. Z_S coincides with the blade shank axis. The definition of the coordinate system otherwise is arbitrary.

- $X_G Y_G Z_G$ Grid point location and displacement coordinate systems

* Any number of such rectangular, cylindrical, or spherical coordinate systems can be completely arbitrarily defined to locate grid points of the NASTRAN model, as well as request output at these grid points. All of the $X_G Y_G Z_G$ coordinate systems used for output requests collectively form the NASTRAN global coordinates system.

- $\bar{x}_{\bar{s}} \bar{y}_{\bar{s}} \bar{z}_{\bar{s}}$ Internally generated coordinate system on swept chord $\bar{s}$

  * This coordinate system is generated within the present Bladed Disks Computer Program, and is used to define flow and motion properties for the unsteady aerodynamic theories on a given swept chord $\bar{s}$. It is located at the blade leading edge with the $\bar{x}_{\bar{s}}$ directed aftward along the chord $\bar{s}$. $\bar{y}_{\bar{s}}$ is defined normal to the blade local mean surface.

2.4 DEGREES OF FREEDOM

The total translational and rotational displacements at any fixed point of the rotating and vibrating turobsystem, expressed in body-fixed coordinate systems, consist of

- steady state components due to the steady airloads and centrifugal loads, and

- vibratory components due to the vibratory excitation,

superposed on the steady displacements.

The aerodynamic vibratory response problem of the turbosystem is posed herein in terms of the vibratory components of total displacements.

2.5 EQUATIONS OF MOTION AND THEIR SOLUTION

For an N-bladed tuned turbosystem, with structural coupling between blades via a relatively flexible hub, the equations of forced motion can be written as (Ref. 4)

$$[M^n]\{\ddot{u}^n\} + \left[[B^n]^{visc.} + 2\Omega[B_1^n]\right]\{\dot{u}^n\}$$

$$+ \left[[K^n]^{elas.} + [K^n]^{diff.} - \Omega^2[M_1^n]\right]\{u^n\}$$

$$- [Q^n]\{u^n\} = \{P^n\}^{aero.}, \qquad (1)$$

and

$$\{u^n\}_{side\ 2} = \{u^{n+1}\}_{side\ 1}, \quad n = 1, 2, \ldots, N. \qquad (2)$$

The forcing term on the right hand side of equation (1) is entirely due to aerodynamic excitation. Cyclic sector numbers and their sides referred to in equation (2) are illustrated in Figure 2.5 .

In seeking solutions for the vibratory displacements u^n , for all n , based on the qualitative and quantitative nature of

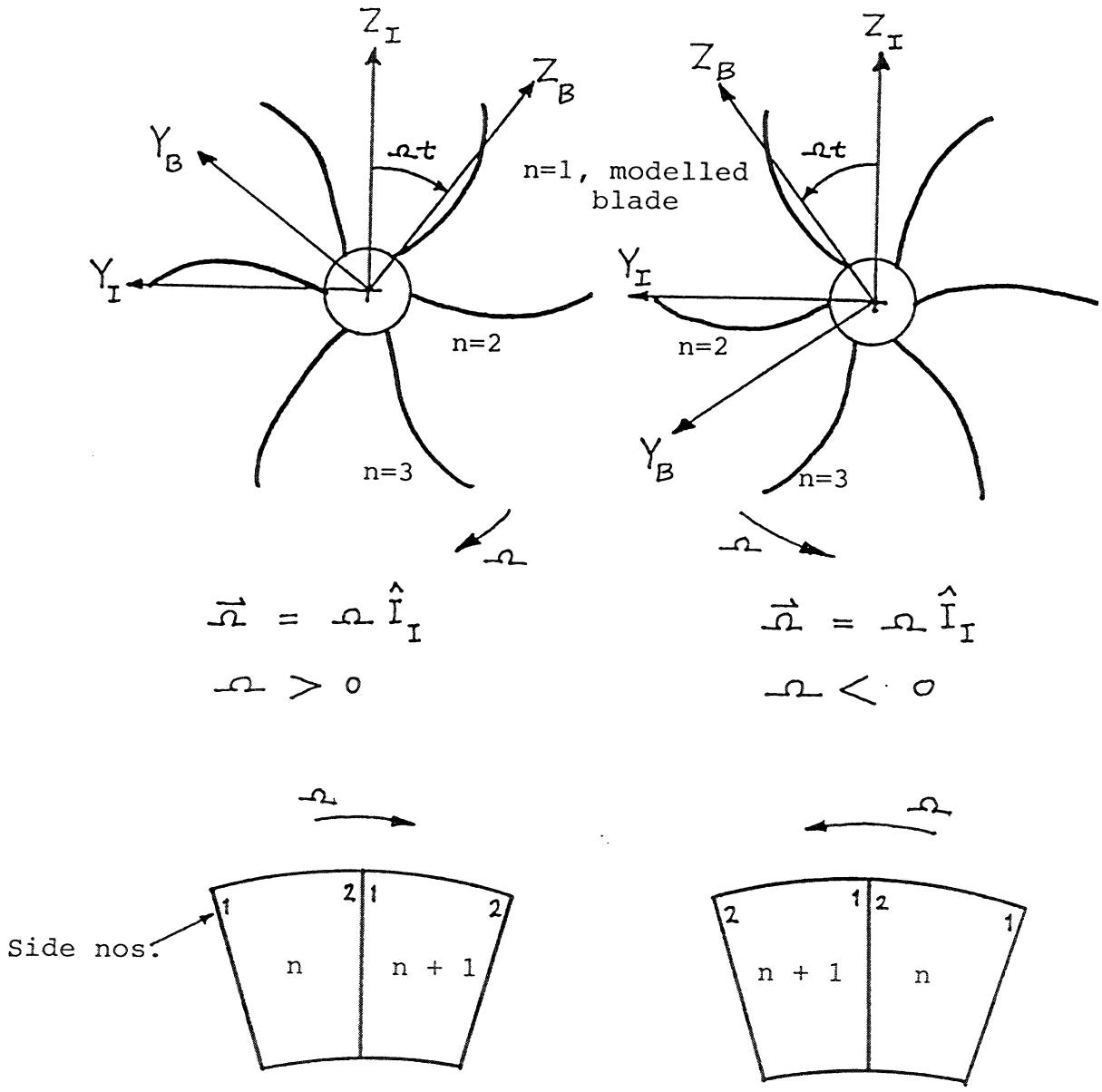

NOTES

1. $\vec{\Omega}$ is the angular velocity of the $X_B Y_B Z_B$ coordinate system w.r.t. the $X_I Y_I Z_I$ coord.system.
2. Modelled sector is always n=1 st. sector.
3. Sector, and side numbers within a sector, increase in the direction of $|\Omega t|$.

Figure 2.5 Cyclic Sector and Side Numbering Convention

the right hand side forcing functions, the following steps, applicable to tuned cyclic structures with rotational cyclic symmetry, are considered.

1. The displacements u^n (and the loads P^n) can be written as (Ref. 4)

$$\{u^n\} = \{\bar{u}^0\} + \sum_{k=1}^{k_L} \left[\{\bar{u}^{kc}\} \cos(\overline{n-1}\, ka) + \{\bar{u}^{ks}\} \sin(\overline{n-1}\, ka) \right] + (-1)^{n-1} \{\bar{u}^{N/2}\} . \quad (3)$$

This is a standing wave representation wherein the coefficients $\bar{u}^0$, $\bar{u}^{kc}$, $\bar{u}^{ks}$ and $\bar{u}^{N/2}$ are, in general, functions of time or frequency. For a given circumferential harmonic index k, by defining appropriate relations between $\bar{u}^{kc}$ and $\bar{u}^{ks}$ the above equation can be transformed to a travelling wave form (Appendix C). The constants k_L and a are given by,

$$\left.\begin{aligned} k_L &= (N-1)/2 \quad , \quad N \text{ odd} , \\ &= (N-2)/2 \quad , \quad N \text{ even} , \end{aligned}\right\} \quad (4)$$

and

$$a = 2\pi / N .$$

2. For a given circumferential harmonic index ,

$$\{u^{n,k}\} = \{\bar{u}^{kc}\} \cos(\overline{n-1}\, ka) + \{\bar{u}^{ks}\} \sin(\overline{n-1}\, ka) . \quad (5)$$

3. With the use of inter-segment compatibility constraint conditions (equation 2)

$$\{\bar{u}^{kc}\} = [G_{ck}(k)]\{\bar{u}^{K}\}, \text{ and} \qquad (6)$$

$$\{\bar{u}^{ks}\} = [G_{sk}(k)]\{\bar{u}^{K}\}, \qquad (7)$$

where $\bar{u}^{K}$ is an independent displacement vector consisting of $\bar{u}^{kc}$ and $\bar{u}^{ks}$ degrees of freedom from the interior and side 1 of a cyclic sector. The transformations G_{ck} and G_{sk} are functions of the circumferential harmonic k, and express the side 2 degrees of freedom in terms of those on side 1.

4. Equation (5) can then be written as

$$\{u^{n,k}\} = \left[\cos(\overline{n-1}\,ka)\,[G_{ck}] + \sin(\overline{n-1}\,ka)\,[G_{sk}]\right]\{\bar{u}^{K}\}. \qquad (8)$$

5. The real eigenvalue problem, for a given k, can then be stated from equation (1) as

$$\left[-\omega^2[\bar{M}^{K}] + [\bar{K}^{K}]\right]\{\bar{\bar{u}}^{K}\} = 0, \qquad (9)$$

where

$$\{\bar{u}^{K}\} = \{\bar{\bar{u}}^{K}\}\,e^{i\omega t}, \qquad (10)\ \text{contd.}$$

$$\left.\begin{aligned} [\bar{M}^K] &= [G_{ck}]^T [M^n][G_{ck}] + [G_{sk}]^T [M^n][G_{sk}], \text{ and} \\ [\bar{K}^K] &= [G_{ck}]^T [K^n][G_{ck}] + [G_{sk}]^T [K^n][G_{sk}]. \end{aligned}\right\} \quad (10)$$

6. The eigenvectors $[\bar{\phi}^K]$ obtained from the solution of equation (9), can be used to introduce the modal coordinates $\{\bar{\xi}^K\}$ as

$$\{\bar{u}^K\} = [\bar{\phi}^K]\{\bar{\xi}^K\}. \quad (11)$$

7. The modal equations of forced motion of the turbosystem, for a given circumferential harmonic index k, can then be written from equation (1)

$$[\bar{\bar{M}}^K]\{\ddot{\bar{\xi}}^K\} + [\bar{\bar{B}}^K]\{\dot{\bar{\xi}}^K\} + [\bar{\bar{K}}^K]\{\bar{\xi}^K\} - [\bar{\bar{Q}}^K]\{\bar{\xi}^K\} = [\bar{\phi}^K]^T\{\bar{P}^K\}, \quad (12)$$

where

$$[\bar{\bar{M}}^K] = [\bar{\phi}^K]^T [\bar{M}^K][\bar{\phi}^K], \quad (13) \text{ contd.}$$

$$
\left.
\begin{aligned}
[\bar{\bar{B}}^K] &= [\bar{\phi}^K]^T [\bar{B}^K][\bar{\phi}^K] \quad , \\
[\bar{\bar{K}}^K] &= [\bar{\phi}^K]^T [\bar{K}^K][\bar{\phi}^K] \quad , \\
[\bar{\bar{Q}}^K] &= [\bar{\phi}^K]^T [\bar{Q}^K][\bar{\phi}^K] \quad , \\
[\bar{Q}^K] &= [G_{ck}]^T [Q^n][G_{ck}] + [G_{sk}]^T [Q^n][G_{sk}] \quad ,
\end{aligned}
\right\} \quad (13)
$$

and

$$
\{\bar{P}^K\} = [G_{ck}]^T \{\bar{P}^{kc}\} + [G_{sk}]^T \{\bar{P}^{ks}\} \quad .
$$

8. For a given circumferential harmonic index k, $\bar{P}^{kc}$ and $\bar{P}^{ks}$ are the circumferential harmonic components of the total external excitation. Such excitation due to aerodynamic sources is discussed in Section 3.

9. The generalized oscillatory aerodynamic reaction matrix $\bar{\bar{Q}}^K$ can be written as

$$
[\bar{\bar{Q}}^K] = [\bar{\phi}^{kc}]^T [Q^n][\bar{\phi}^{kc}] + [\bar{\phi}^{ks}]^T [Q^n][\bar{\phi}^{ks}] \quad , \quad (14)
$$

where

$$
[\bar{\phi}^{kc}] = [G_{ck}][\bar{\phi}^K] \quad , \quad (15) \text{ contd.}
$$

and

$$[\bar{\phi}^{ks}] = [G_{sk}][\bar{\phi}^{K}] \qquad (15)$$

are the 'cosine' and 'sine' component mode shapes of eigenvectors $\bar{\phi}^{K}$ Equation (14) is rewritten as

$$[\bar{\bar{Q}}^{K}] = [Q^{c}_{ii}] + [Q^{s}_{ii}] \qquad (16)$$

For turbosystem structures with flexible hub/disk,

a) Q^{c}_{ii} and Q^{s}_{ii} exist when the circumferential harmonic index $k \neq 0$ and $\neq N/2$ when N, the total number of cyclic segments in the structure, is even, and

b) only Q^{c}_{ii} exists when k = 0 or N/2, N even.

For turbosystem structures with rigid hub/disk, each cyclic segment of the structure behaves structurally independent of its adjacent segments. Degrees of freedom at segment boundaries are completely constrained to zero. The only possible structural modes are those akin to k = 0 modes with fixed inter-segment boundaries. Only Q^{c}_{ii} exists.

Derivation of Q_{ii} is discussed in detail in Appendix A. Supersonic chords are considered as examples. The derivation of Q_{ii} for subsonic chords alone was discussed in Ref. 6. Q^{c}_{ii} and Q^{s}_{ii} are generated, in turn, by considering $\bar{\phi}^{kc}$ and $\bar{\phi}^{ks}$, in turn, to represent the structural modes in

equations (A29) and (A31) of Appendix A.

10. Equation (12) can now be solved for $\bar{\xi}^K$. Substitution in equation (11), and equation (8) yields $u^{n,k}$.

11. Repeating steps 2 through 10 for all applicable circumferential harmonic indices, and substitution in equation (3), result in u^n for all n .

12. Other dynamic responses such as stresses, etc., can be obtained for all sectors of the turbosystem by current NASTRAN procedures.

The procedure described above for the solution of circumferential harmonic components of dynamic response, for a given circumferential harmonic index, has been implemented in the April 1984 release of NASTRAN on the CRAY 1-S computer system at NASA LeRC (Ref. 9).

An overall flowchart of the solution procedure is shown in Figure 2.6 .

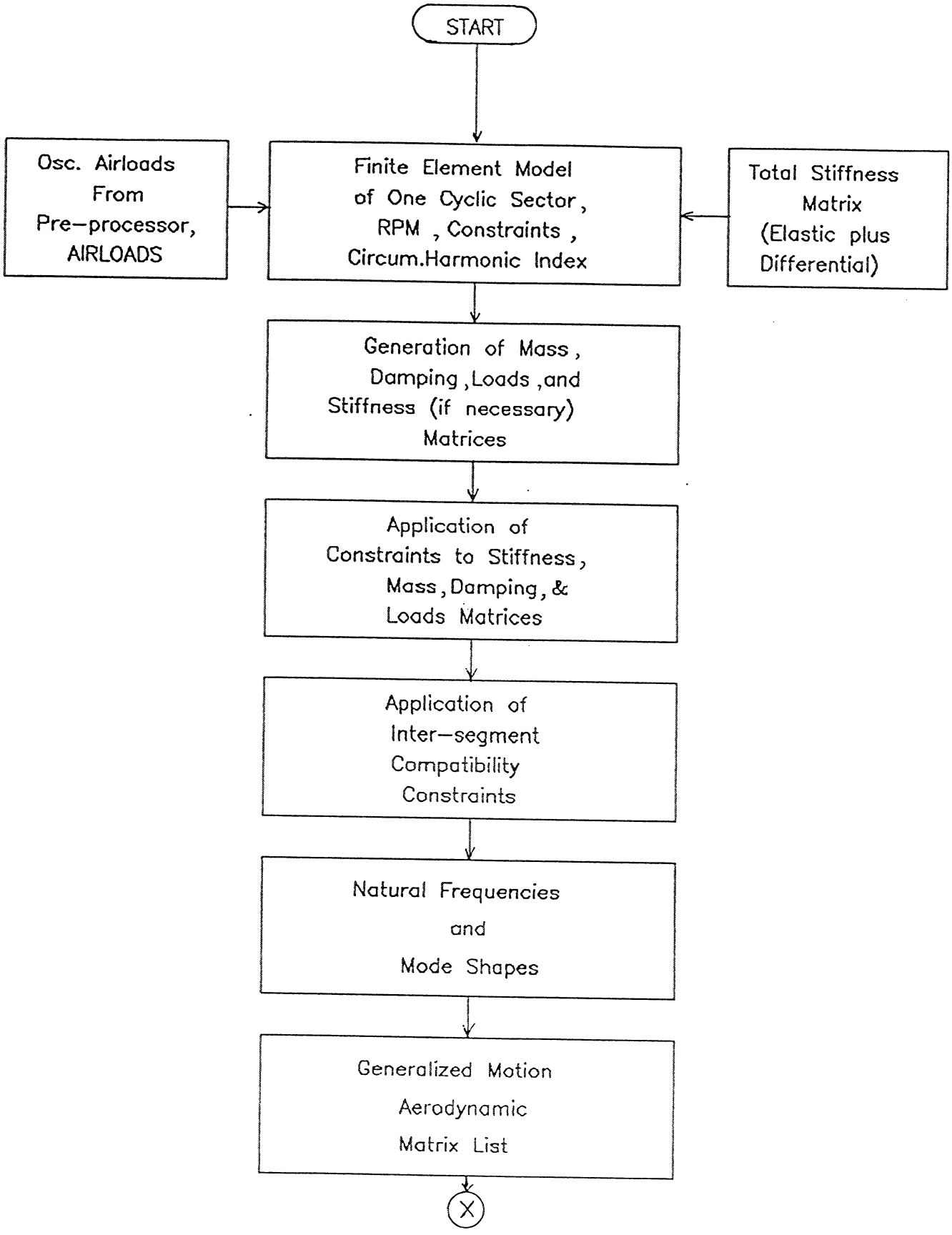

Figure 2.6 Overall Flowchart of Modal Forced Vibration Analysis Capability for Aerodynamically Excited Turbosystems

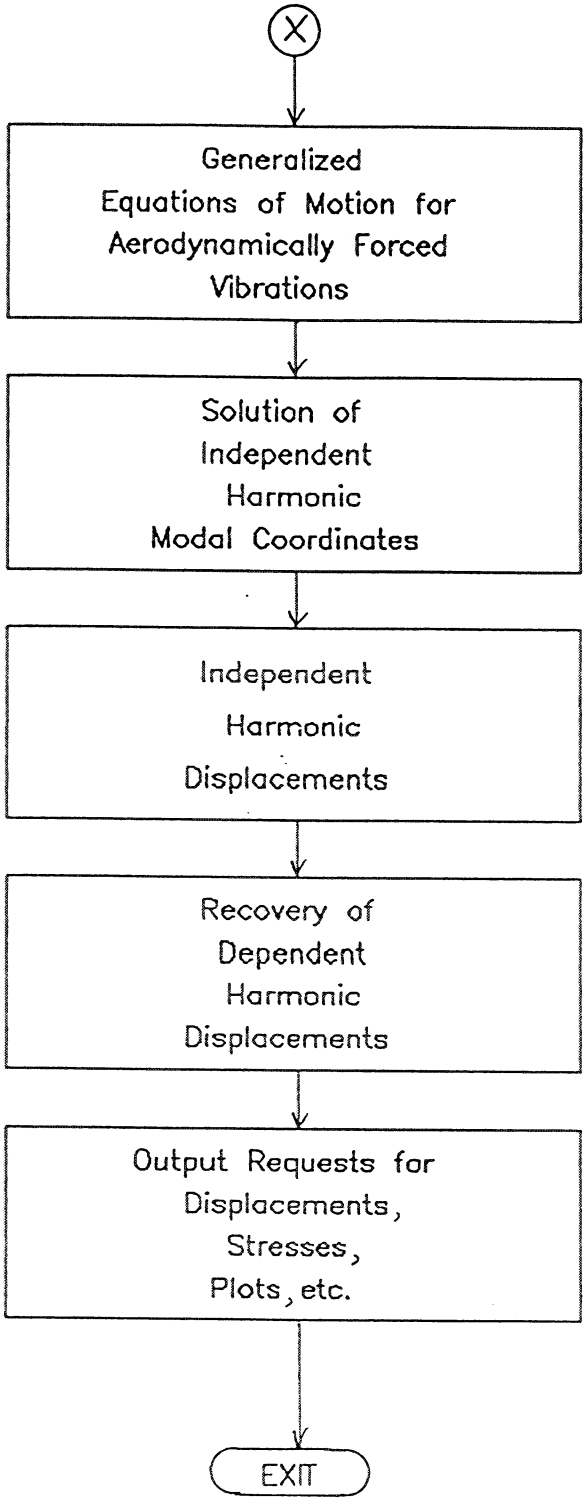

Figure 2.6 Concluded

3. APPLIED OSCILLATORY AIRLOADS

3.1 GENERAL

Generation of applied oscillatory aerodynamic loads on the blades of the turbosystems due to oscillatory relative inflow is briefly discussed in this section. Complete details of the airloads generation process are reported in Ref. 8.

A rotating turbosystem placed in a spatially non-uniform inflow, or in a uniform inflow with its axis of rotation misaligned with inflow direction, experiences oscillatory relative inflow.

The resultant oscillatory airloads are computed by the use of subsonic and supersonic 2-d cascade unsteady aerodynamic theories (Refs. 10 and 11). Accordingly, the aerodynamic model of the blade comprises non-intersecting strips as shown in Figure 2.2. The swept blade of an advanced turboprop is shown as an example. The analytical development is equally applicable to unswept blades.

The computation of the oscillatory airloads is carried out in the following four steps:

1. For a given chord, sinusoidal gust amplitudes, frequencies, and other aerodynamic excitation parameters (Appendix C), are determined based on the relative inflow variations as the blades go through one revolution.

2. Subsonic or supersonic theory with appropriate gust inputs from step 1 is used to determine oscillatory pressure distributions on the chord.

3. The unsteady pressure distribution on the blade strip associated with the chord is transformed to loads at the finite element structural grid on the chord.

4. Steps 1 through 3 are repeated for all chords spanning the blade.

After establishing the relative inflow velocity to be either subsonic, transonic, or supersonic from step 1, step 2 is merely an application of the appropriate theory. In case of transonic relative inflow, the airloads for that chord are interpolated from adjacent non-transonic chords. Steps 1 and 3 are discussed further in the following sections.

3.2 GUST AMPLITUDES AND FREQUENCIES OF OSCILLATORY RELATIVE INFLOW

The problem of determining the amplitude and frequency contents of oscillatory relative inflow gusts can be accomplished in four steps:

1. At the leading edge point A of any chord $\bar{s}$ (Figure 3.1), the relative inflow velocity is determined as a function of time t (at discrete time instances) during one revolution of the turboprop rotating at a constant angular velocity Ω.

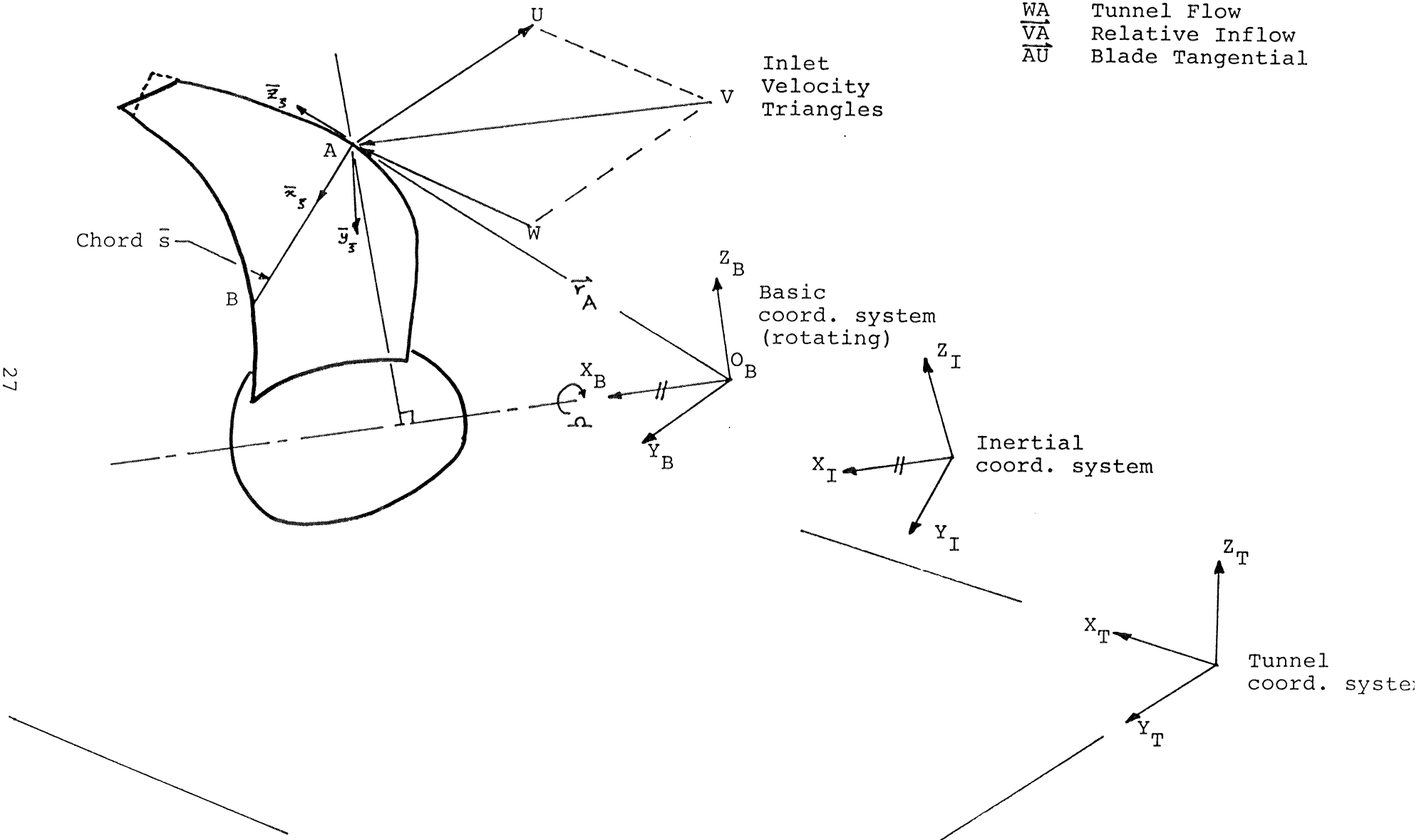

Figure 3.1 Inlet Velocity Triangles for Determining Oscillatory Relative Inflow

2. At each time step, the relative inflow velocity can be resolved into $\bar{x}_{\bar{s}}$, $\bar{y}_{\bar{s}}$, and $\bar{z}_{\bar{s}}$ components of the local chord coordinate system (Figure 3.1).

   - Component along $\bar{x}_{\bar{s}}$ is the cascade relative inflow velocity. Component along $\bar{y}_{\bar{s}}$ is the gust velocity. Component along $\bar{z}_{\bar{s}}$ is the radial velocity, which is ignored in 2-d cascade aerodynamics.

3. A Fourier series decomposition in ωt of

   a) the velocity component along $\bar{x}_{\bar{s}}$ yields the cascade mean relative inflow velocity as the constant term of the Fourier series (along AB, Figure 3.1). This is used to determine the relative Mach number and select the appropriate aerodynamic theory.

   b) the velocity component along $\bar{y}_{\bar{s}}$ yields the necessary sinusoidal gust amplitudes and frequencies which are subsequently input to appropriate oscillatory inflow aerodynamic theories.

4. Steps 1 through 3 are repeated for all chords spanning the blade to determine the oscillatory pressure distribution over the entire blade surface.

Referring to Figure 3.1, the relative inflow velocity at the leading edge point A on the chord $\bar{s}$, expressed in the chord coordinate system, is

$$\{VA\}^{\bar{x}_{\bar{s}}\,\bar{y}_{\bar{s}}\,\bar{z}_{\bar{s}}} = [T_{\bar{s}}^{BL}][T^{IB}][T^{TI}]\{WA\}^{Tunnel} - [T_{\bar{s}}^{BL}]\begin{Bmatrix} \vec{\Omega} \times \vec{r}_A \cdot \hat{I}_B \\ \vec{\Omega} \times \vec{r}_A \cdot \hat{J}_B \\ \vec{\Omega} \times \vec{r}_A \cdot \hat{K}_B \end{Bmatrix}^{Basic} \quad (1)$$

In equation (1), the position vector is

$$\vec{r}_A = (O_B A)_{X_B} \hat{I}_B + (O_B A)_{Y_B} \hat{J}_B + (O_B A)_{Z_B} \hat{K}_B \,, \quad (2)$$

and the coordinate transformations are

$$[T_{\bar{s}}^{BL}] = \begin{bmatrix} \beta_{11} & \beta_{12} & \beta_{13} \\ \beta_{21} & \beta_{22} & \beta_{23} \\ \beta_{31} & \beta_{32} & \beta_{33} \end{bmatrix} , \quad (3)$$

$$[T^{TI}] = \begin{bmatrix} \tau_{11} & \tau_{12} & \tau_{13} \\ \tau_{21} & \tau_{22} & \tau_{23} \\ \tau_{31} & \tau_{32} & \tau_{33} \end{bmatrix} , \quad (4)$$

and

$$[T^{IB}] = \begin{bmatrix} 1 & 0 & 0 \\ 0 & \cos\Omega t & \sin\Omega t \\ 0 & -\sin\Omega t & \cos\Omega t \end{bmatrix} . \quad (5)$$

Selecting the angular velocity $\vec{\Omega}$ to be

$$\vec{\Omega} = \Omega \hat{I}_I = \Omega \hat{I}_B \,, \quad (6)$$

equation (1) reduces to

$$\{VA\}^{\bar{x}_{\bar{s}}\,\bar{y}_{\bar{s}}\,\bar{z}_{\bar{s}}} = [G]\{WA\}^{Tunnel} - \Omega[T^{BL}_{\bar{s}}]\begin{Bmatrix} 0 \\ -(O_BA)_{Z_B} \\ (O_BA)_{Y_B} \end{Bmatrix}^{Basic}, \quad (7)$$

where

$$[G] = [T^{BL}_{\bar{s}}][T^{IB}][T^{TI}] . \quad (8)$$

For clarity of presentation, further development is separated into that for uniform and non-uniform inflows.

3.2.1 Uniform Inflow

In the uniform inflow case, the turbosystem axis of rotation is inclined at an angle γ with the uniform inflow velocity as shown in Figure 2.4. The transformation from the tunnel to the inertial coordinate system (equation (4)) becomes

$$[T^{TI}] = \begin{bmatrix} \cos\gamma & 0 & -\sin\gamma \\ 0 & 1 & 0 \\ \sin\gamma & 0 & \cos\gamma \end{bmatrix}, \quad (9)$$

with the uniform inflow velocity given by

$$\{WA\}^{Tunnel} = \begin{Bmatrix} (WA)_{X_T} \\ 0 \\ 0 \end{Bmatrix} . \quad (10)$$

Substitution of equations (10), (9), (5) and (3) in equation (7) yields the constant (independent of Ωt) part of $(VA)_{\bar{x}}$, and the oscillating (function of Ωt) part of $(VA)_{\bar{y}}$ as

$$con\,(VA)_{\bar{x}} = \beta_{11} \cos\gamma\, (WA)_{X_T} - \Omega\left[-\beta_{12}\,(O_B A)_{Z_B} + \beta_{13}\,(O_B A)_{Y_B}\right], \quad (11)$$

$$osc\,(VA)_{\bar{y}} = (WA)_{X_T} \sin\gamma\, \left[\beta_{22} \sin\Omega t + \beta_{23} \cos\Omega t\right]. \quad (12)$$

The equivalent complex representation of equation (12) is

$$osc\,(VA)_{\bar{y}} = (WA)_{X_T} \sin\gamma \sqrt{\beta_{22}^2 + \beta_{23}^2}\; e^{i(\Omega t - \delta)}, \quad (13)$$

with

$$\tan\delta = \beta_{22} / \beta_{23}. \quad (14)$$

Equation (11) defines the cascade relative inflow velocity for the chord $\bar{s}$, whereas equation (13) describes the incoming gust velocity at the frequency Ω.

3.2.2 Non-Uniform Inflow

Equation (7), in its most general form, yields the expressions for the cascade relative inflow velocity and the gust velocity. The cascade inflow velocity is

$$(VA)_{\bar{z}} = g_{11}\,(WA)_{X_T} + g_{12}\,(WA)_{Y_T} + g_{13}\,(WA)_{Z_T} - \Omega\left[-\beta_{12}\,(O_B A)_{Z_B} + \beta_{13}\,(O_B A)_{Y_B}\right], \quad (15)$$

where g_{ij}'s are the elements of the transformation G (equation

8), with

$$g_{11} = \beta_{11}\tau_{11} + \beta_{12}\left[\tau_{21}\cos\Omega t + \tau_{31}\sin\Omega t\right] + \beta_{13}\left[-\tau_{21}\sin\Omega t + \tau_{31}\cos\Omega t\right], \quad (16)$$

$$g_{12} = \beta_{11}\tau_{12} + \beta_{12}\left[\tau_{22}\cos\Omega t + \tau_{32}\sin\Omega t\right] + \beta_{13}\left[-\tau_{22}\sin\Omega t + \tau_{32}\cos\Omega t\right], \quad (17)$$

$$g_{13} = \beta_{11}\tau_{13} + \beta_{12}\left[\tau_{23}\cos\Omega t + \tau_{33}\sin\Omega t\right] + \beta_{13}\left[-\tau_{23}\sin\Omega t + \tau_{33}\cos\Omega t\right]. \quad (18)$$

The incoming gust velocity is

$$(VA)_{\bar{y}} = g_{21}(WA)_{x_T} + g_{22}(WA)_{y_T} + g_{23}(WA)_{z_T} - \Omega\left[-\beta_{22}(O_\beta A)_{z_\beta} + \beta_{23}(O_\beta A)_{y_\beta}\right], \quad (19)$$

where

$$g_{21} = \beta_{21}\tau_{11} + \beta_{22}\left[\tau_{21}\cos\Omega t + \tau_{31}\sin\Omega t\right] + \beta_{23}\left[-\tau_{21}\sin\Omega t + \tau_{31}\cos\Omega t\right], \quad (20)$$

$$g_{22} = \beta_{21}\tau_{12} + \beta_{22}\left[\tau_{22}\cos\Omega t + \tau_{32}\sin\Omega t\right] + \beta_{23}\left[-\tau_{22}\sin\Omega t + \tau_{32}\cos\Omega t\right], \quad (21)$$

$$g_{23} = \beta_{21}\tau_{13} + \beta_{22}\left[\tau_{23}\cos\Omega t + \tau_{33}\sin\Omega t\right] + \beta_{23}\left[-\tau_{23}\sin\Omega t + \tau_{33}\cos\Omega t\right]. \quad (22)$$

Both $(VA)_{\bar{x}}$ (equation (15)) and $(VA)_{\bar{y}}$ (equation (19)) are

periodic functions of the azimuthal angle Ωt, with a maximum period of 2π as the blade completes one revolution in spatially non-uniform absolute inflow field. Each of these velocities can be expanded as finite Fourier series

$$f(\Omega t) = f_o + \sum_{p=1}^{P} \left[f_{pc} \cos \overline{p\Omega t} + f_{ps} \sin \overline{p\Omega t} \right] . \qquad (23)$$

The coefficients f_o, f_{pc}, and f_{ps} are determined by knowing f at M equally spaced intervals between 0 and 2π. The upper limit of harmonics, P, is given by

$$\left.\begin{aligned} P &= (M-1)/2 \quad , \quad M \text{ odd} , \\ &= M/2 \quad , \quad M \text{ even} . \end{aligned}\right\} \qquad (24)$$

In the non-uniform inflow case, the f_o component of $(VA)_{\bar{x}}$ is taken as the constant part of the cascade relative inflow velocity. For a selected harmonic p, the oscillating part of $(VA)_{\bar{y}}$ is written as

$$\text{osc}\,(VA)_{\bar{y}}\Big|_p = \sqrt{f_{pc}^2 + f_{ps}^2}\; e^{i(p\Omega t - \delta_p)} , \qquad (25)$$

with

$$\tan \delta_p = f_{ps} / f_{pc} . \qquad (26)$$

The excitation frequency correspondingly is $p\Omega$.

3.3 GRID POINT LOADS FROM OSCILLATORY PRESSURE DISTRIBUTION ALONG CHORD

The subsonic and supersonic aerodynamic routines compute the oscillatory pressure distribution at a number of points between the leading and trailing edges of a given chord. These points are generally distinct from the structural grid points at which the applied airloads are desired.

To obtain the loads at structural grid points, the chord is divided into a number of segments as shown in Figure 3.2. For each of the segments, the loads at its ends, directed along $+\bar{y}$, are calculated. As an example, for the $G_2 G_3$ segment,

$$P_{G_2} = \frac{1}{\Delta}\left[\int_{\bar{x}_{G_2}}^{\bar{x}_{G_3}} \Delta p(\bar{x}) \cdot w(\bar{x}) \cdot \overline{\bar{x}_{G_3} - \bar{x}}\; d\bar{x}\right], \text{ and} \qquad (27)$$

$$P_{G_3} = \frac{1}{\Delta}\left[\int_{\bar{x}_{G_2}}^{\bar{x}_{G_3}} \Delta p(\bar{x}) \cdot w(\bar{x}) \cdot \overline{\bar{x} - \bar{x}_{G_2}}\, d\bar{x}\right], \qquad (28)$$

where $\Delta = \bar{x}_{G_3} - \bar{x}_{G_2}$, and w is strip width associated with the given chord.

Furthermore, the load at grid point G_2, for instance, comprises the algebraic sum of those contributed by segments $G_1 G_2$ and $G_2 G_3$.

The applied oscillatory airloads generation procedure has been implemented in a stand-alone (independent of NASTRAN system) computer program, AIRLOADS, which is described in detail in Ref. 8.

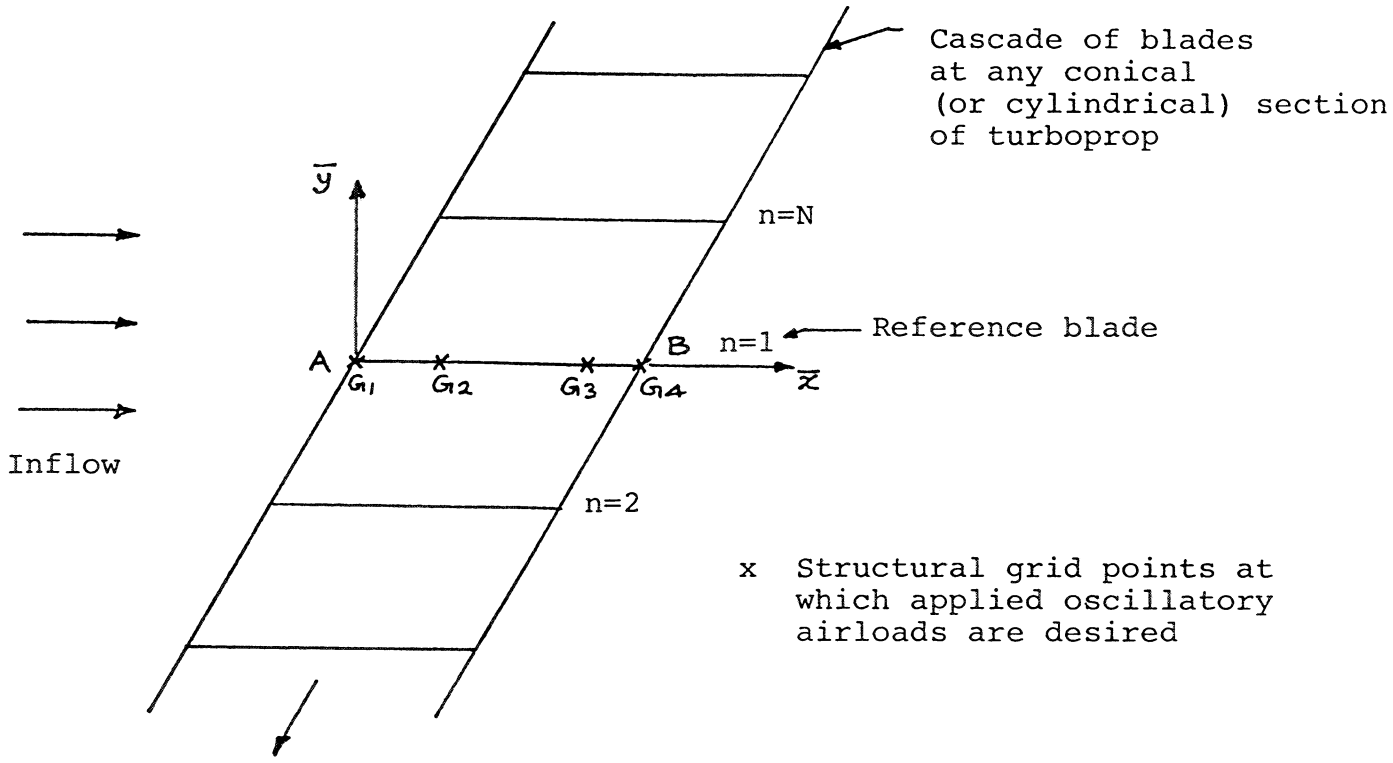

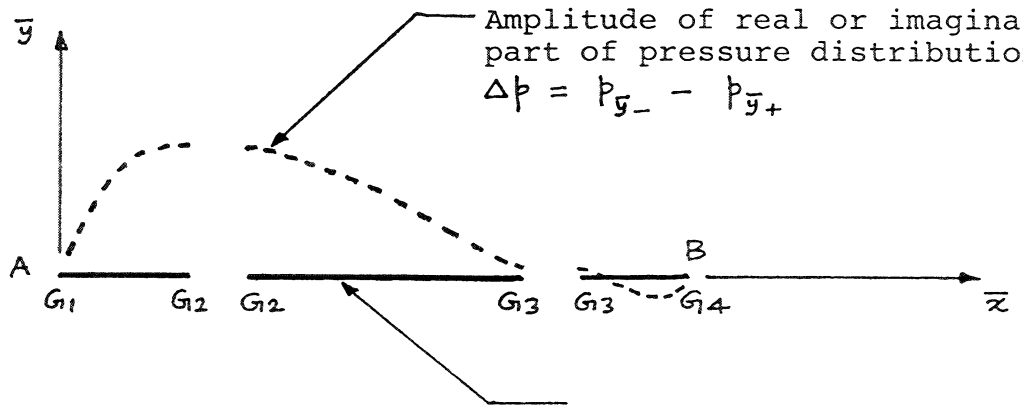

Figure 3.2 Transformation of Oscillatory Pressure Distribution to Loads at Structural Grid Points

4. APPLICATION EXAMPLES

4.1 GENERAL

The theoretical development of the preceding sections, as implemented in the Bladed Disks Computer Program in the April 1984 release of NASTRAN on the CRAY 1-S computer system at NASA LeRC, was used to conduct a total of eight examples on the SR-3 and SR-5 advanced turboprops. These examples were selected by NASA.

4.2 EXAMPLES

The SR-3 and SR-5 examples are listed by operating conditions in Table 4.1. These conditions were selected by NASA to cover a range of wind tunnel test conditions and provide a degree of commonality between examples to cut down on the computational steps.

At each of these operating conditions, it was desired to

1. calculate the natural frequencies and mode shapes of the turboprops,

2. examine the aeroelastic stability, and

3. determine the one-per-rev stress response at the strain gage locations shown in Figures 4.1 and 4.2 for the SR-3 and SR-5 turboprops, respectively.

Table 4.1 Operating Conditions for SR-3 and SR-5 Examples

Turboprop Blade	NASA Test Rdg. No.	Freestream			Blade Setting Angle $\beta_{3/4}$ (deg)	Prop. axis tilt (deg)	Prop. RPM
		Mach No.	Velocity (ft/sec)	Density $\times 10^3$ ($lbf\text{-}sec^2/ft^4$)			
SR-3	190	.353	398	2.3833	48.9	8	8000
	273	.798	873	1.9034	60.8	2	8000
	277	.795	871	1.9053	60.8	4	7000
	278	.795	871	1.9060	60.8	4	8000
SR-5	8508	.801	885	1.8225	70.8	2	5500
	8511	.797	881	1.8313	70.8	5	5500
	8607	.360	411	2.3057	60.8	12	6000
	8610	.361	411	2.3062	60.8	3	6000

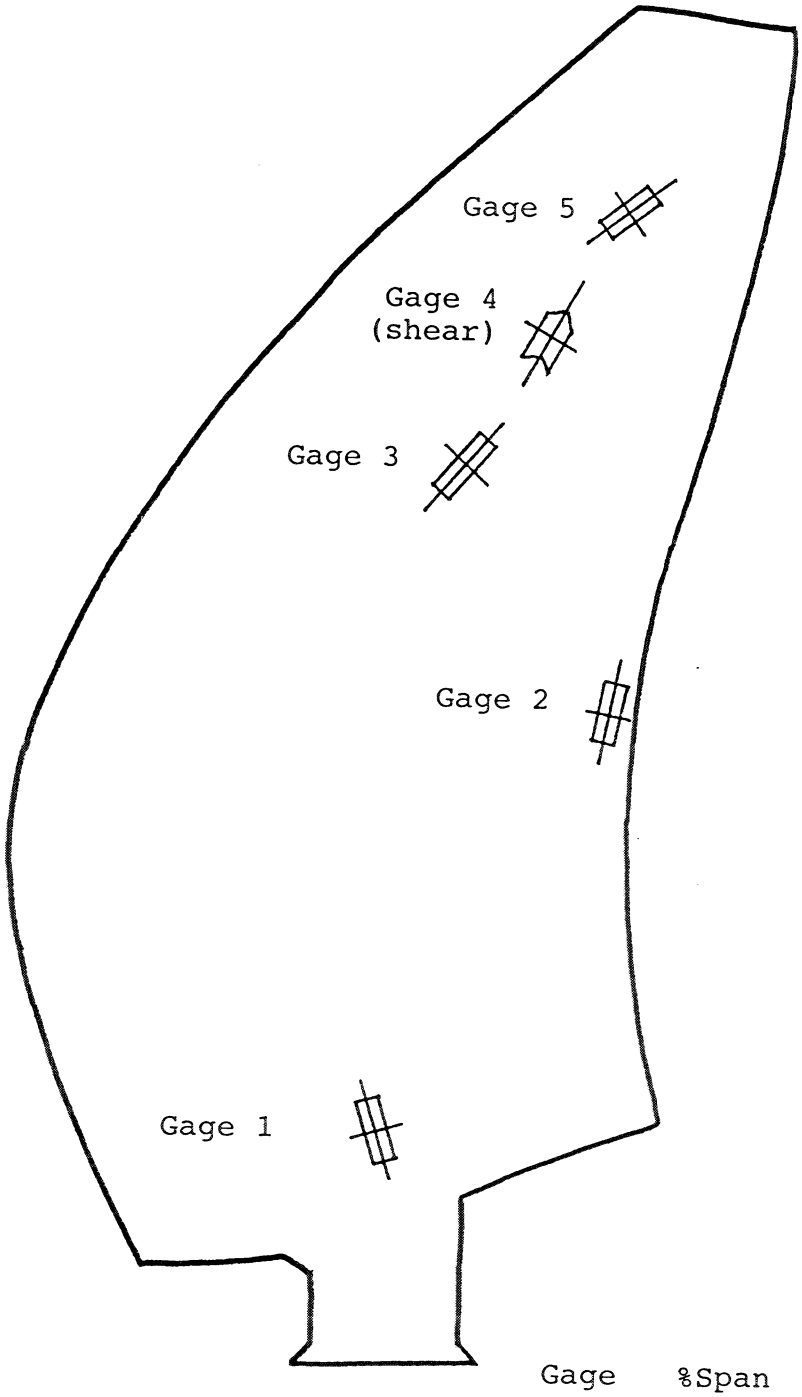

Gage	%Span	%Chord	Angle from Radial
1	30.0	54	-19°
2	55.1	96	11.3°
3	69.9	56	42°
4	78.4	59	38.5°
5	86.3	61	49°

Figure 4.1 SR-3 Strain Gage Locations (Suction Side)

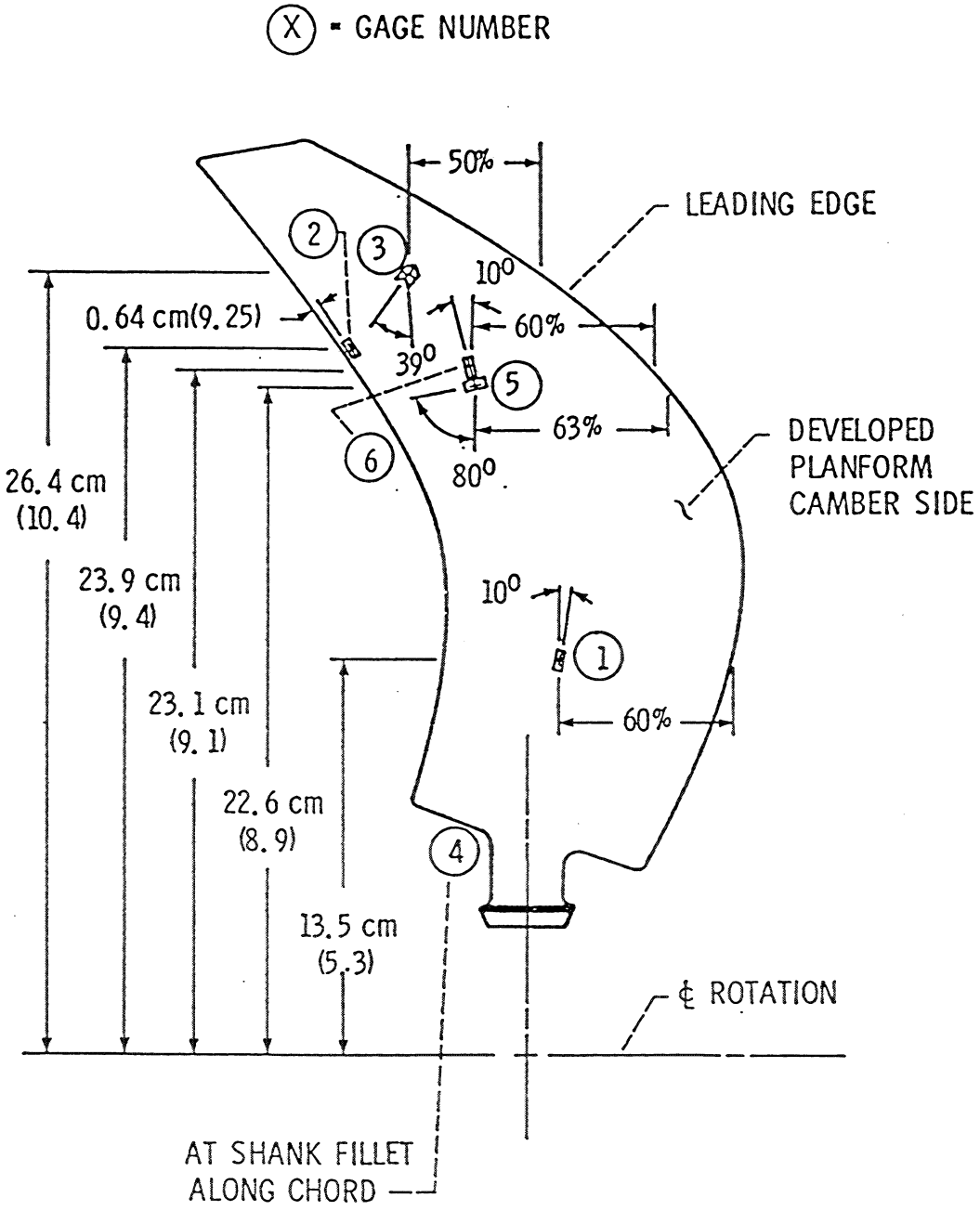

Figure 4.2 SR-5 Strain Gage Locations
(Suction Side)

4.3 STRUCTURAL AND AERODYNAMIC MODELS

NASA provided the NASTRAN finite element structural and aerodynamic models of the SR-3 and SR-5 turboprops shown in Figures 4.3 and 4.4, respectively. The aerodynamic models were defined as subsets of the structural grid.

Both models, with homogeneous material properties of Young's modulus = 1.6×10^7 psi, Poisson's ratio = .35 , and mass density = .16 lbm/in^3 , were built using the TRIA2 triangular plate element with bending and membrane capabilities.

4.4 BOUNDARY CONDITIONS

For the purposes of the present analyses, the turboprop hub was considered to be rigid as compared to the blade flexibility for both SR-3 and SR-5. This mechanical decoupling between blades was achieved by completely constraining the degrees of freedom at the bottom of the blade shank, and by not modelling the hub.

4.5 APPLIED OSCILLATORY AIRLOADS

The applied airloads were generated by using the AIRLOADS program discussed in Section 3 and Ref. 8. This program is capable of reading the NASTRAN structural and aerodynamic grid data, and the operating conditions to generate the oscillatory airloads. Upon user's request, the program also produces two output files for the oscillatory applied airloads for convenient

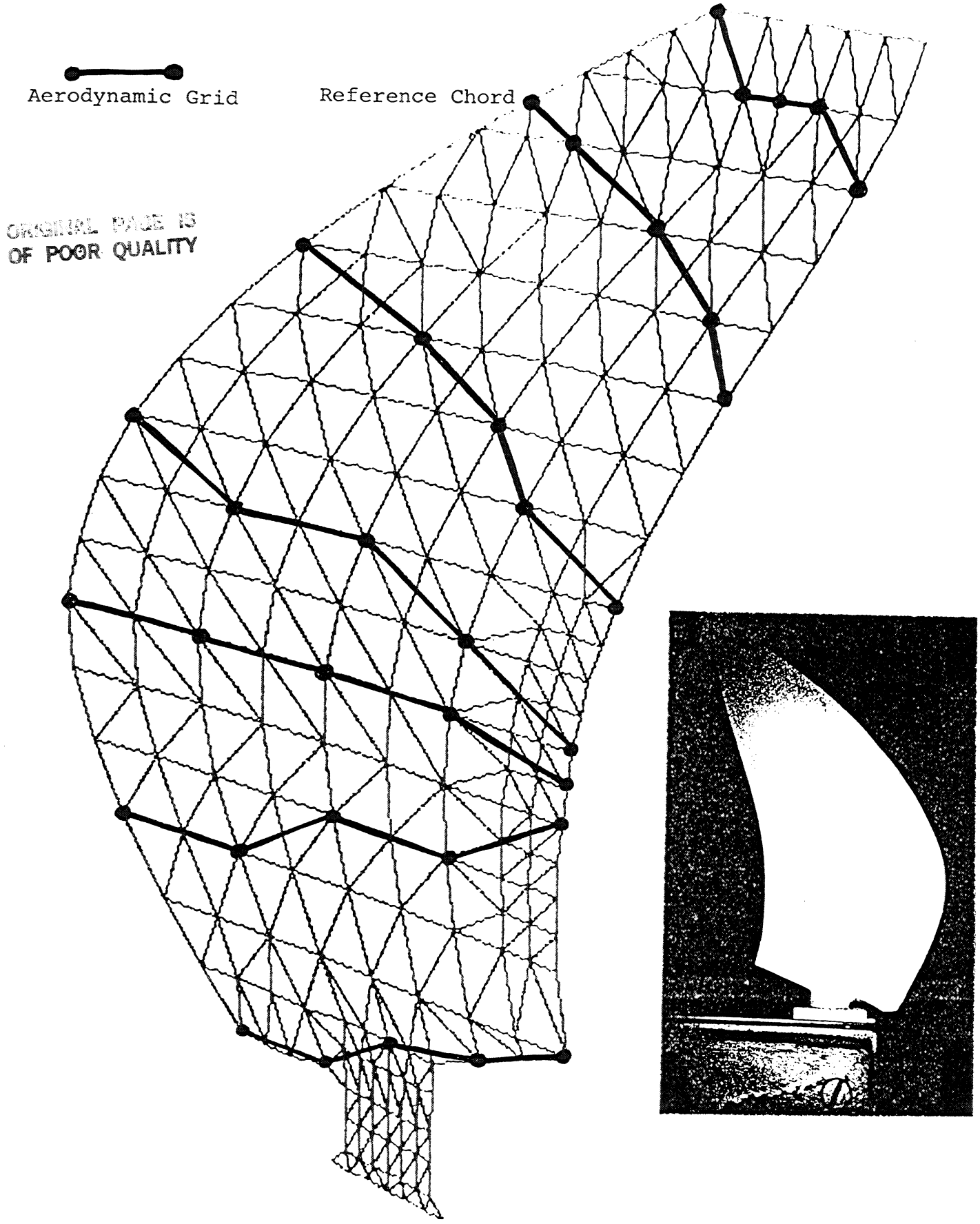

Figure 4.3 NASTRAN Structural and Aerodynamic Models of SR-3

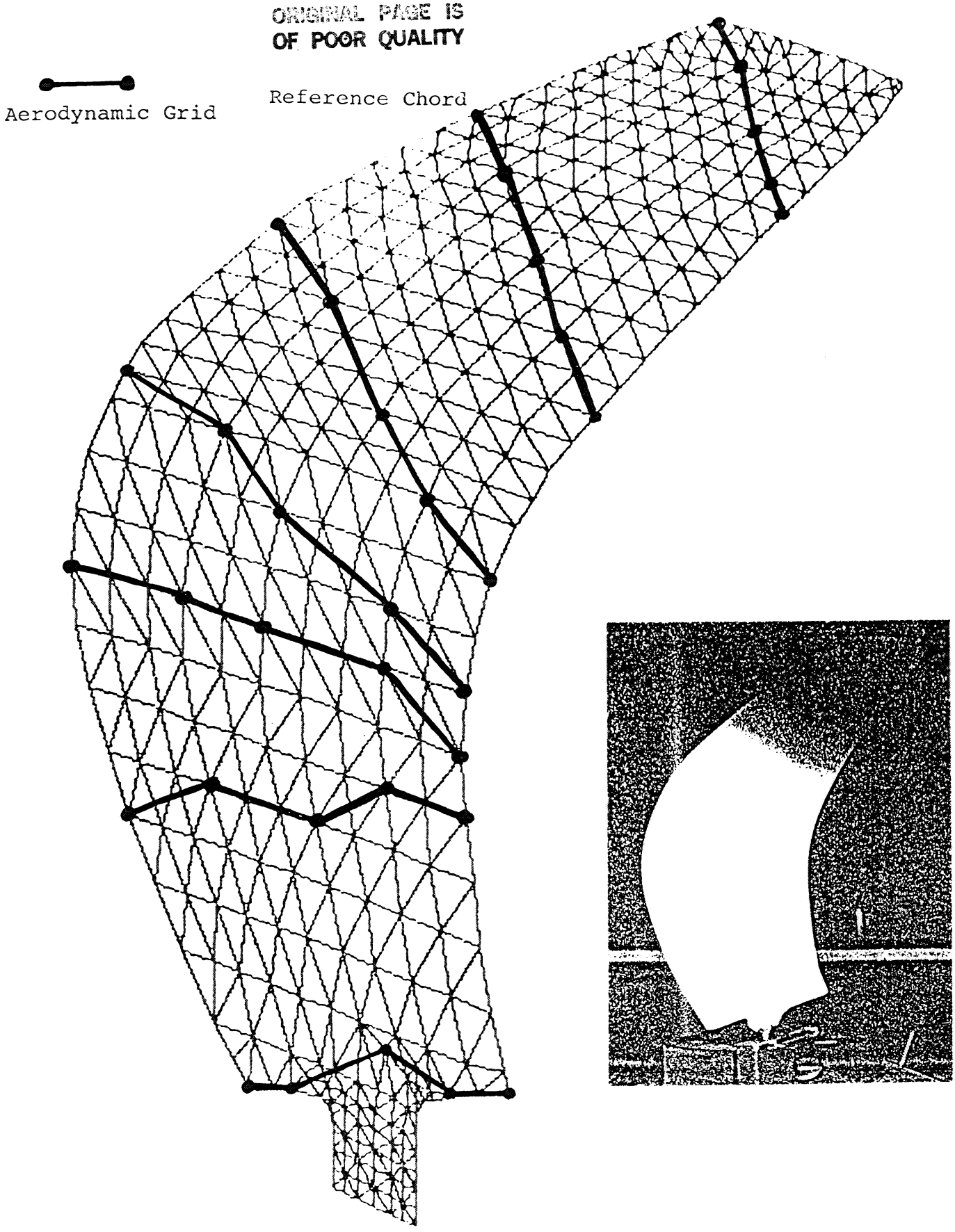

Figure 4.4 NASTRAN Structural and Aerodynamic Models of SR-5

inclusion into NASTRAN Case Control and Bulk Data Decks. The streamline geometry and flow data generated by the AIRLOADS program was also useful in conducting aeroelastic stability analysis.

4.6 ANALYSIS STEPS FOR EACH OPERATING CONDITION

A series of procedural steps was setup to systematically conduct all of the analysis required for the turboprops at each of the operating conditions listed in Table 4.1. An overall flowchart of these steps is shown in Figure 4.5.

The sequence of four runs shown is arbitrary to an extent , and could be rearranged as per user's needs.

Run 1. Differential/Stiffness analysis was conducted at the operating rpm with the blade set at the selected blade setting angle. Displacement Approach RF 4 was used , and the total (elastic plus differential) stiffness was saved as KTOTAL.

Run 2/3. Aeroelastic stability of the turboprop at the selected operating point was determined using the Aero Approach RF 9. V-g, V-f plots were used to determine stability.

If desired, the AERO and STREAMLi bulk data cards required for this run can be obtained from the AIRLOADS program, Run 3/2.

Natural frequencies and mode shape plots can be optionally obtained in this run.

Run 3/2. At the given operating condition with the prop axis

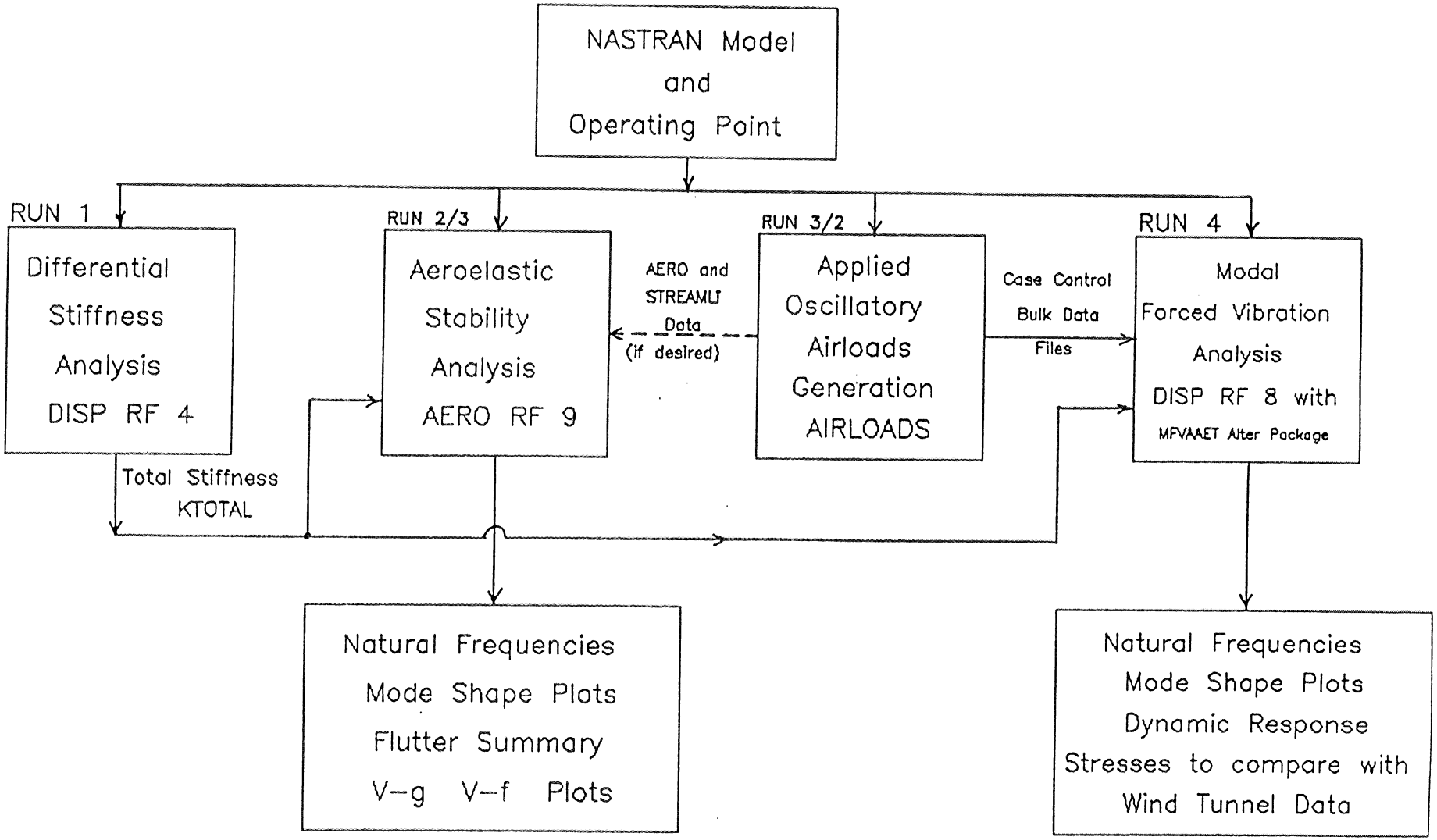

Figure 4.5 Overall Flowchart of Analyses Steps to Conduct Each of the SR-3 and SR-5 Examples

set at an angle with the uniform inflow, the applied oscillatory airloads distribution on the modelled turboprop blade was generated using the newly developed AIRLOADS program. At user's option, individual output files for direct inclusion in the Case Control and Bulk Data Decks of the subsequent response Run 4 were also created.

Run 4. Finally, modal forced vibration analysis was conducted using the newly developed Displacement Approach RF 8 alter package, MFVAAET (Modal Forced Vibration Analysis of Aerodynamically Excited Turbosystems).

Element stresses in element coordinate systems for elements neighboring a strain gage location were transformed along strain gage orientation as follows:

$$S_{normal} = \frac{S_x + S_y}{2} + \frac{S_x - S_y}{2} \cos 2\theta + S_{xy} \sin 2\theta \text{ , and}$$

$$S_{shear} = \frac{S_x - S_y}{2} \sin 2\theta - S_{xy} \cos 2\theta \text{ ,}$$

where θ is the angle between the strain gage axis and the x-axis of the element coordinate system.

5. RESULTS AND DISCUSSION

5.1 GENERAL

Results of the SR-3 and SR-5 examples described in the previous section are presented in Table 5.1 (SR-3 and SR-5), Figures 5.1 through 5.15 (SR-3), and Figures 5.16 through 5.32 (SR-5).

For all of the contour plots shown in these Figures, the contours for the translational displacements along the Basic coordinate system Y axis are plotted within the UNDEFORMED shape outline. The outline for the DEFORMED shape accounting for the total translational displacements is also shown. For all mode shape plots, the contours represent zero displacement along the Basic Y axis.

Following discussions are grouped by analyses.

5.2 DIFFERENTIAL STIFFNESS

Results of differential stiffness analysis of SR-3 test reading no. 190, and SR-5 test reading no. 8508 are shown in Figures 5.1 - 5.2, and 5.16 - 5.17 respectively.

Convergence of the non-linear part of the analysis was achieved after two iterations for all operating conditions.

In the present context, the differential stiffness analysis

Table 5.1 Natural Frequencies of SR-3 and SR-5 Turboprops

Turboprop Blade	NASA Test Rdg. No.	Blade Setting Angle $\beta_{3/4}$ (deg)	Prop. RPM	Natural Frequencies, Hz.				
				Mode 1	Mode 2	Mode 3	Mode 4	Mode 5
SR-3	190	48.9	8000	227	431	673	759	915
	273	60.8	8000	220	423	666	757	911
	277	60.8	7000	210	417	652	743	905
	278	60.8	8000	220	423	666	757	911
SR-5	8508	70.8	5500	140	275	558	650	718
	8511	70.8	5500	140 (166)*	275 (287)	558	650	718
	8607	60.8	6000	150	281	564	658	723
	8610	60.8	6000	150 (173)	281 (288)	564	658	723

* Experimental Values

MAX-DEF. = 0.36370445

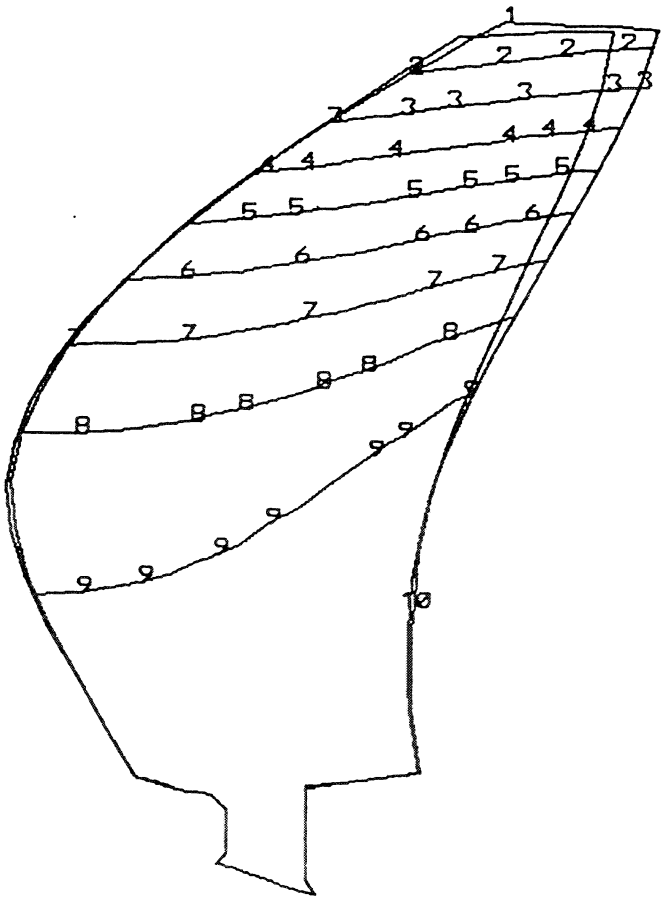

SR3 RESPONSE TO 1 PER REV OSC. AIRLOADS
NASA TEST READING NO. 190 SOL 4
DIFF. STIFF. ANAL.--LINEAR SOLUTION
STATIC DEFOR. SUBCASE 1 LOAD 1

Figure 5.1 SR-3 Differential Stiffness Analysis--Linear Solution

MAX-DEF. = 0.12401215

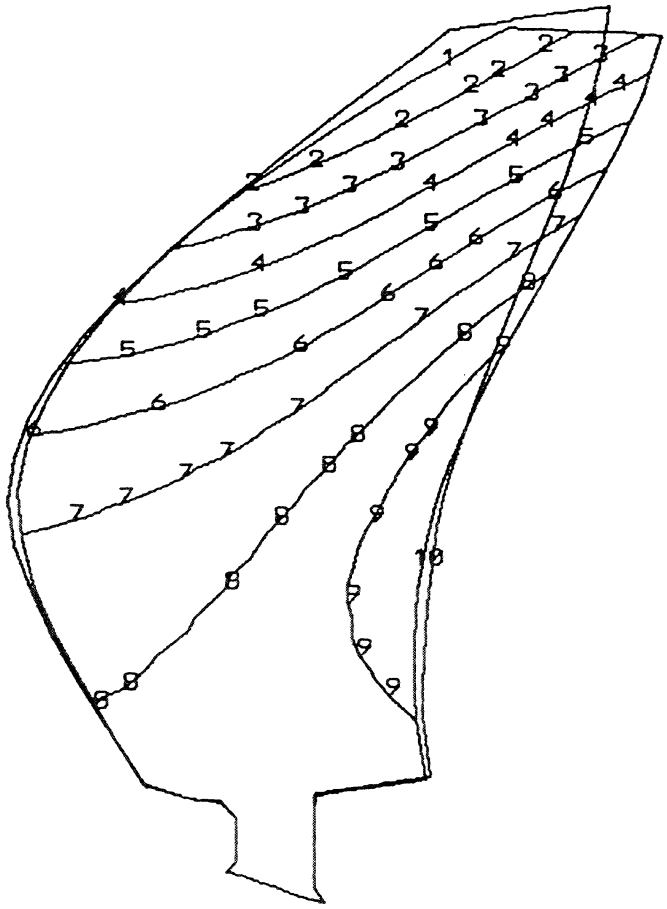

SR3 RESPONSE TO 1 PER REV OSC. AIRLOADS
NASA TEST READING NO. 190 SOL 4
DIFF. STIFF. ANAL.--NONLINEAR SOLUTION
STATIC DEFOR. SUBCASE 2 LOAD 1

Figure 5.2 SR-3 Differential Stiffness Analysis--Non-Linear Solution

MAX-DEF. = 0.55044185

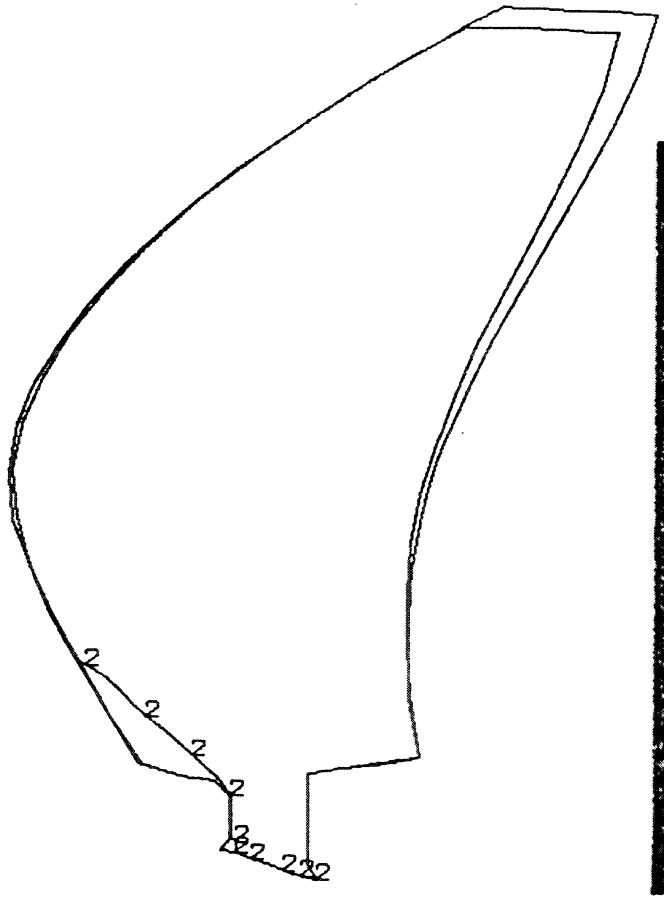

SR3 RESPONSE TO 1 PER REV OSC. AIRLOADS
NASA TEST READING NO. 190
K = 0 MODES- OSCILLATORY AIRLOADS PRESENT
MODAL DEFOR. SUBCASE 1 MODE 1 FREQ. 227.1975

Figure 5.3 SR-3 Mode 1

MAX-DEF. = 0.62499093

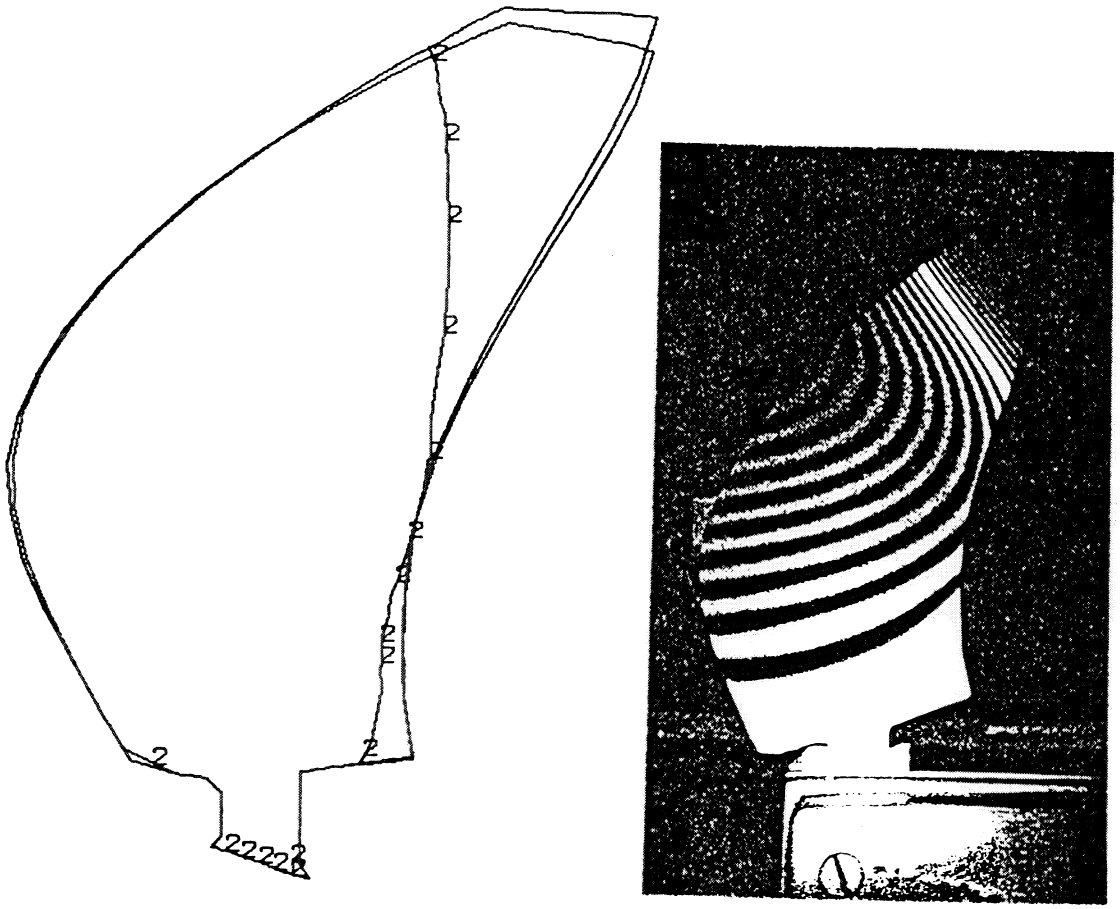

SR3 RESPONSE TO 1 PER REV OSC. AIRLOADS
NASA TEST READING NO. 190
K = 0 MODES- OSCILLATORY AIRLOADS PRESENT
MODAL DEFOR. SUBCASE 1 MODE 2 FREQ. 431.7661

Figure 5.4 SR-3 Mode 2

MAX-DEF. = 0.27690971

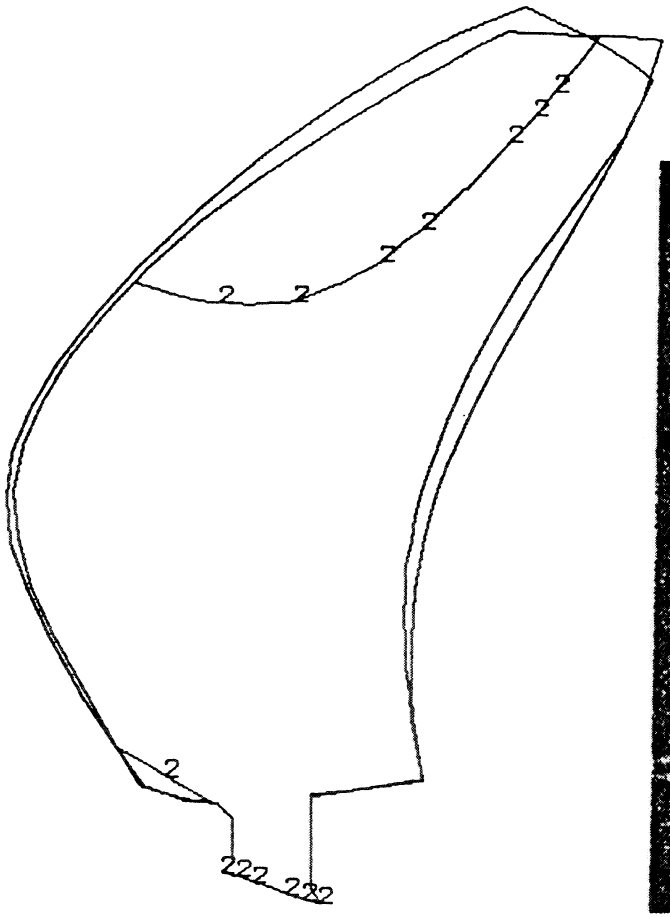

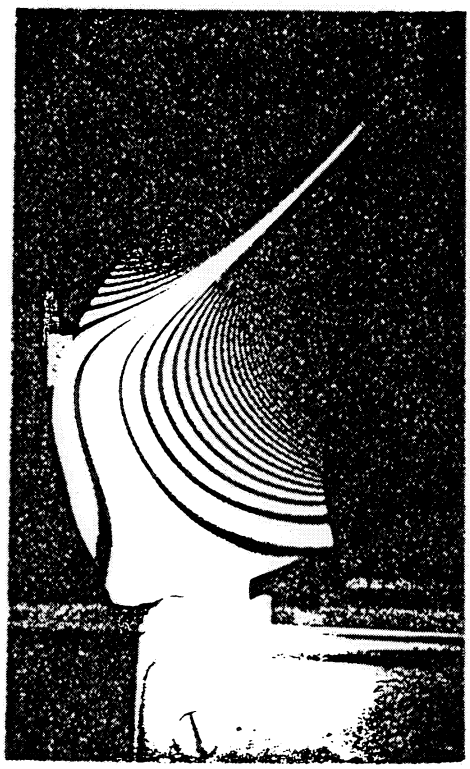

SR3 RESPONSE TO 1 PER REV OSC. AIRLOADS
NASA TEST READING NO. 190
K = 0 MODES- OSCILLATORY AIRLOADS PRESENT
MODAL DEFOR. SUBCASE 1 MODE 3 FREQ. 673.0511

Figure 5.5 SR-3 Mode 3

MAX-DEF. = 0.69575762

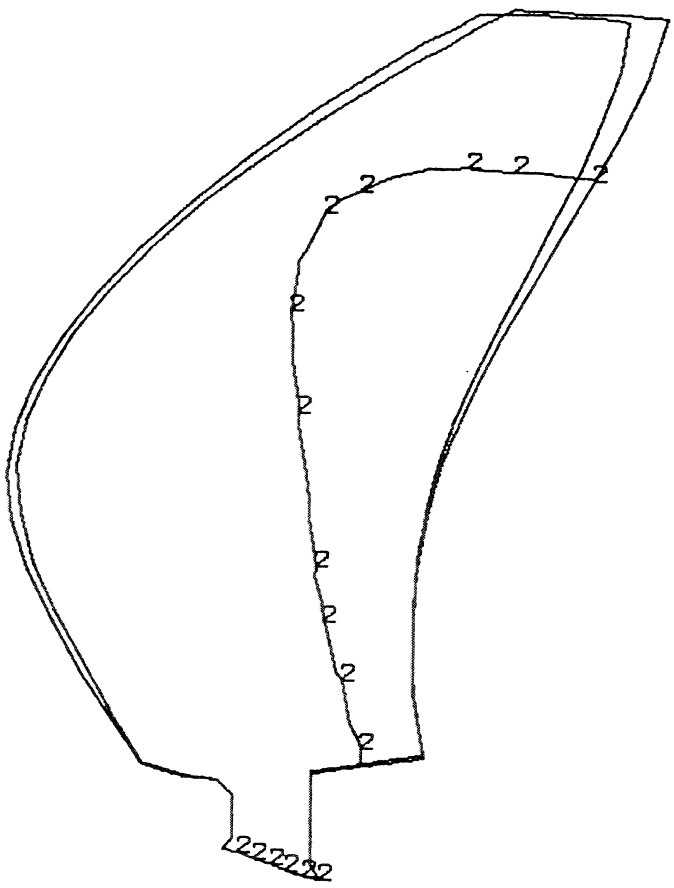

SR3 RESPONSE TO 1 PER REV OSC. AIRLOADS
NASA TEST READING NO. 190
K = 0 MODES- OSCILLATORY AIRLOADS PRESENT
MODAL DEFOR. SUBCASE 1 MODE 4 FREQ. 759.2396

Figure 5.6 SR-3 Mode 4

MAX-DEF. = 0.77304033

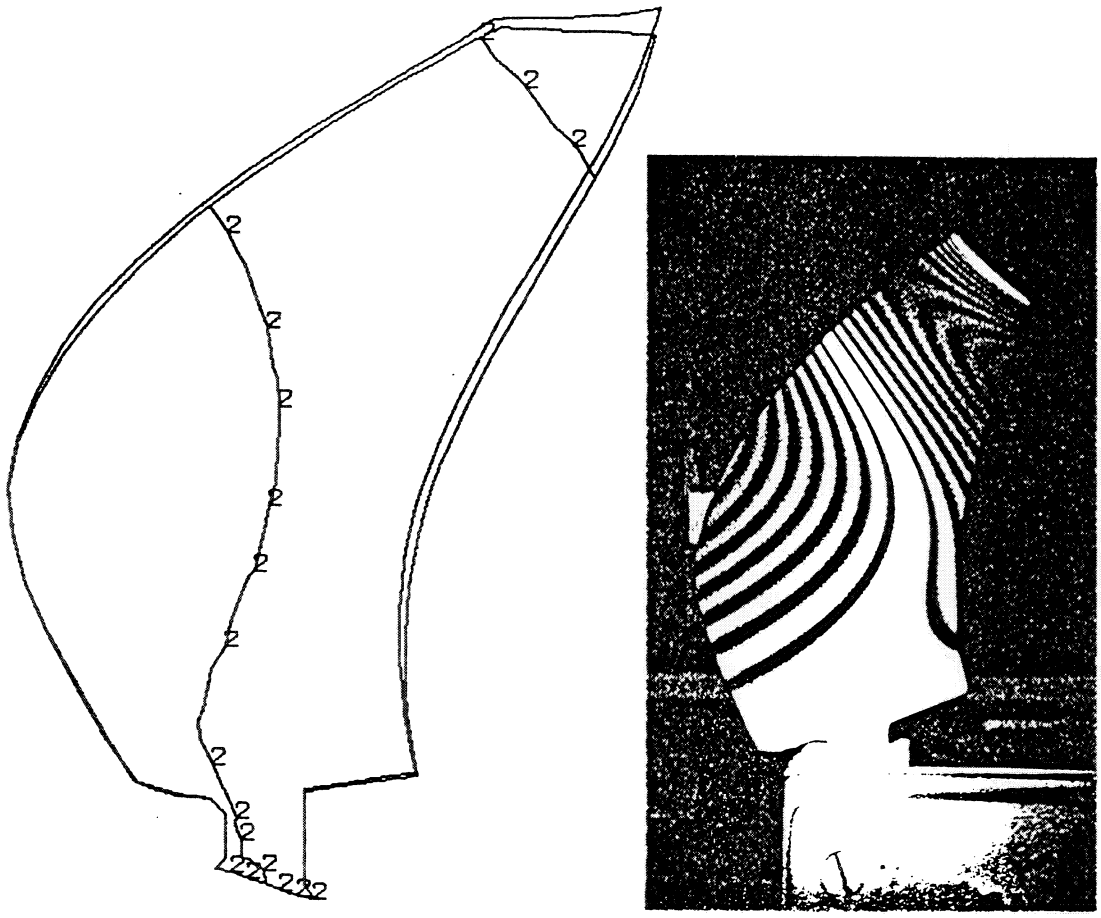

SR3 RESPONSE TO 1 PER REV OSC. AIRLOADS
NASA TEST READING NO. 190
K = 0 MODES- OSCILLATORY AIRLOADS PRESENT
MODAL DEFOR. SUBCASE 1 MODE 5 FREQ. 915.2528

Figure 5.7 SR-3 Mode 5

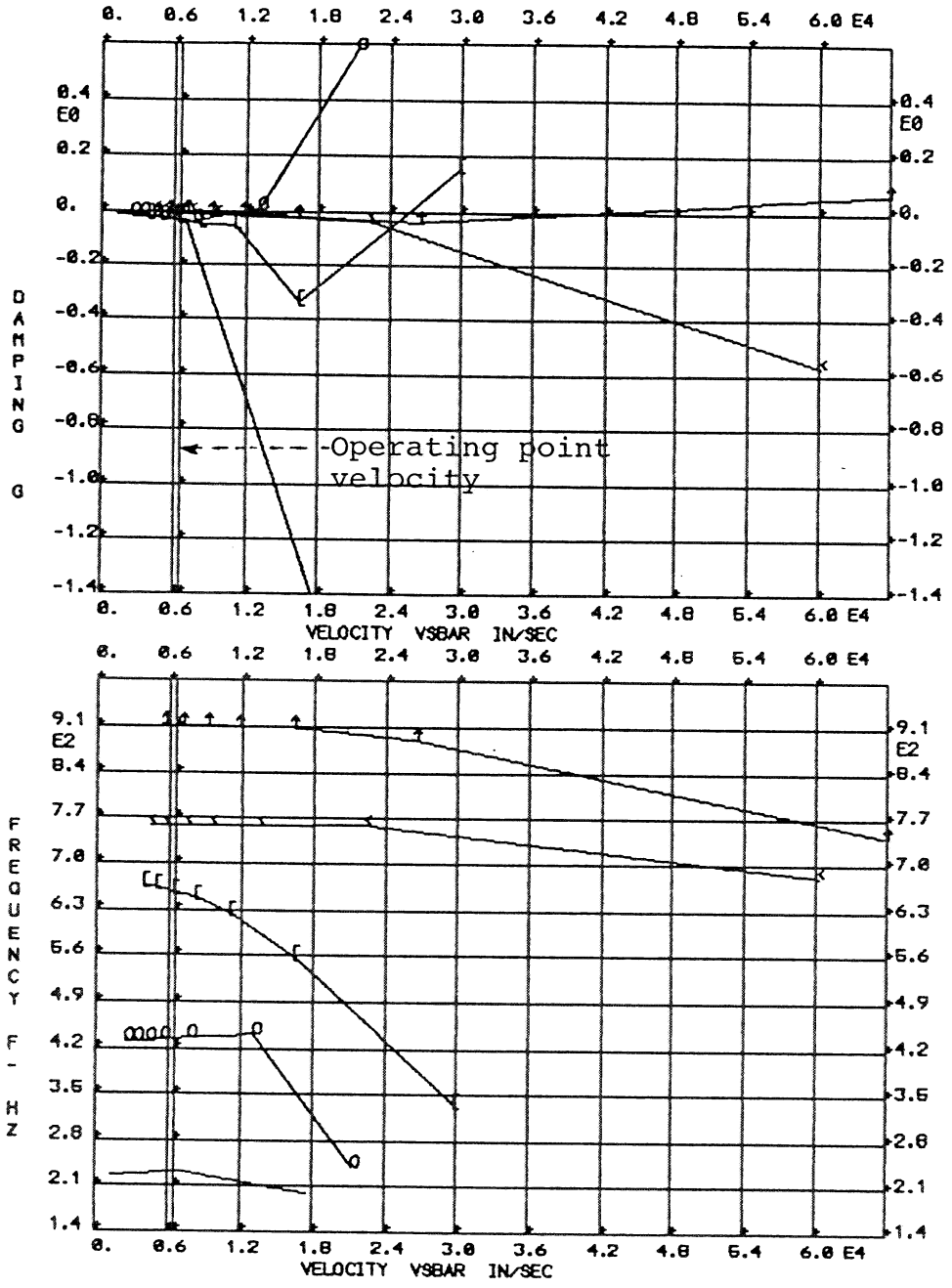

Figure 5.8 SR-3 V-g, V-f Curves
--Test Reading No. 190

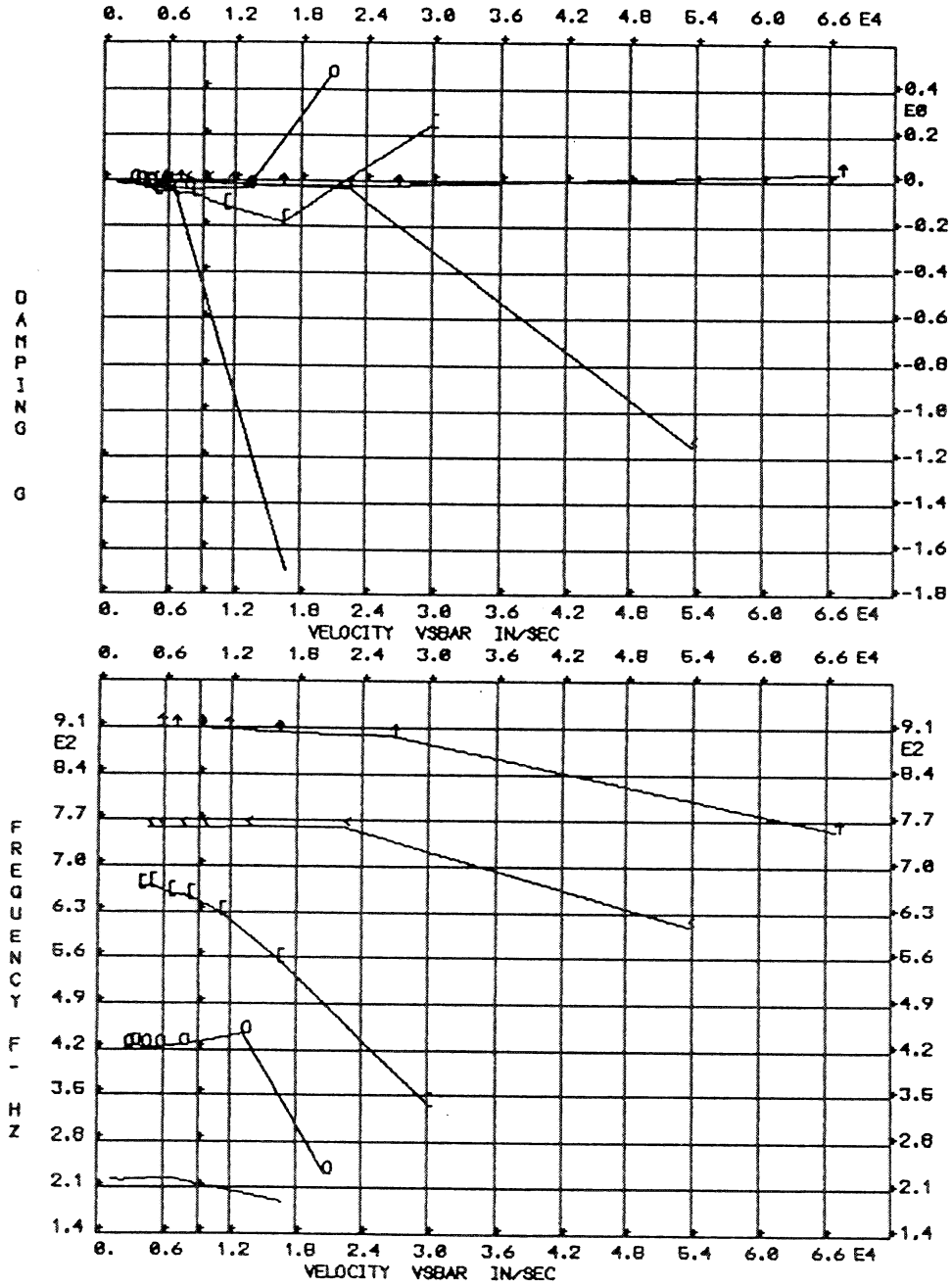

Figure 5.9 SR-3 V-g, V-f Curves
--Test Reading No. 273

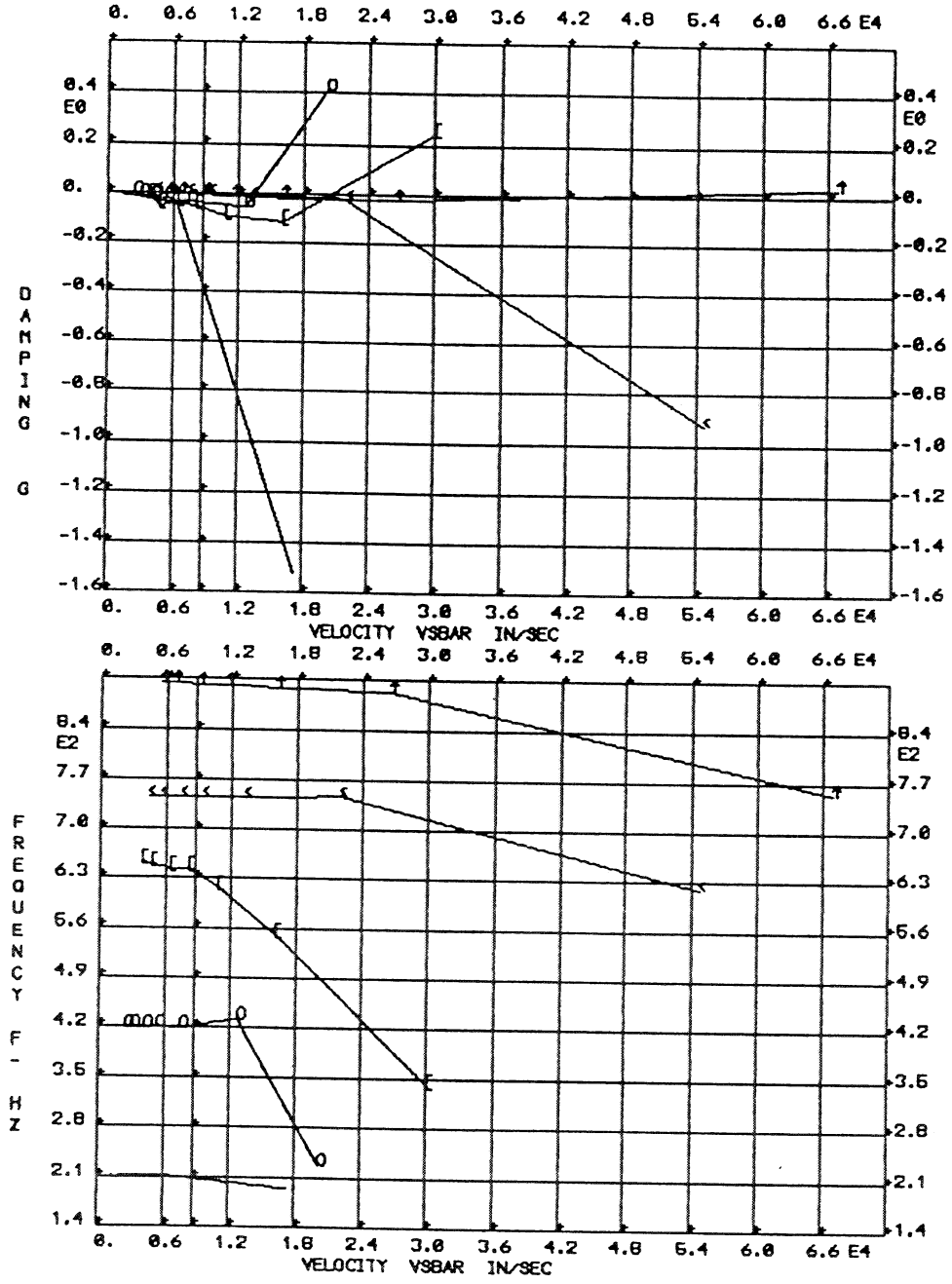

Figure 5.10 SR-3 V-g, V-f Curves
--Test Reading No. 277

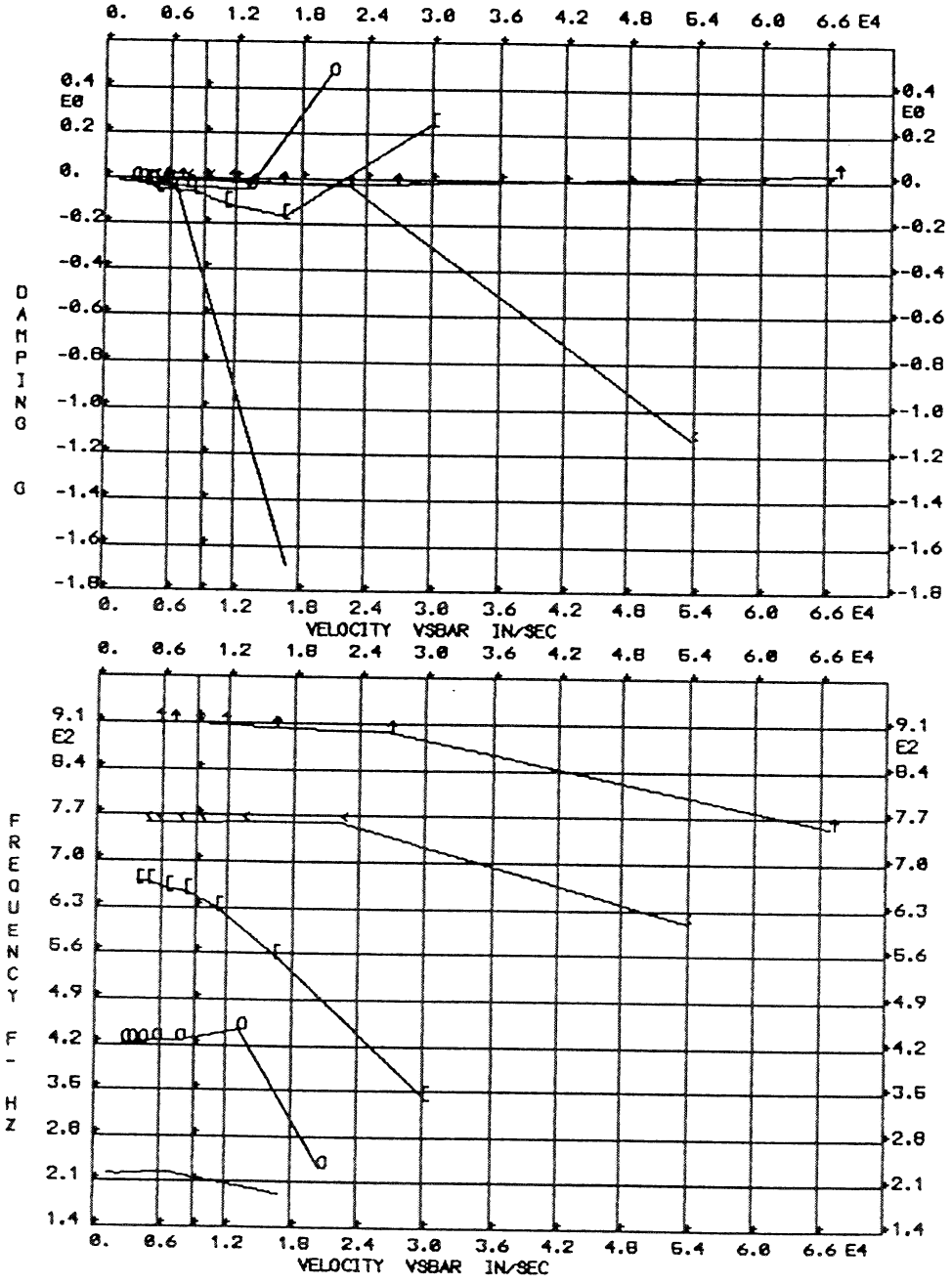

Figure 5.11 SR-3 V-q, V-f Curves
--Test Reading No. 278

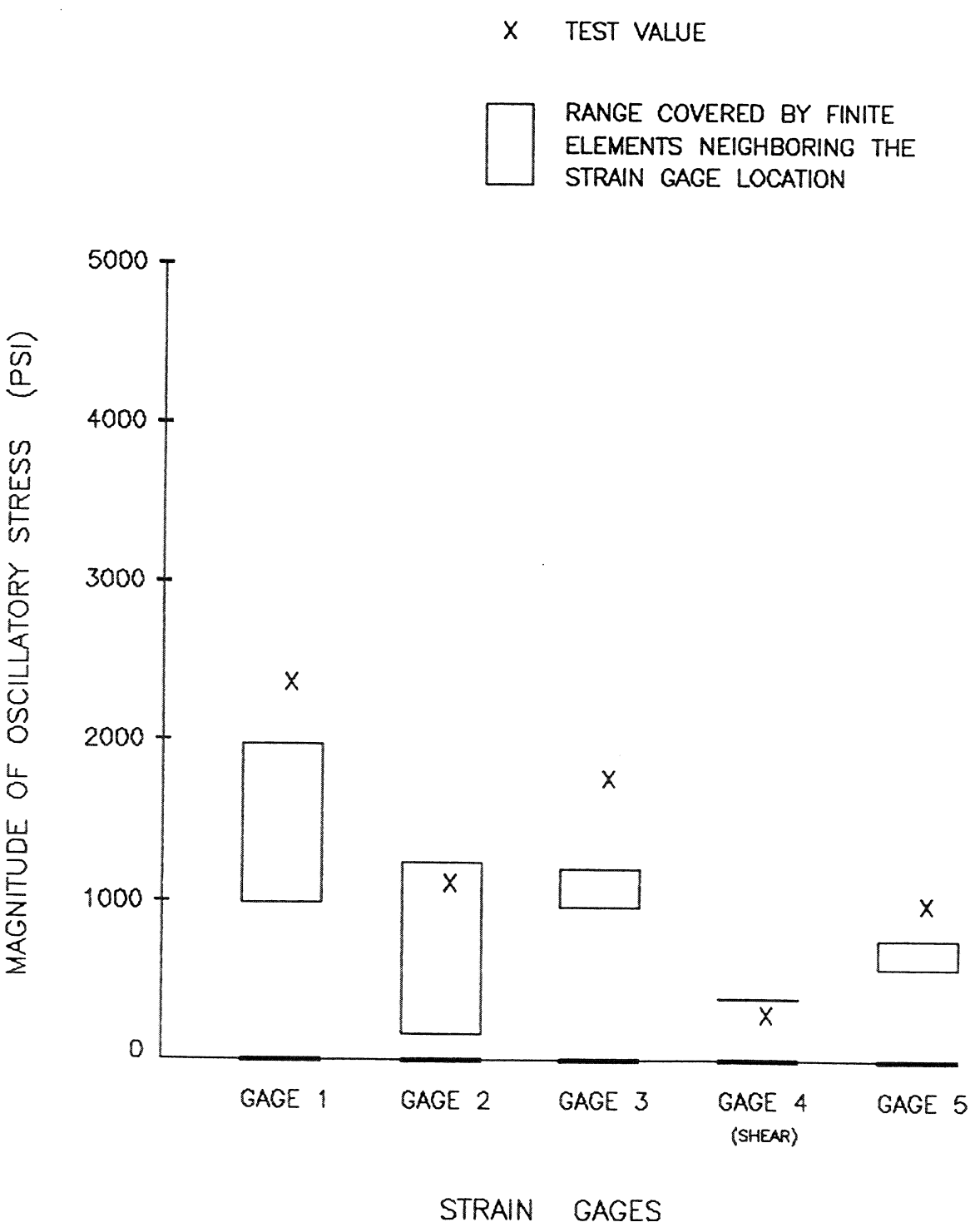

Figure 5.12 SR-3 One-Per-Rev Stress Comparison--Test Reading No. 190

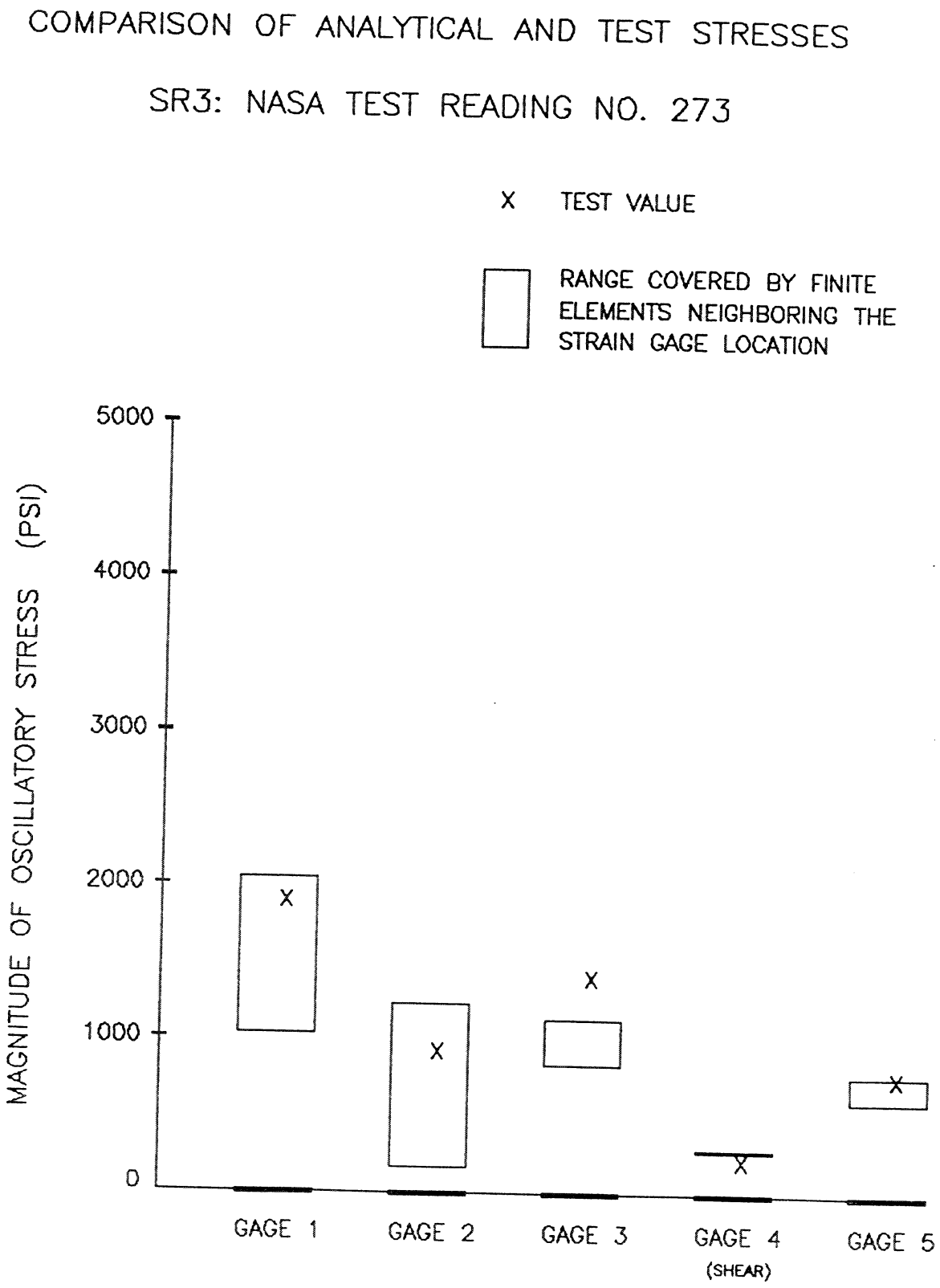

Figure 5.13 SR-3 One-Per-Rev Stress Comparison--Test Reading No. 273

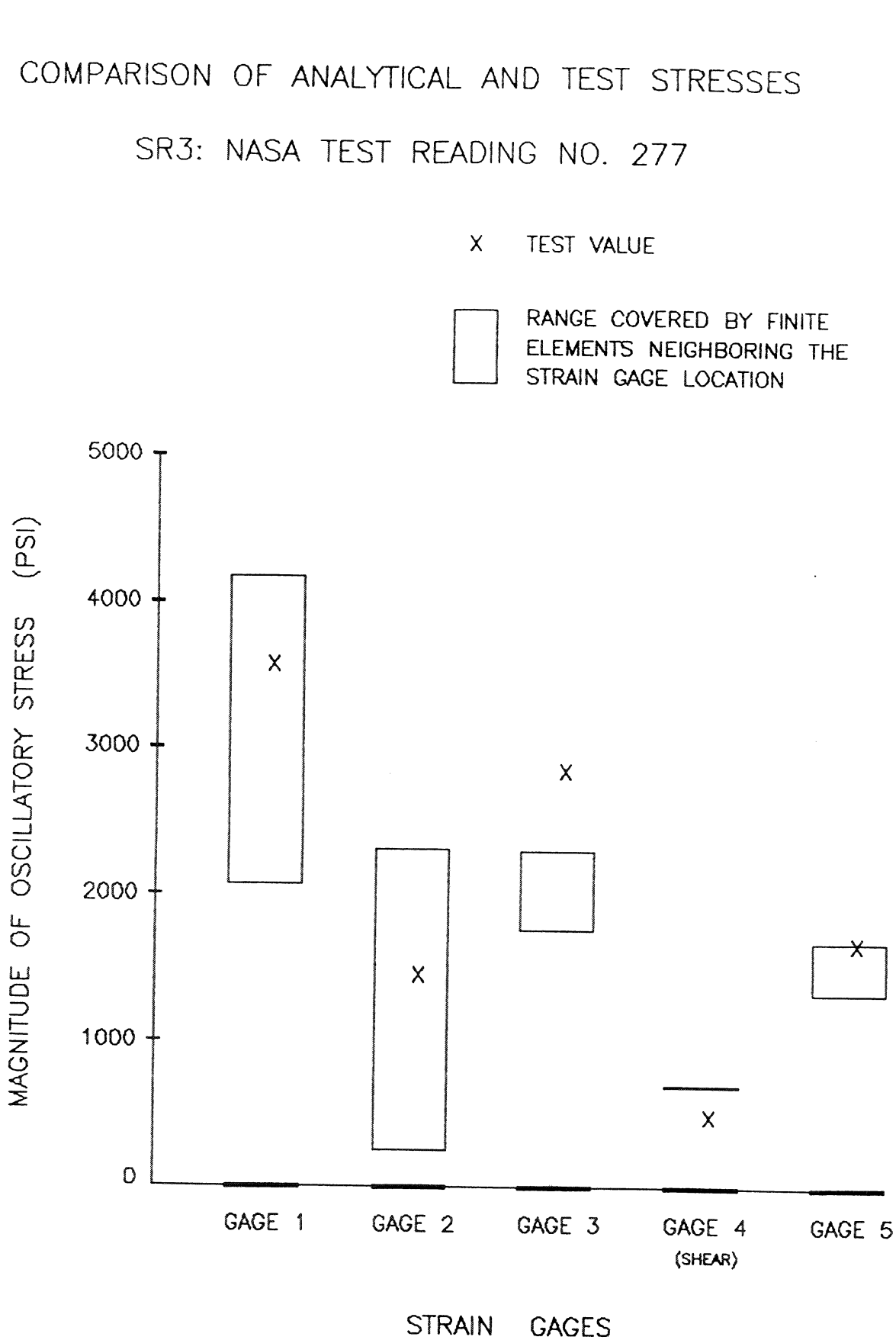

Figure 5.14 SR-3 One-Per-Rev Stress Comparison--Test Reading No. 277

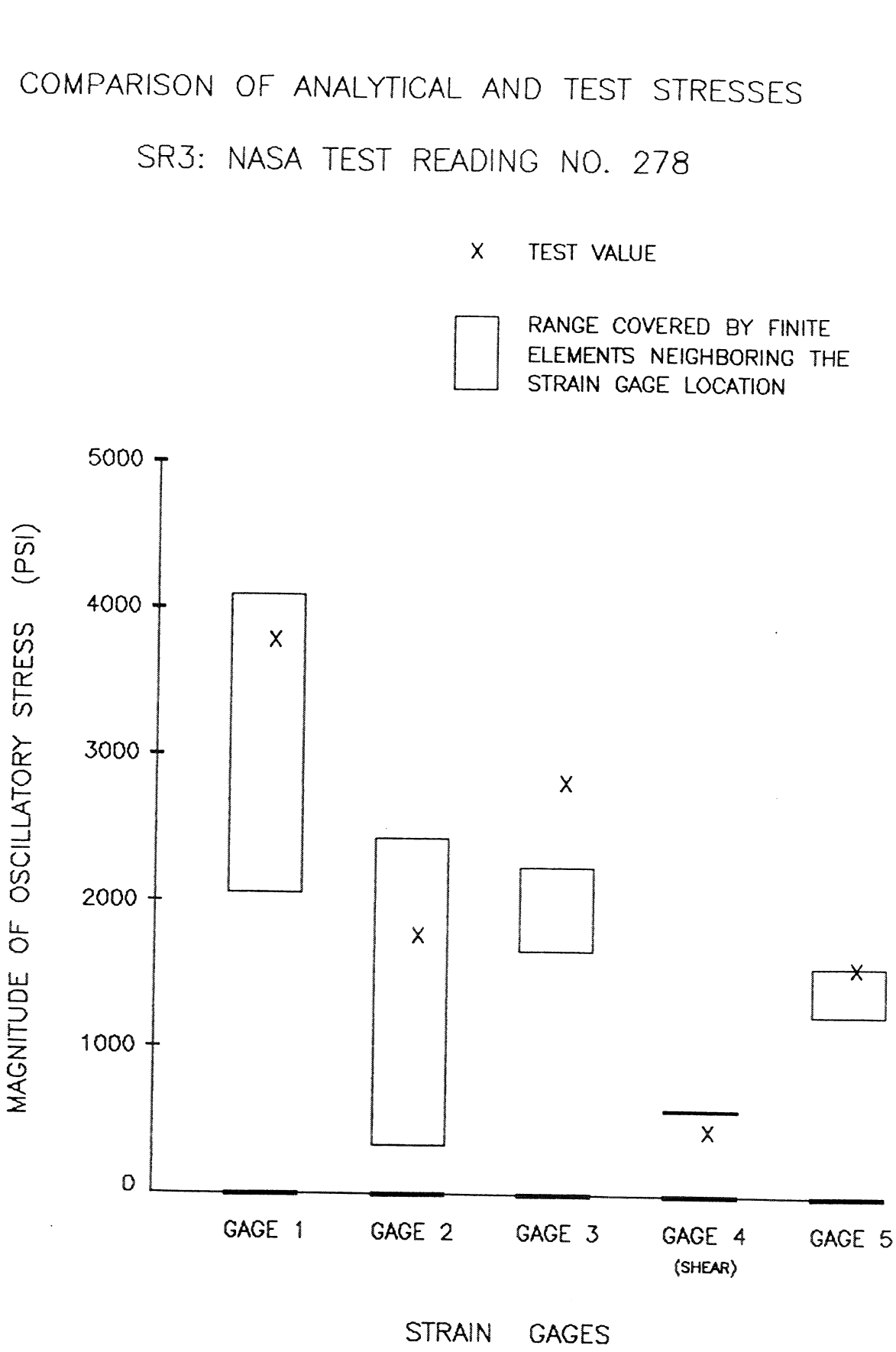

Figure 5.15 SR-3 One-Per-Rev Stress Comparison--Test Reading No. 278

MAX-DEF. = 0.46232789

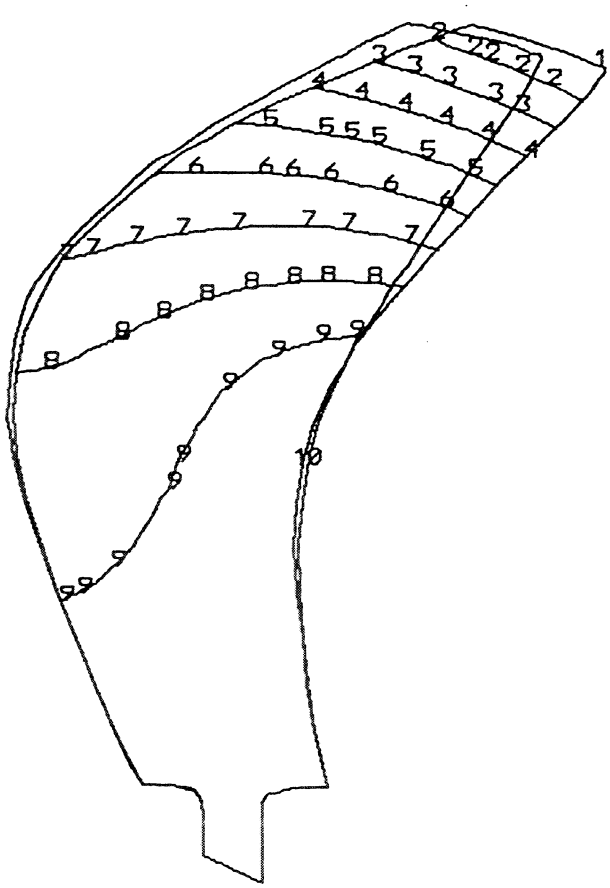

SR5 RESPONSE TO 1 PER REV OSC. AIRLOADS
NASA TEST READING NO. 8508 SOL 4
DIFF. STIFF. ANAL.--LINEAR SOLUTION
STATIC DEFOR. SUBCASE 1 LOAD 1

Figure 5.16 SR-5 Differential Stiffness Analysis--Linear Solution

MAX-DEF. = 0.15929164

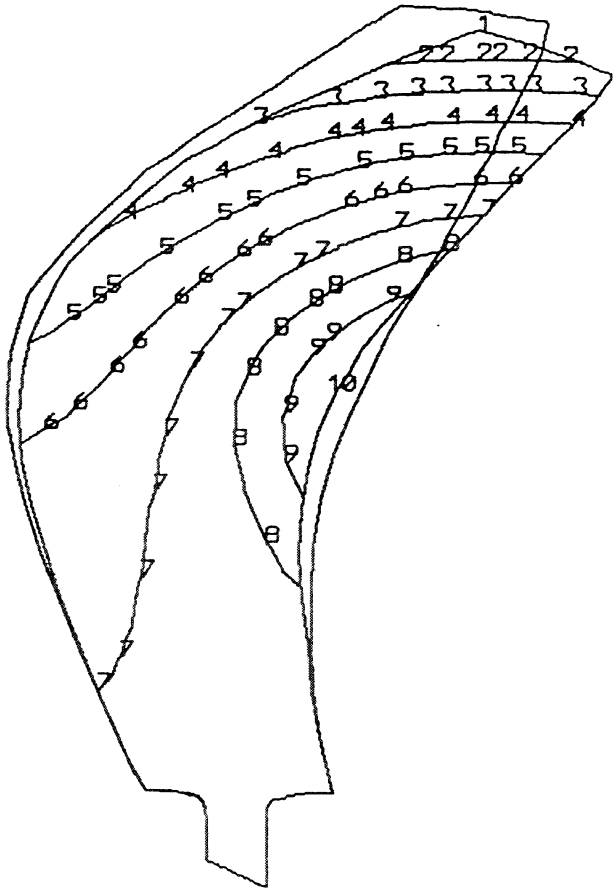

SR5 RESPONSE TO 1 PER REV OSC. AIRLOADS
NASA TEST READING NO. 8508 SOL 4
DIFF. STIFF. ANAL.--NONLINEAR SOLUTION
STATIC DEFOR. SUBCASE 2 LOAD 1

Figure 5.17 SR-5 Differential Stiffness Analysis--Non-Linear Solution

MAX-DEF. = 1.00000000

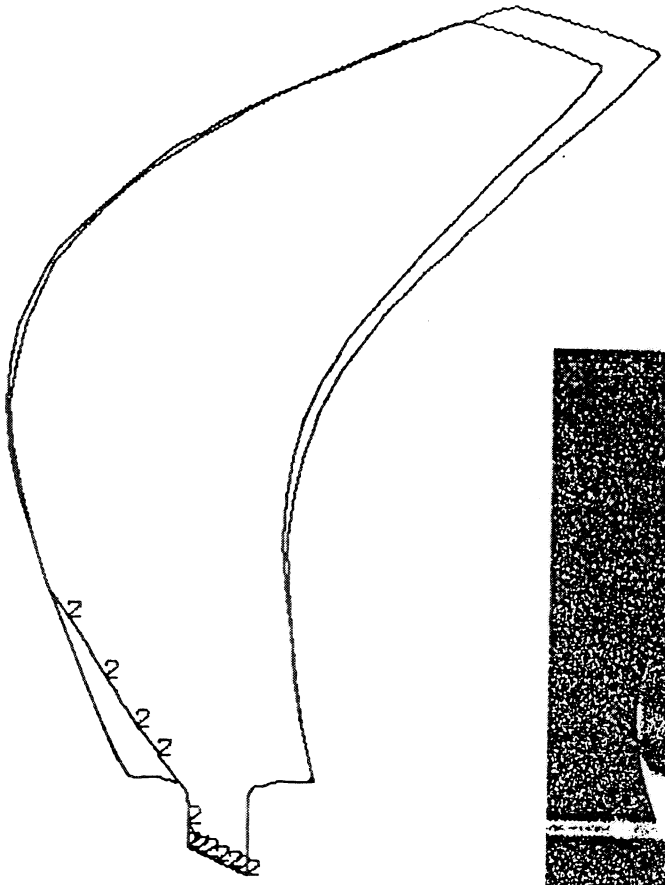

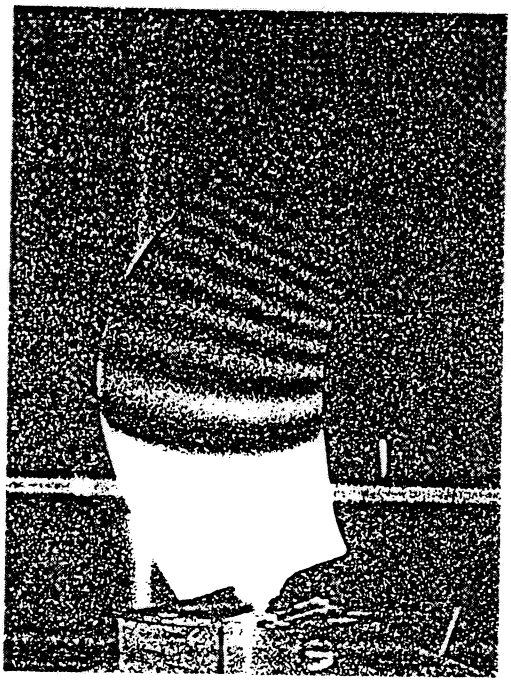

SR5 RESPONSE TO 1 PER REV OSC. AIRLOADS
NASA TEST READING NO. 8508
K = 0 MODES- OSCILLATORY AIRLOADS PRESENT
MODAL DEFOR. SUBCASE 1 MODE 1 FREQ. 140.0948

Figure 5.18 SR-5 Mode 1

MAX-DEF. = 1.00000000

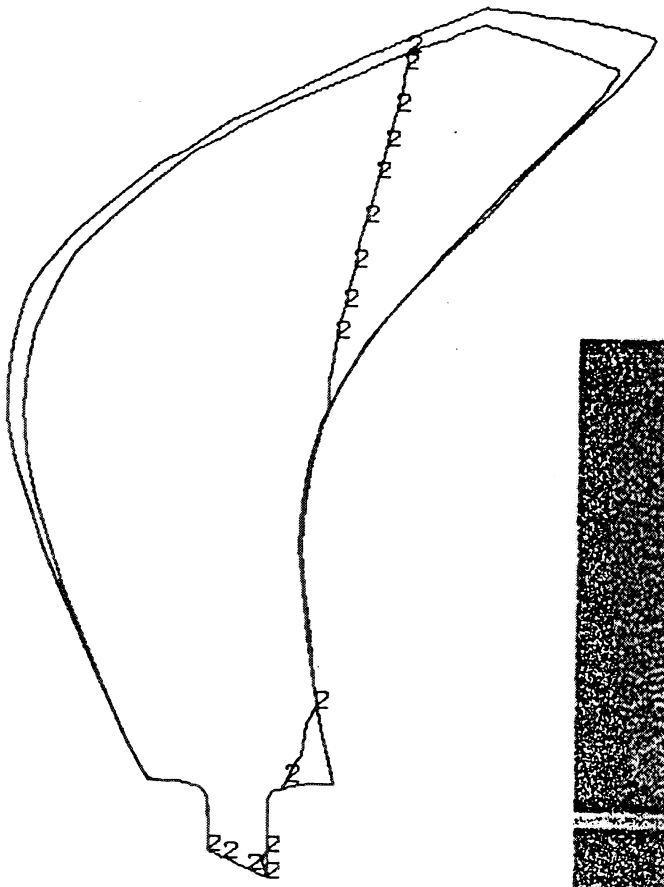

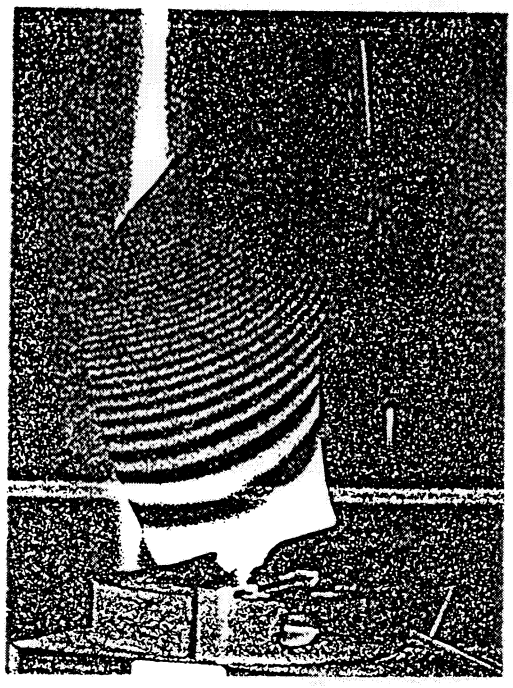

SR5 RESPONSE TO 1 PER REV OSC. AIRLOADS
NASA TEST READING NO. 8508
K = 0 MODES- OSCILLATORY AIRLOADS PRESENT
MODAL DEFOR. SUBCASE 1 MODE 2 FREQ. 275.8804

Figure 5.19 SR-5 Mode 2

MAX-DEF. = 1.00000000

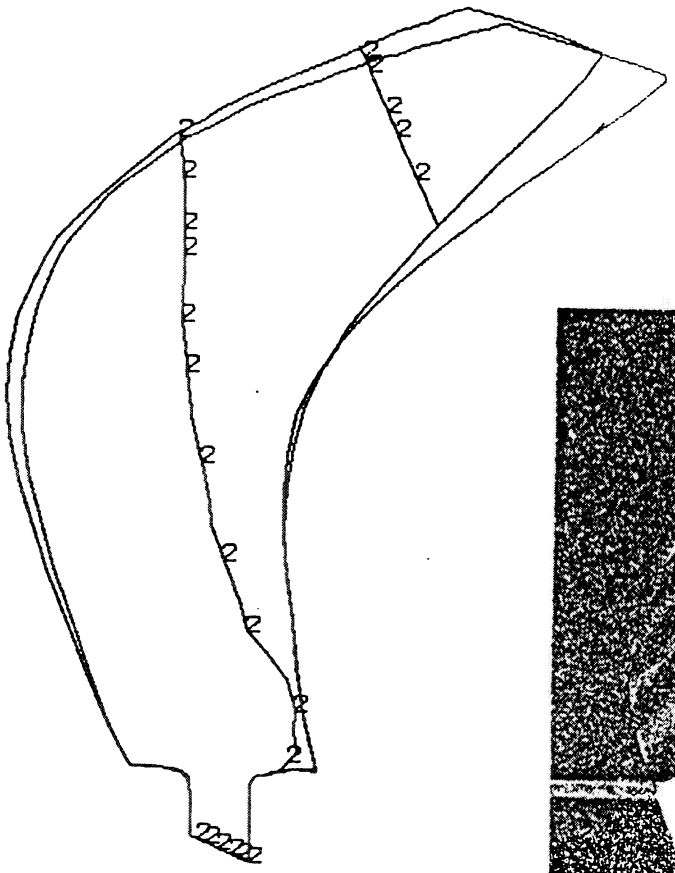

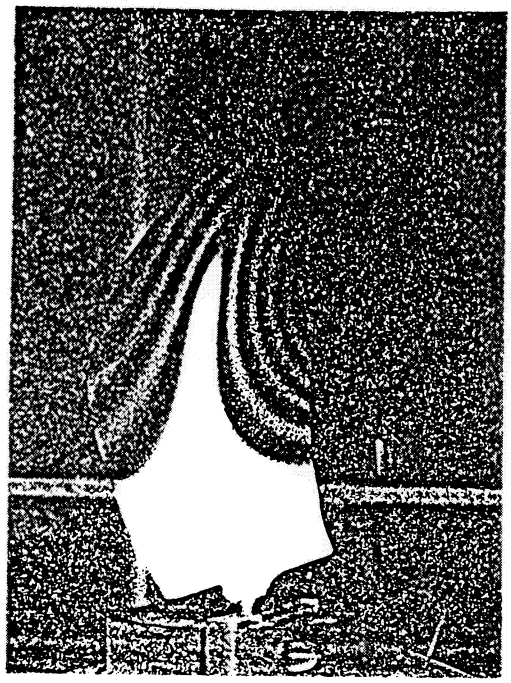

SR5 RESPONSE TO 1 PER REV OSC. AIRLOADS
NASA TEST READING NO. 8508
K = 0 MODES- OSCILLATORY AIRLOADS PRESENT
MODAL DEFOR. SUBCASE 1 MODE 3 FREQ. 558.1463

Figure 5.20 SR-5 Mode 3

MAX-DEF. = 0.74887144

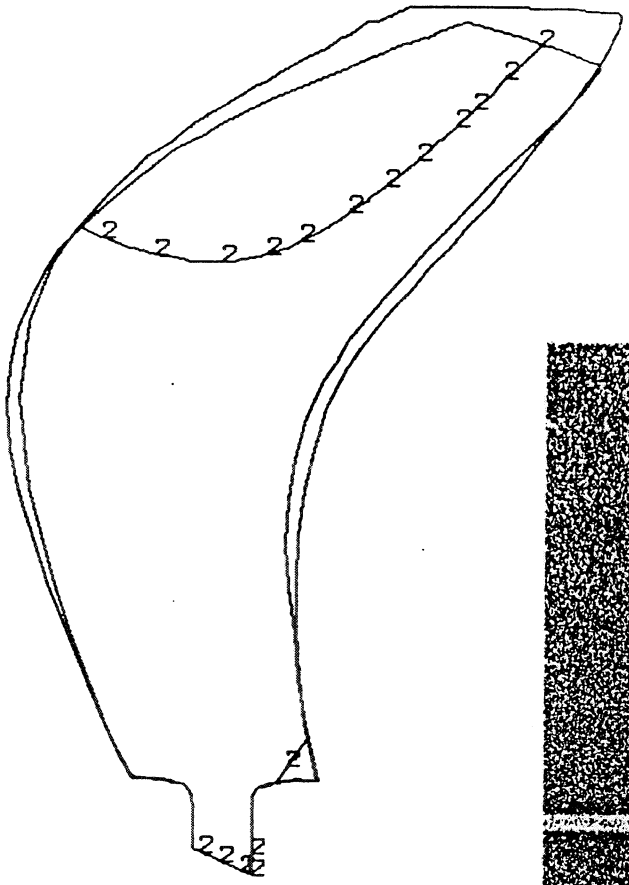

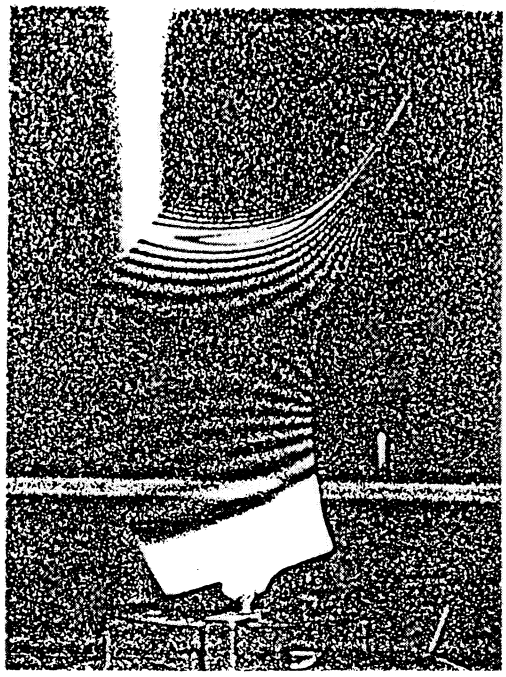

SR5 RESPONSE TO 1 PER REV OSC. AIRLOADS
NASA TEST READING NO. 8508
K = 0 MODES- OSCILLATORY AIRLOADS PRESENT
MODAL DEFOR. SUBCASE 1 MODE 4 FREQ. 650.2884

Figure 5.21 SR-5 Mode 4

MAX-DEF. = 0.96886316

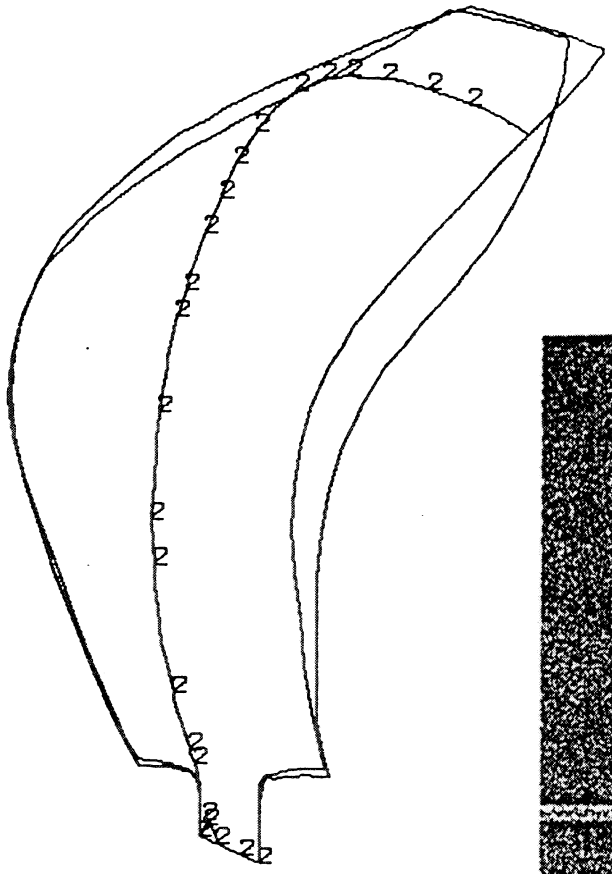

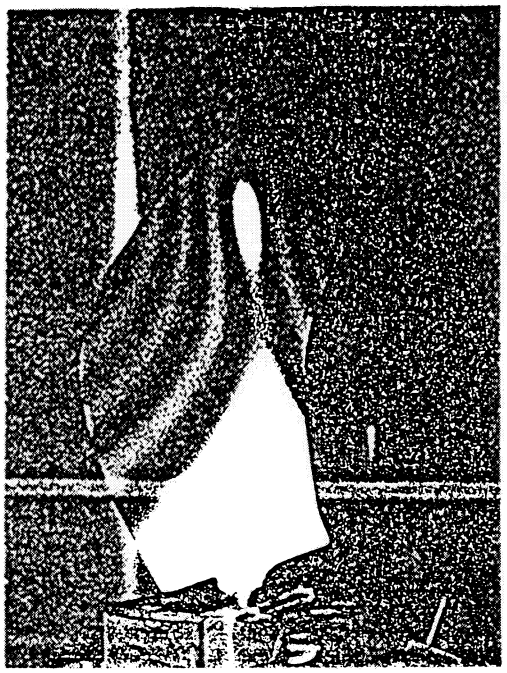

SR5 RESPONSE TO 1 PER REV OSC. AIRLOADS
NASA TEST READING NO. 8508
K = 0 MODES- OSCILLATORY AIRLOADS PRESENT
MODAL DEFOR. SUBCASE 1 MODE 5 FREQ. 718.7901

Figure 5.22 SR-5 Mode 5

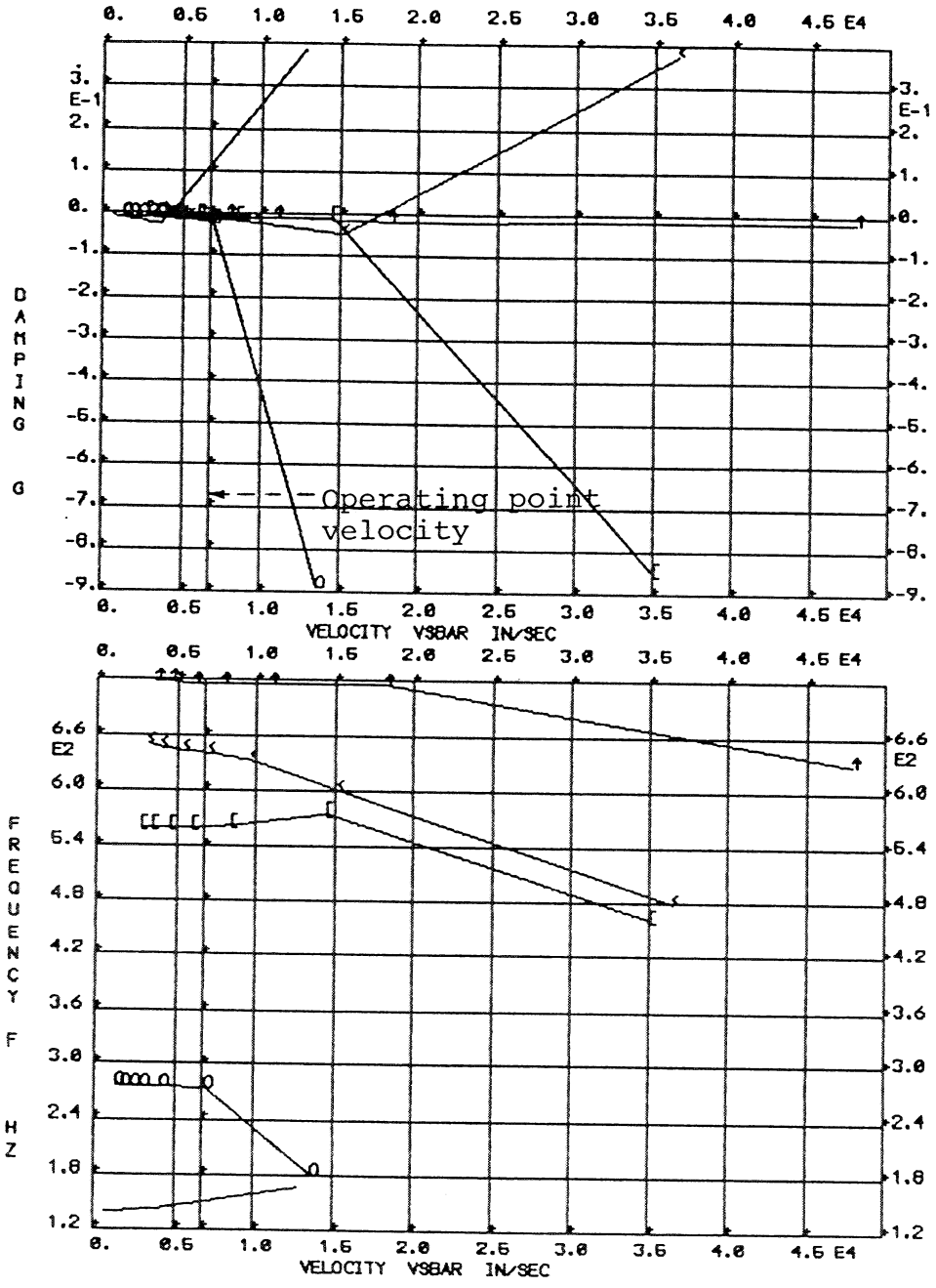

Figure 5.23 SR-5 V-g, V-f Curves
--Test Reading No. 8508

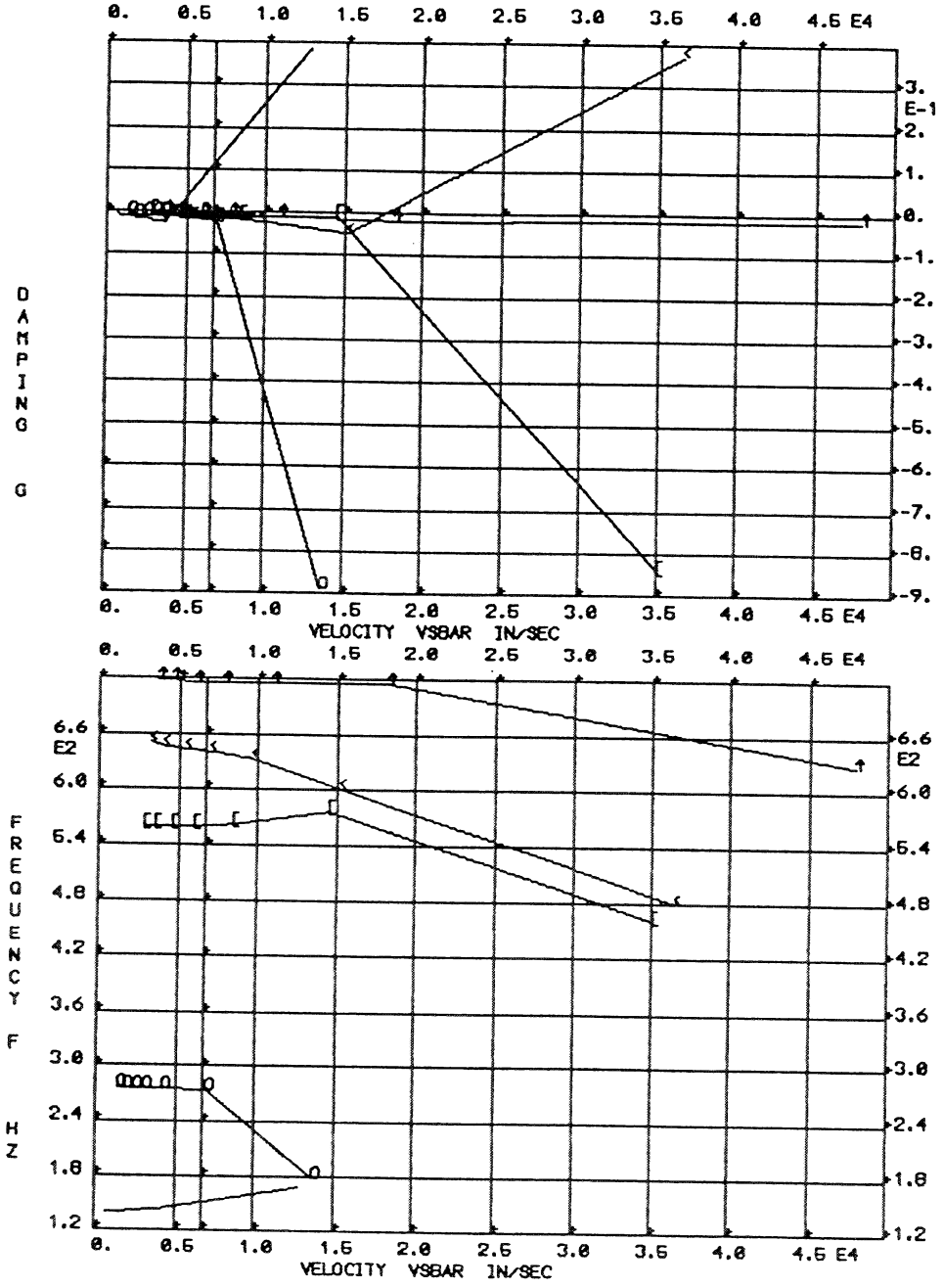

Figure 5.24 SR-5 V-g, V-f Curves
--Test Reading No. 8511

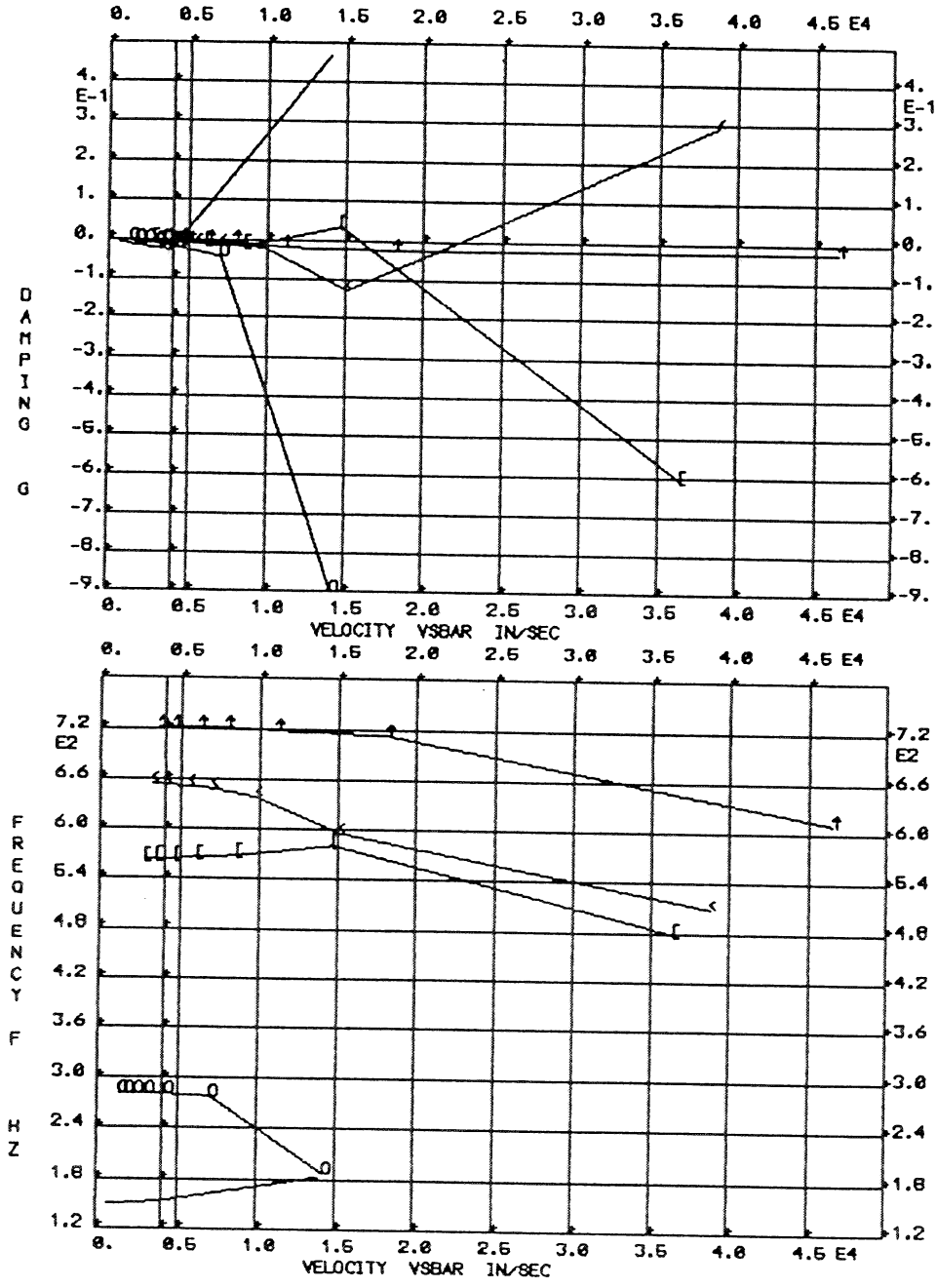

Figure 5.25 SR-5 V-g, V-f Curves
--Test Reading No. 8607

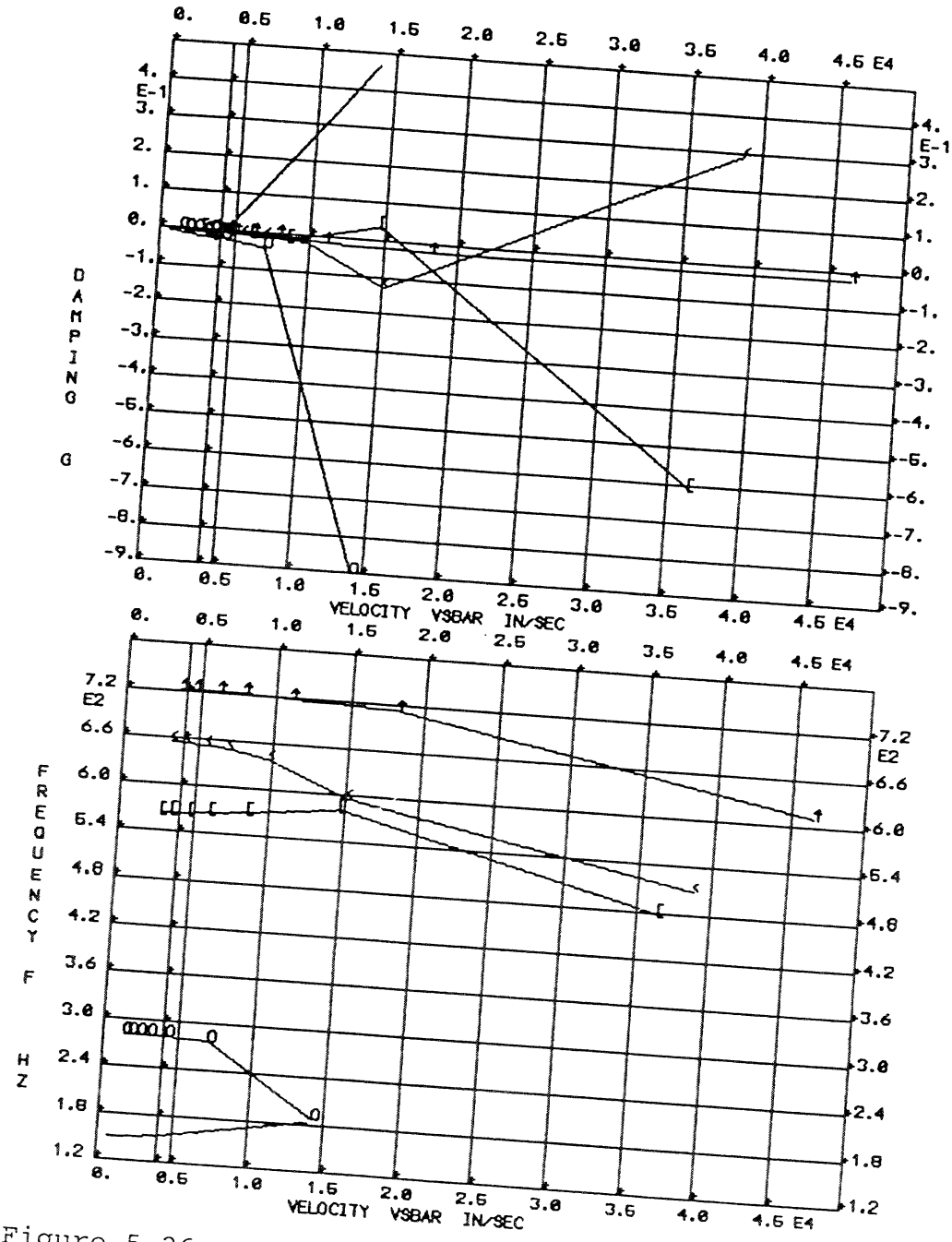

Figure 5.26 SR-5 V-g, V-f Curves
--Test Reading No. 8610

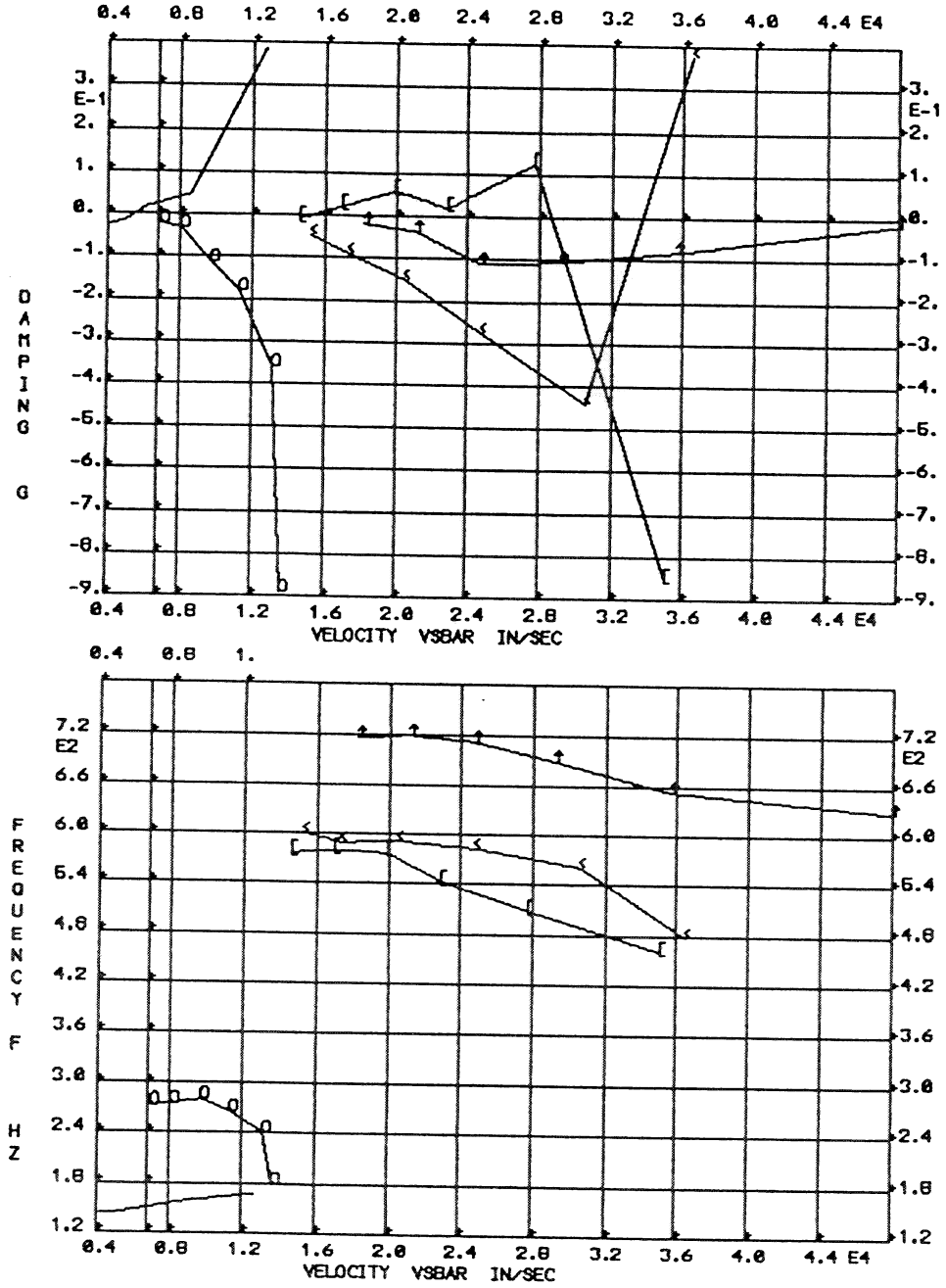

Figure 5.27 SR-5 V-g, V-f Curves with Refined Reduced Frequency Range (.10-.30)--Test Reading No. 8508

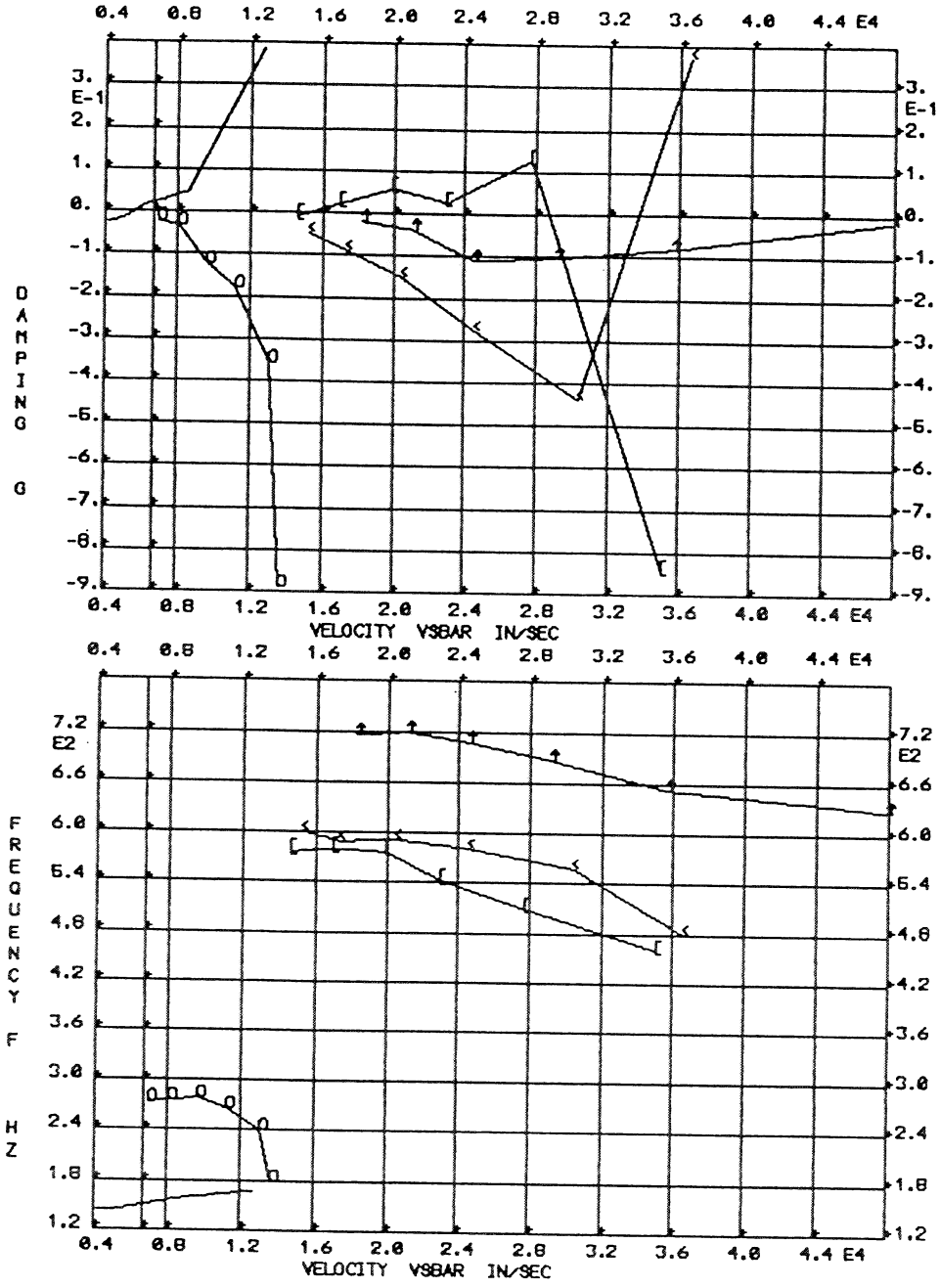

Figure 5.28 SR-5 V-g, V-f Curves with Refined Reduced Frequency Range (.10-.30)--Test Reading No. 8511

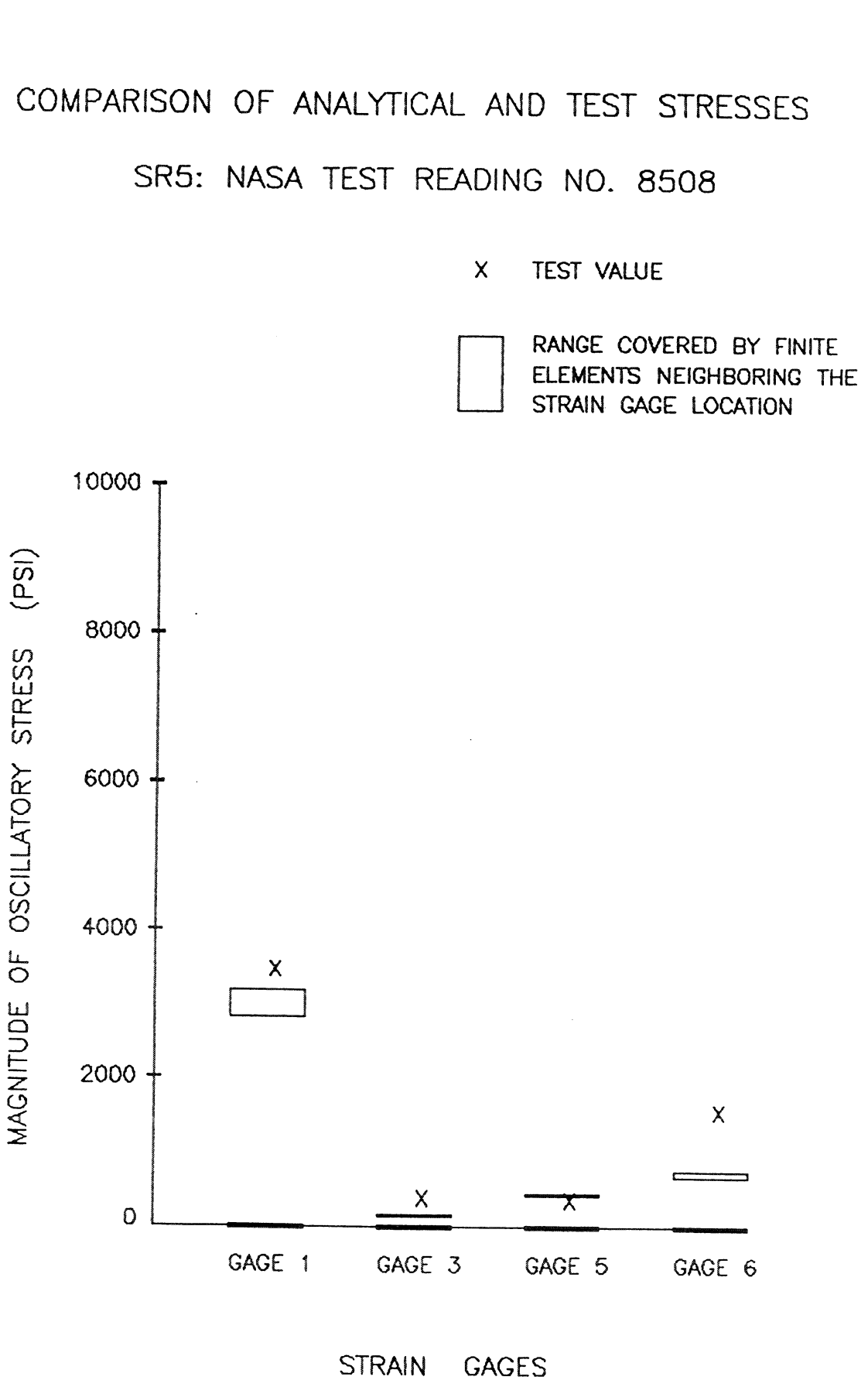

Figure 5.29 SR-5 One-Per-Rev Stress Comparison--Test Reading No. 8508

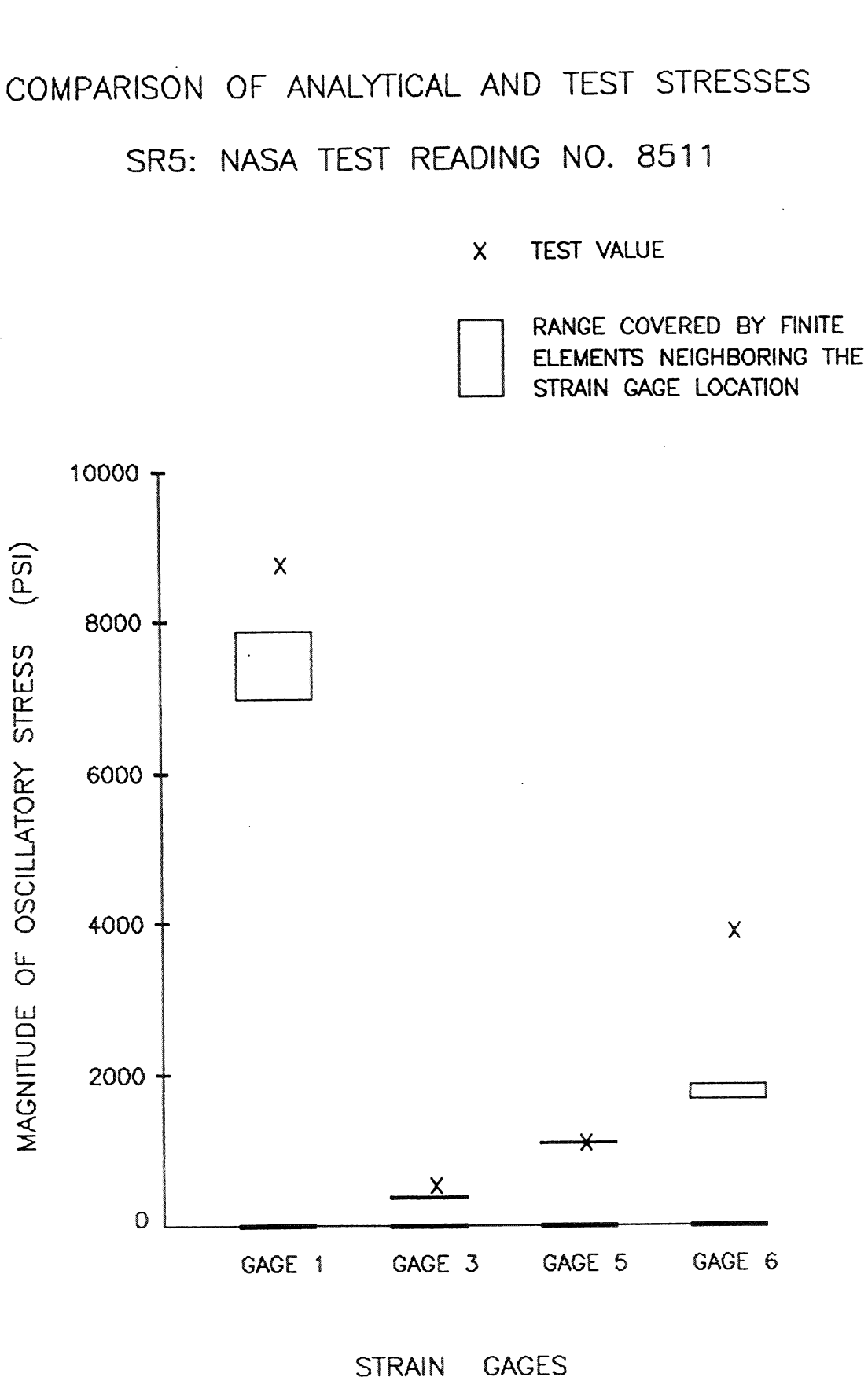

Figure 5.30 SR-5 One-Per-Rev Stress Comparison--Test Reading No. 8511

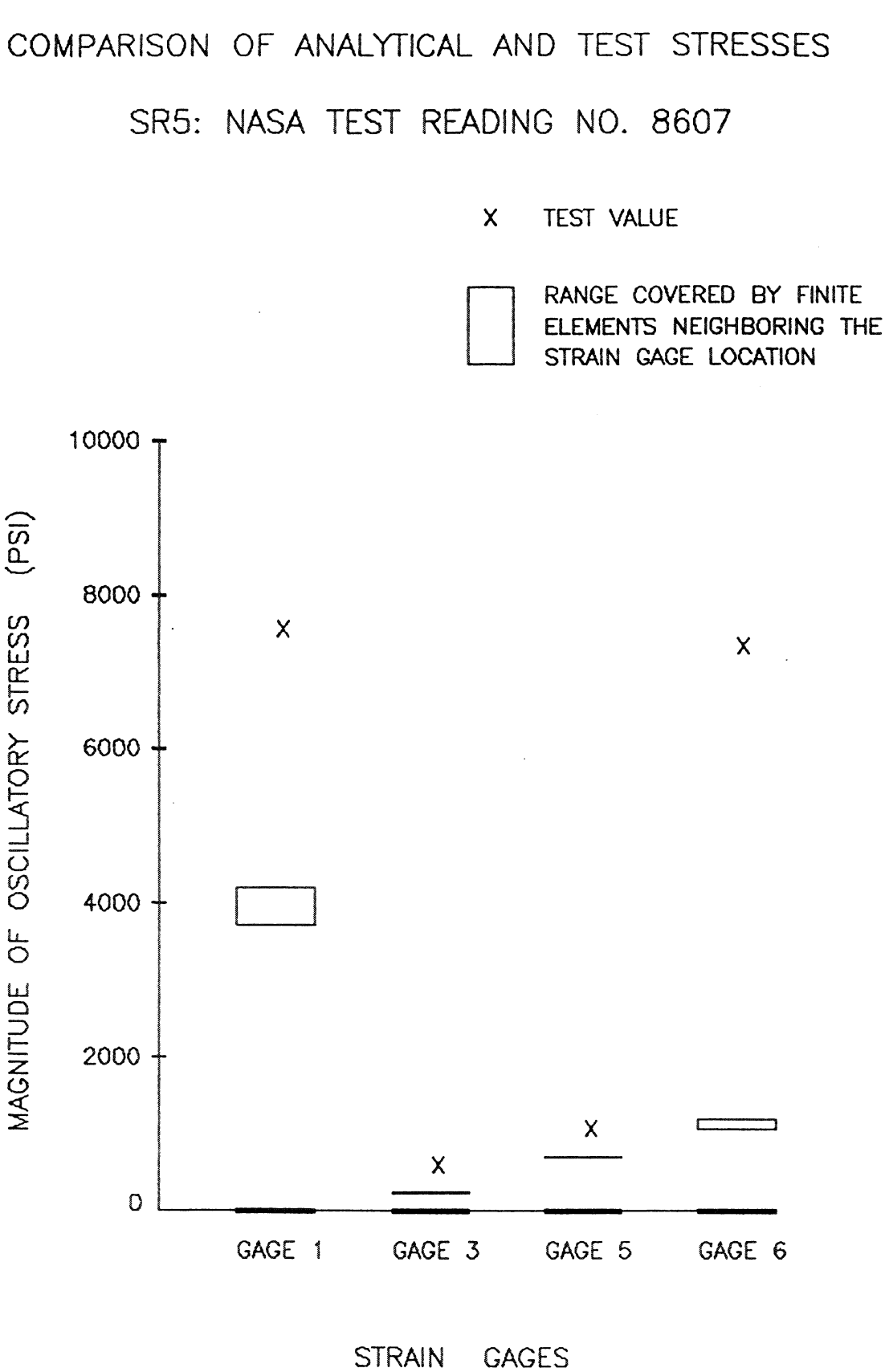

Figure 5.31 SR-5 One-Per-Rev Stress Comparison--Test Reading No. 8607

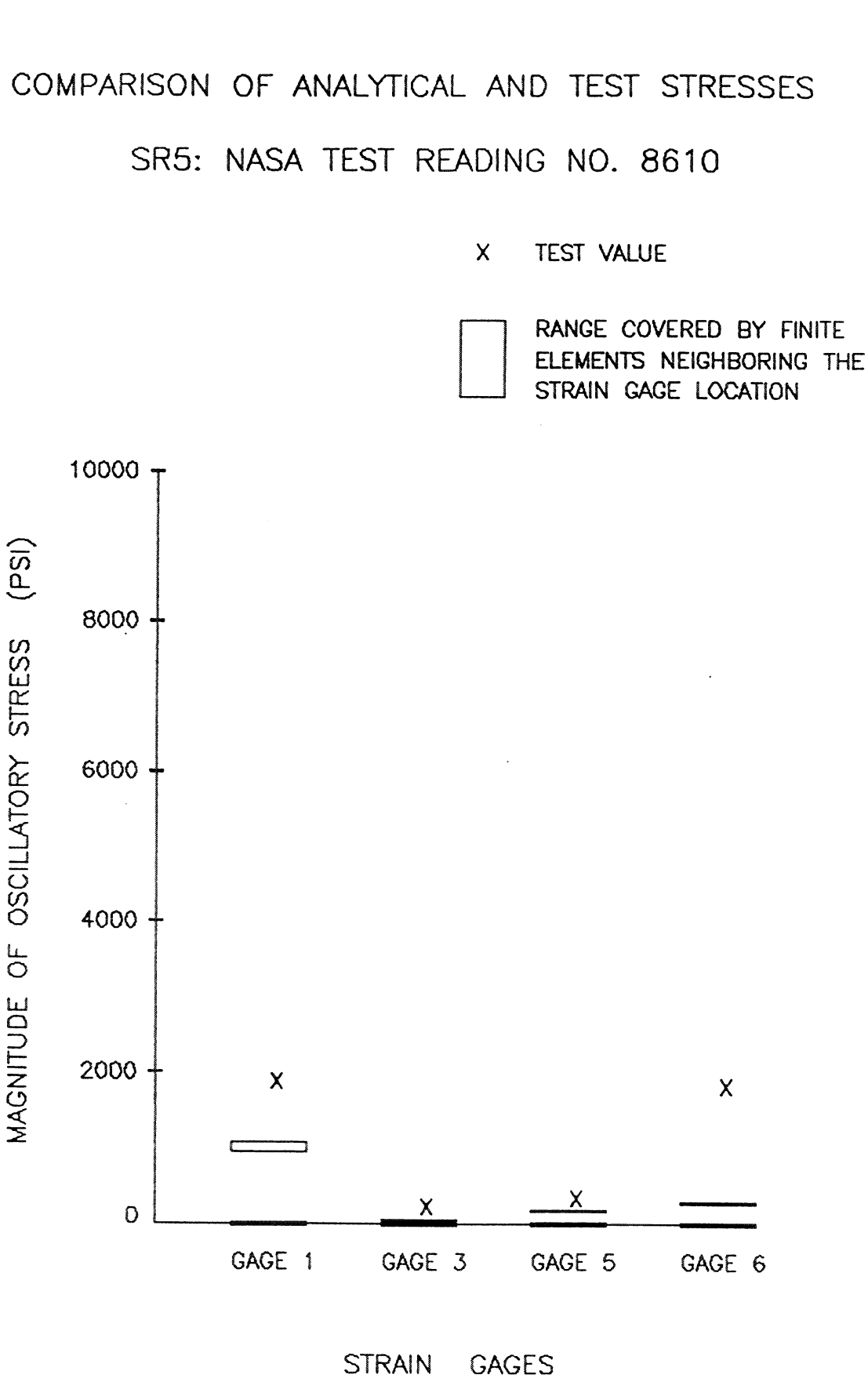

Figure 5.32 SR-5 One-Per-Rev Stress Comparison--Test Reading No. 8610

was conducted principally to save the total (elastic plus differential) stiffness matrix for use in subsequent aeroelastic stability and dynamic response analyses.

5.3 NATURAL FREQUENCIES AND MODE SHAPES

The first five natural frequencies for all SR-3 and SR-5 operating conditions are listed in Table 5.1. These frequencies were obtained by including the effects of differential stiffness and centripetal softening terms.

The only available experimental frequencies are also shown in the Table.

The first five mode shapes for SR-3 test reading no. 190, and SR-5 test reading no. 8508 are shown in Figures 5.3 - 5.7, and 5.18 - 5.22, respectively. These mode shapes were determined at the operating speeds of the turboprops. Inserts of holograms from the bench modal tests (zero rpm) are also included in these Figures. Although the nodal contour patterns can not be directly (and exactly) compared, due to the rpm differences and the Basic coordinate system Y axis not being normal to the blade surface at all points, a broad-based correlation between the calculated and observed mode shapes is indicated in these Figures.

5.4 AEROELASTIC STABILITY

Velocity-damping (V-g) and Velocity-frequency (V-f) curves summarizing the complex eigenvalues of aeroelastic stability

analysis for each of the four operating conditions of the SR-3 turboprop are shown in Figures 5.8 through 5.11.

The first five natural modes were included in the stability analysis conducted by the KE method in NASTRAN. The reduced frequencies were based on the natural frequencies of these modes, and the semichord and cascade relative inflow velocity of the reference chord (Figure 4.3). No structural damping was assumed. The cascade relative inflow velocity on the reference chord defining the operating point is shown by a vertical line in each of the V-g, V-f plots. The aeroelastic stability of the operating point is established by a negative damping value for each of the structural modes at the operating point velocity (vertical line).

This is observed to be true in all of the SR-3 operating conditions (Figures 5.8 through 5.11).

The V-g, V-f curves for the four SR-5 operating conditions are presented in Figures 5.23 through 5.26.

In these cases too, the first five structural modes were considered in the aeroelastic stability calculations. No structural damping was assumed.

While the operating points 8607 and 8610 (Figures 5.25 and 5.26) are seen to be stable, aeroelastic instability is indicated at the 8508 and 8511 test conditions (Figures 5.23 and 5.24) by the positive damping value in structural mode 1. To highlight the damping distribution in this mode near the operating velocity,

these two cases were further analyzed by selecting a finer reduced frequency range (.1 to .3) about the first structural mode frequency. The resulting V-g, V-f plots are shown in Figures 5.27 (8508) and 5.28 (8511). A positive aerodynamic damping value of about 2% is indicated in mode 1 for both of these curves. With the assumption of 2-3% structural damping present in the turboprop blades, the 8508 and 8511 test conditions can be treated as marginally subcritical operating points. A uniform structural damping value of 3% was used in the response calculations at these two operating conditions.

5.5 VIBRATORY RESPONSE TO AERODYNAMIC EXCITATION

The aerodynamic excitation in all of the eight examples is due to the turboprop axis of rotation being misaligned with the uniform inflow. Hence, the only excitation frequency is the one-per-rev value for each of the operating conditions. Magnitudes of the one-per-rev oscillatory stress response of the SR-3 and SR-5 turboprops at the strain gage locations with available wind tunnel data are shown in Figures 5.12 - 5.15, and 5.29 - 5.32 respectively. (Strain gages are identified in Figures 4.1 (SR-3) and 4.2 (SR-5)).

A range of stress values covered by the finite elements neighboring a strain gage location is plotted for direct comparison with the measured value.

The first five structural modes in each case were included in the response calculations.

In regards to the comparison of calculated and measured stresses, the following points are noted:

1. In modal forced response analysis, the calculated stress response is essentially determined by the following factors:

    a. modal frequencies,

    b. modal stresses,

    c. modal damping,

    d. excitation frequencies, and

    e. excitation levels.

2. If the excitation frequencies are well separated from the modal frequencies, the modal damping exerts insignificant influence on the stress response.

3. If only one excitation frequency exists, and is placed well below the first modal frequency, the principal, and significant, contribution to the response stresses comes from the modal stresses of the first mode.

4. The contributing modal stresses are 'scaled' by the excitation levels to the calculated response stresses.

5. Keeping in view the above 4 points, the following observations are made in the eight SR-3 and SR-5 examples:

    a. The only one-per-rev excitation frequency in each case is well below the first modal frequency as

summarized in Table 5.2 .

b. This implies the insignificance of modal damping, and the significance of modal stresses of the first structural mode toward computing the response stresses.

Figure 5.33 illustrates the striking similarities between the calculated stress responses of all four SR-3 cases. Gage-to-gage stress distribution for each case (Figures 5.12 - 5.15) is normalized with the mean stress of gage 1 in that case. These stress distributions are also noted to closely resemble those exhibited by the modal stresses in the first structural mode.

Figure 5.34 shows a similar relation between the calculated stress responses of all four of the SR-5 cases.

c. The one-per-rev applied oscillatory airloads distribution effectively scales the modal stresses in the first mode to the calculated response stresses.

6. While an across the board inspection of comparisons of calculated and measured stresses in all eight cases reveals a generally good correlation, some specific deviations are noted as follows:

a. In all SR-3 cases, gage 3 measurements are higher than predictions. This may be due to discrepancies in strain measurements or strain-gage orientation. The finite element model (Figure 4.3) does not reflect

Table 5.2 Comparison of Excitation and Modal Frequencies

Turboprop Blade	NASA Test Rdg. No.	Excitation Frequency, Hz.	Modal Frequencies, Hz.	
			Mode 1	Mode 2
SR-3	190	133	227	431
	273	133	220	423
	277	117	210	417
	278	133	220	423
SR-5	8508	92	140	275
	8511	92	140	275
	8607	100	150	281
	8610	100	150	281

COMPARISON OF CALCULATED STRESS RESPONSES

SR-3: ALL CASES

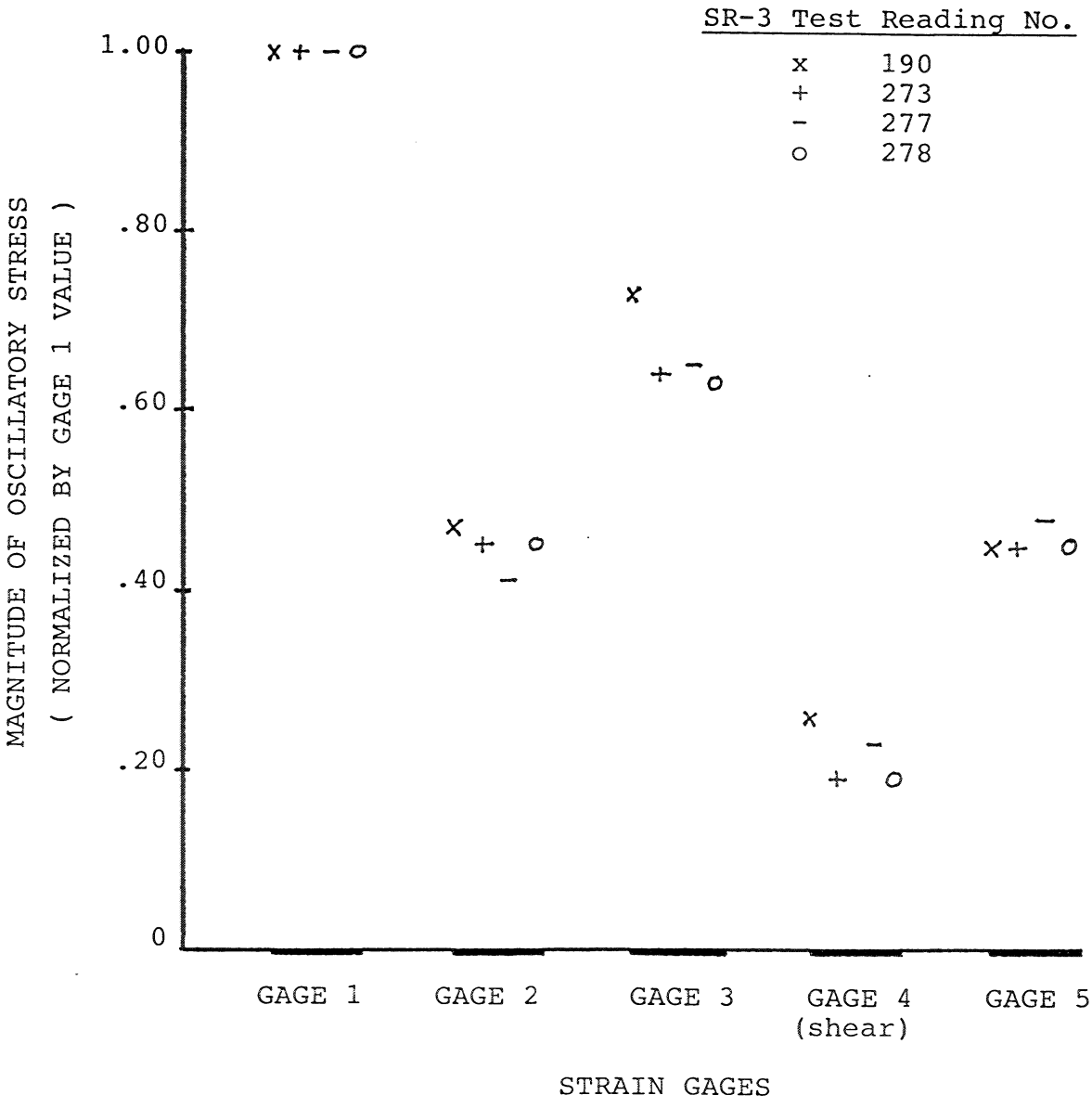

Figure 5.33 SR-3 One-Per-Rev Calculated Stress Response Comparison Between Cases

COMPARISON OF CALCULATED STRESS RESPONSES

SR-5: ALL CASES

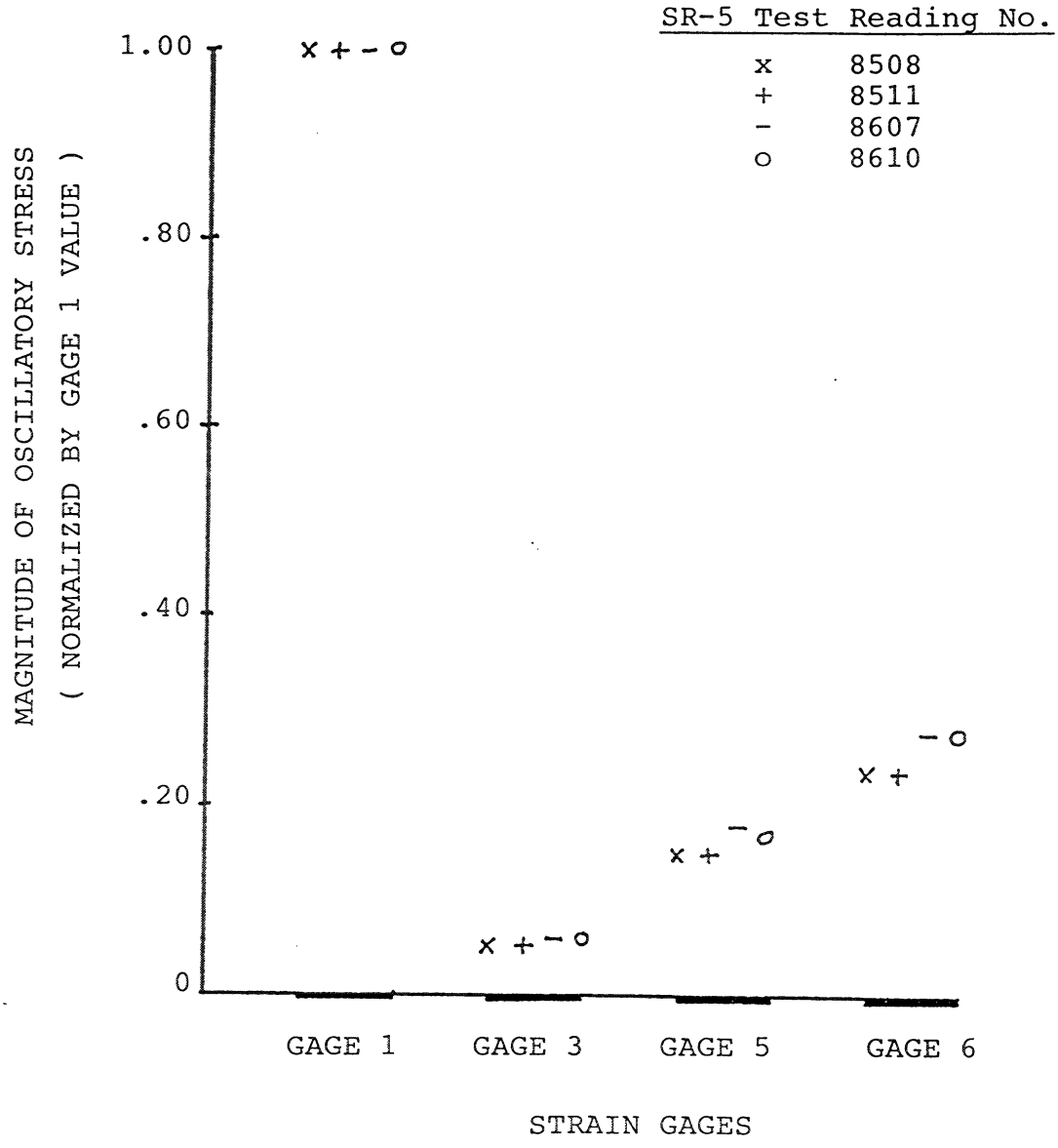

Figure 5.34 SR-5 One-Per-Rev Calculated Stress Response Comparison Between Cases

abnormal element connections or boundaries in this region.

b. Similar observations can be made for gage 6 in SR-5 cases.

c. Test cases with a combination of low (.35 - .36) Mach numbers (SR-3 190, SR-5 8607 and 8610), high tilt angles (SR-3 190 and SR-5 8607), and very highly swept blades (SR-5 8607) may be more sensitive to the aerodynamic modelling of the tip regions of the blade. This, in turn, affects the applied oscillatory airloads, ultimately altering the vibratory stress response. Spacing, number, and orientation of streamlines in such regions of the blade are some of the variables of the aerodynamic model which will provide a good basis for any sensitivity investigations.

6. CONCLUSIONS

1. Theoretical developments of a new capability in NASTRAN for modal forced vibration analysis of aerodynamically excited turbosystems have been described.

2. The capability has been successfully applied to eight NASA wind tunnel test conditions of the SR-3 and SR-5 advanced turboprops for predicting the vibratory response of the turboprop blades.

3. NASTRAN pre-processing capability of the stand-alone AIRLOADS program has been successfully utilized in generating the applied oscillatory airloads on the swept blades of the advanced turboprops.

7. RECOMMENDATIONS

The application examples conducted in the present work have been for single-rotation advanced turboprops at a number of operating conditions. Two or three of these eight cases have indicated a need for analyzing refined aerodynamic models in improving predictions.

It would prove useful to,

1. study the aerodynamic model variations as they affect the applied airloads and response predictions, and

2. apply the capability to analyze forced vibrations of other turbosystems such as counter-rotating turboprops and axial-flow turbomachines.

APPENDIX A

SWEEP EFFECTS IN SUPERSONIC AIRLOADS DUE TO OSCILLATORY BLADE MOTIONS

A.1 GENERAL

The generalized modal aerodynamic force matrix Q_{ii} due to oscillatory motions of the swept blades of advanced turbopropellers is derived. The two-dimensional supersonic cascade unsteady aerodynamics program of Ref. 11 has been modified to include the effects of blade sweep. The modifications are similar to those carried out for subsonic flow (Ref. 6). The blade is spanned by a number of non-intersecting chords selected normal to any spanwise reference curve such as the blade leading edge (Figure A.1). The modified subsonic or supersonic two-dimensional cascade theory is applied on each of these chords to determine the generalized aerodynamic forces acting on the associated strip. The strip results are added to obtain the blade aerodynamic matrix. This Appendix discusses the sweep changes in supersonic aerodynamics. Those for subsonic flow are contained in Ref. 6.

In order to conform to the existing computational scheme in the Bladed Disks Computer Program, and thus reduce extensive recoding, the chordwise generalized aerodynamic matrices are first computed for predefined, simple, chordwise aerodynamic modes (Figure A.2). The chordwise structural modes are then

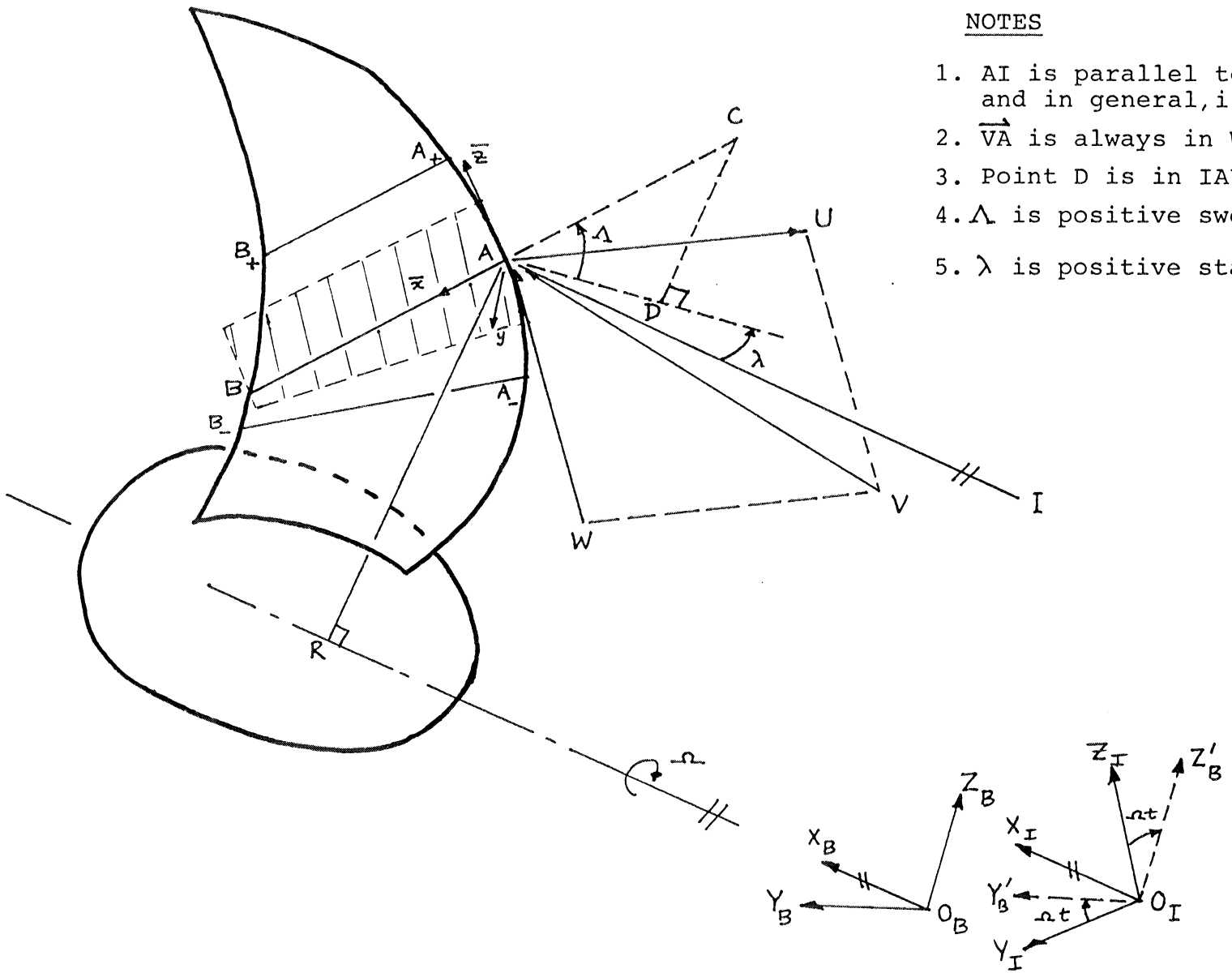

NOTES

1. AI is parallel to axis of rotation, and in general, is NOT in WAU plane
2. $\overrightarrow{VA}$ is always in WAU plane
3. Point D is in IAU plane
4. Λ is positive sweep angle
5. λ is positive stagger angle

Figure A.1 Some Definitions for Swept Blade Aerodynamics

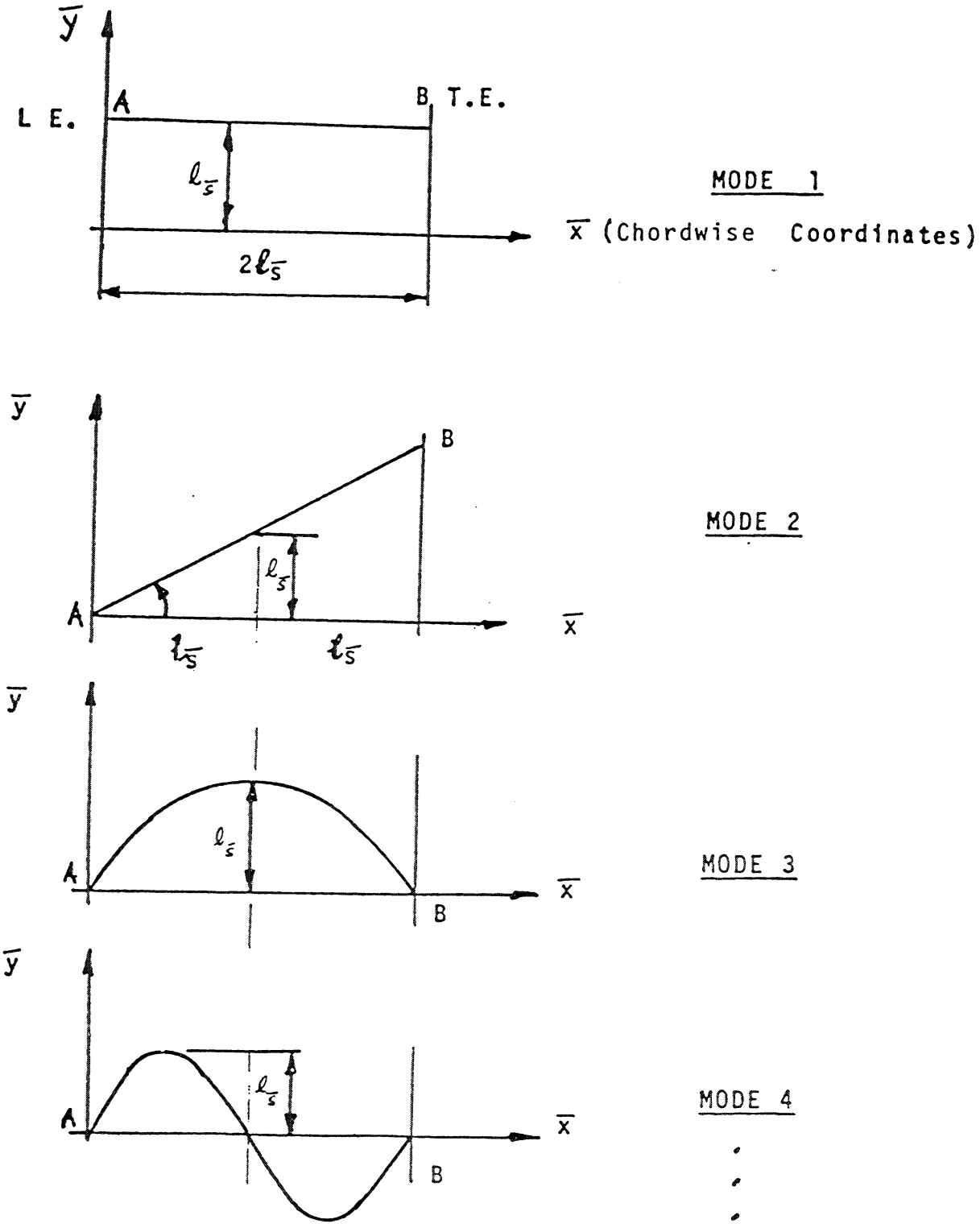

Figure A.2 Chordwise Aerodynamic Modes

introduced via Fourier expansions to finally obtain the blade generalized airforce matrix.

A.2 DEFINITIONS

Figure A.1 illustrates some of the definitions pertinent to incorporating sweep effects in the 2-d cascade programs. A_-B_-, AB and A_+B_+ represent three successive chords with points A's on the leading edge. For the chord AB, at any operating condition $\overrightarrow{WA}$ represents the absolute inflow velocity while $\overrightarrow{AU}$ (= $\vec{\Omega}$ x $\overrightarrow{RA}$) is the blade (tangential) velocity.

In the plane WAU, $\overrightarrow{VA} = \overrightarrow{WA} - \overrightarrow{AU}$ represents the relative inflow velocity.

AI is parallel to the axis of rotation, and does not, in general, lie in the WAU plane.

AD is the projection of AC (BA extended arbitrarily to C) in plane IAU.

The sweep angle Λ, and the stagger angle λ are positive as shown.

A local coordinate system $\bar{x}\bar{y}\bar{z}$ is defined at the leading edge point A of the chord AB such that $\bar{x}$ is directed along AB. $\bar{y}$ is defined normal to the 'mean' surface containing the points A_-, A, A_+, B_+, B, and B_-. The unit vector along $\bar{y}$, for the sense of Ω shown in Figure A.1 is given by

$$\hat{\bar{j}} = \frac{1}{2}\left[\frac{(\overrightarrow{A_-B_+}) \times (\overrightarrow{AB})}{|(\overrightarrow{A_-B_+}) \times (\overrightarrow{AB})|} + \frac{(\overrightarrow{AB}) \times (\overrightarrow{A_+B_-})}{|(\overrightarrow{AB}) \times (\overrightarrow{A_+B_-})|}\right] \qquad (A1)$$

Modal translations along $\bar{y}$ and rotations about $\bar{x}$ are used in deriving the generalized airforce matrix (Section A.6). For the opposite sense of rotation, $\bar{x}\bar{y}\bar{z}$ is defined to be left handed with $\bar{y}$ reversing direction.

The shaded area about the chord AB represents the strip of integration associated with AB. The length of the strip is given by AB, the widths at the leading and trailing edges are respectively given by

$$\left.\begin{aligned} w_{l.e.} &= \tfrac{1}{2}\left(\overrightarrow{A_- A_+}\right)\cdot\hat{\bar{k}} \quad , \text{ and} \\ w_{t.e.} &= \tfrac{1}{2}\left(\overrightarrow{B_- B_+}\right)\cdot\hat{\bar{k}} \end{aligned}\right\} \qquad (A2)$$

where $\hat{\bar{k}}$ is the unit vector along $\bar{z}$.

A.3 BLADE DEGREES OF FREEDOM

For aerodynamic computations, consider the blade to be spanned by $\bar{S}$ chords with G structural grid points on each chord. The blade degrees of freedom $\{u\}$ can then be partitioned as

$$\{u\} = \begin{Bmatrix} u_1 \\ \hline u_2 \\ \hline \vdots \\ \hline u_{\bar{s}} \\ \hline \vdots \\ \hline u_{\bar{S}} \end{Bmatrix} , \qquad (A3)$$

where

$$\{u_{\bar{s}}\} = \begin{Bmatrix} u_{\bar{s}1} \\ u_{\bar{s}2} \\ \vdots \\ u_{\bar{s}g} \\ \vdots \\ u_{\bar{s}G} \end{Bmatrix} \qquad (A4)$$

$u_{\bar{s}g}$ represents the 3 translational and 3 rotational degrees of freedom at grid point g on chord $\bar{s}$.

A.4 NORMAL DISPLACEMENT, DOWNWASH AND PRESSURE DISTRIBUTION IN TERMS OF CHORDWISE AERODYNAMIC MODES

The normal displacement (along + $\bar{y}$) at any point $\bar{x}$ on the chord $\bar{s}$ can be expressed in the local (chord) coordinate system as a linear combination of the chordwise aerodynamic modes:

$$u^{\bar{s}n}(\bar{x}, \bar{z}, t) = \ell_{\bar{s}}(\bar{z}) \left\lfloor \Phi^{\bar{s}}(\bar{x}/\ell_{\bar{s}}) \right\rfloor \left\{\eta^{\bar{s}1}(\bar{z})\right\} e^{i\omega t} \qquad (A5)$$

where $\ell_{\bar{s}}$ is the semi-chord,

$$\left\lfloor \Phi^{\bar{s}} \right\rfloor = \left\lfloor 1 \quad \frac{\bar{x}}{\ell_{\bar{s}}} \quad \sin\left(\frac{\overline{3-2}\cdot\pi\cdot\bar{x}}{2\ell_{\bar{s}}}\right) \cdots \sin\left(\frac{\overline{g-2}\cdot\pi\cdot\bar{x}}{2\ell_{\bar{s}}}\right) \cdots \sin\left(\frac{\overline{G-2}\cdot\pi\cdot\bar{x}}{2\ell_{\bar{s}}}\right) \right\rfloor \qquad (A6)$$

represents the chordwise aerodynamic mode shapes, and

$$\{\eta^{\bar{s}1}\} = \begin{Bmatrix} a_1 \\ a_2 \\ \vdots \\ a_g \\ \vdots \\ a_G \end{Bmatrix} \qquad (A7)$$

is the aerodynamic modal participation vector.

The downwash at $\bar{x}$ can be written as

$$w^{\bar{s}n}(\bar{x},\bar{z},t) \simeq \left[\frac{\partial}{\partial t} + V_{\bar{s}}\left\{\frac{\partial}{\partial \bar{x}} + \tan\Lambda\,\frac{\partial}{\partial \bar{z}}\right\}\right] u^{\bar{s}n}(\bar{x},\bar{z},t), \quad (A8)$$

where $V_{\bar{s}}$ is the chordwise cascade relative inflow velocity directed along CA.

Substituting for $u^{\bar{s}n}$ from equation (A5), the downwash can be written as

$$w^{\bar{s}n} = V_{\bar{s}}\left[\left[\left(ik_{\bar{s}} + \tan\Lambda\cdot\frac{\partial \ell_{\bar{s}}}{\partial \bar{z}}\right)\left[\Phi^{\bar{s}}\right] + \ell_{\bar{s}}\left[\frac{\partial \Phi^{\bar{s}}}{\partial \bar{x}}\right]\right]\{\eta^{\bar{s}1}\}\right.$$
$$\left. + \ell_{\bar{s}}\tan\Lambda\left[\Phi^{\bar{s}}\right]\{\eta^{\bar{s}2}\}\right] e^{i\omega t}, \quad (A9)$$

where

$$\{\eta^{\bar{s}2}\} = \left\{\frac{\partial \eta^{\bar{s}1}}{\partial \bar{z}}\right\}, \quad (A10)$$

and the reduced frequency

$$k_{\bar{s}} = \omega\,\ell_{\bar{s}} / V_{\bar{s}} . \quad (A11)$$

Corresponding to the downwash boundary conditions associated with each of the elements of the modal participation vector $\eta^{\bar{s}1}$ and its derivative $\eta^{\bar{s}2}$, the modified 2-d supersonic cascade unsteady aerodynamics program computes the pressures on $\bar{y}_-$ and $\bar{y}_+$ surfaces at P discrete points distributed along the chord $\bar{s}$. (The contribution due to the variation of the perturbation velocity potential in the $\bar{z}$ direction is neglected.) The distributions of these P points on the $\bar{y}_-$ and

$\overline{y}_+$ surfaces of the chord are distinct in general. Hence, the supersonic aerodynamics program has been modified to compute the required nett airloads as the algebraic differences of those computed based on pressures on $\overline{y}_-$ and $\overline{y}_+$ surfaces individually. For clarity of presentation and understanding, however, the following derivation continues in terms of differential pressures. The physical differential pressure at these P points can then be found from

$$\{p^{\bar{s}}\} = \{p^{\bar{s}}_{\overline{y}_-}\} - \{p^{\bar{s}}_{\overline{y}_+}\} = \frac{1}{2}\rho_{\bar{s}} V_{\bar{s}}^2 \left[[\psi^{\bar{s}1}_{pg}]\{\eta^{\bar{s}1}\} + [\psi^{\bar{s}2}_{pg}]\{\eta^{\bar{s}2}\}\right] e^{i\omega t} \quad (A12)$$

In order to be consistent with the subsonic development (Ref. 6) in integrating the pressures along the chord, the modal differential pressures are rewritten as

$$\left.\begin{aligned} [\psi^{\bar{s}1}_{pg}] &= [\Pi_{pp}][C^1_{gp}]^T, \text{ and} \\ [\psi^{\bar{s}2}_{pg}] &= [\Pi_{pp}][C^2_{gp}]^T, \end{aligned}\right\} \quad (A13)$$

where

$$[\Pi_{pp}] = \begin{bmatrix} 1 & 0 & 0 & \cdots & 0 \\ 1 & \frac{\bar{x}_2}{\ell_{\bar{s}}} & \sin\left(\frac{\overline{3-2}\cdot\pi\cdot\bar{x}_2}{2\ell_{\bar{s}}}\right) & \cdots & \sin\left(\frac{\overline{P-2}\cdot\pi\cdot\bar{x}_2}{2\ell_{\bar{s}}}\right) \\ 1 & \frac{\bar{x}_3}{\ell_{\bar{s}}} & \sin\left(\frac{\overline{3-2}\cdot\pi\cdot\bar{x}_3}{2\ell_{\bar{s}}}\right) & \cdots & \sin\left(\frac{\overline{P-2}\cdot\pi\cdot\bar{x}_3}{2\ell_{\bar{s}}}\right) \\ \vdots & \vdots & \vdots & \cdots & \vdots \\ \vdots & \vdots & \vdots & \cdots & \vdots \\ 1 & \frac{\bar{x}_P}{\ell_{\bar{s}}} & \sin\left(\frac{\overline{3-2}\cdot\pi\cdot\bar{x}_P}{2\ell_{\bar{s}}}\right) & \cdots & \sin\left(\frac{\overline{P-2}\cdot\pi\cdot\bar{x}_P}{2\ell_{\bar{s}}}\right) \end{bmatrix}. \quad (A14)$$

A.5 GENERALIZED AIRFORCE MATRICES FOR CHORDWISE AERODYNAMIC MODES

The differential pressures are estimated at P points along the chord (equation A12). The physical displacement at these P points can be written using equation (A5) as

$$\{u^{\bar{s}n}\} = \ell_{\bar{s}} \left[\Phi^{\bar{s}}_{pg}\right]\{\eta^{\bar{s}1}\} \quad . \tag{A15}$$

The virtual work done by the aerodynamic forces, acting on the blade strip associated with the chord $\bar{s}$, through a virtual displacement $\delta\{u^{\bar{s}n}\}$ becomes

$$\delta W^{\bar{s}} = \int_{\bar{x}=0}^{2\ell_{\bar{s}}} \delta u^{\bar{s}n} \cdot p^{\bar{s}} \cdot \left(C^{\bar{s}1}\bar{x} + C^{\bar{s}2}\right) \cdot d\bar{x} \tag{A16}$$

$$= \tfrac{1}{2}\rho_{\bar{s}} V_{\bar{s}}^2 \ell_{\bar{s}}^3 \delta\lfloor\eta^{\bar{s}1}\rfloor \left[\Phi^{\bar{s}}_{pg}\right]^T \lceil W \rceil \left[\Pi_{pp}\right]\left(\left[C^1_{gp}\right]^T\{\eta^{\bar{s}1}\} + \left[C^2_{gp}\right]^T\{\eta^{\bar{s}2}\}\right), \tag{A17}$$

where

$$\lceil W \rceil = \begin{bmatrix} \left[C^{\bar{s}1}\frac{\bar{x}_1}{\ell_{\bar{s}}} + \frac{C^{\bar{s}2}}{\ell_{\bar{s}}}\right]\left[\Delta\frac{\bar{x}_1}{\ell_{\bar{s}}}\right] & & 0 \\ & \left[C^{\bar{s}1}\frac{\bar{x}_2}{\ell_{\bar{s}}} + \frac{C^{\bar{s}2}}{\ell_{\bar{s}}}\right]\left[\Delta\frac{\bar{x}_2}{\ell_{\bar{s}}}\right] & \\ & & \ddots \\ 0 & & \left[C^{\bar{s}1}\frac{\bar{x}_p}{\ell_{\bar{s}}} + \frac{C^{\bar{s}2}}{\ell_{\bar{s}}}\right]\left[\Delta\frac{\bar{x}_p}{\ell_{\bar{s}}}\right] \end{bmatrix} \tag{A18}$$

$$= C^{\bar{s}1}\lceil W^2 \rceil + \frac{C^{\bar{s}2}}{\ell_{\bar{s}}}\lceil W^1 \rceil \quad . \tag{A19}$$

Substituting for $\lceil W \rceil$ in equation (A17),

$$\delta W^{\bar{s}} = \tfrac{1}{2}\rho_{\bar{s}} V_{\bar{s}}^2 \ell_{\bar{s}}^3 \delta\lfloor\eta^{\bar{s}1}\rfloor \left(\left[A^{\bar{s}1}_{gg}\right]\{\eta^{\bar{s}1}\} + \left[A^{\bar{s}2}_{gg}\right]\{\eta^{\bar{s}2}\}\right), \tag{A20}$$

whereby the generalized chordwise aerodynamic force matrices are

$$\left.\begin{aligned} [A^{\bar{s}1}_{gg}] &= [I^{\bar{s}}_{gp}][C^{1}_{gp}]^T \text{ , and} \\ [A^{\bar{s}2}_{gg}] &= [I^{\bar{s}}_{gp}][C^{2}_{gp}]^T \text{ ,} \end{aligned}\right\} \quad (A21)$$

$$\text{with} \quad \left.\begin{aligned} [I^{\bar{s}}_{gp}] &= C^{\bar{s}1}[I^{2}_{gp}] + \frac{C^{\bar{s}2}}{\ell_{\bar{s}}}[I^{1}_{gp}] \text{ ,} \\ [I^{2}_{gp}] &= [\Phi^{\bar{s}}_{pg}]^T [W^{2}][\Pi_{pp}] \text{ , and} \\ [I^{1}_{gp}] &= [\Phi^{\bar{s}}_{pg}]^T [W^{1}][\Pi_{pp}] \text{ .} \end{aligned}\right\} \quad (A22)$$

Elements of matrices I^{2}_{gp} and I^{1}_{gp} have been evaluated as chordwise integrals, and are presented in Appendix B.

A.6 TRANSFORMATION BETWEEN AERODYNAMIC AND STRUCTURAL MODAL COORDINATES

Equation (A5) can be used to express the normal displacement at the G structural grid points on chord $\bar{s}$ as

$$\{u^{\bar{s}n}\} = \ell_{\bar{s}} [\Phi^{\bar{s}}_{gg}]\{\eta^{\bar{s}1}\} \text{ .} \quad (A23)$$

In terms of structural modal coordinates, $u^{\bar{s}n}$ can also be written as

$$\{u^{\bar{s}n}\} = [\phi^{\bar{s}n,\underline{local}}_{gi}]\{\xi_i\} \text{ .} \quad (A24)$$

Comparison of equation (A23) with equation (A24) yields

$$\{\eta^{\bar{s}1}\} = \frac{1}{\ell_{\bar{s}}} \left[\Phi^{\bar{s}}_{gg}\right]^{-1} \left[\phi^{\bar{s}n,\underline{local}}_{gi}\right]\{\xi_i\} , \tag{A25}$$

$$= \frac{1}{\ell_{\bar{s}}} \left[G^{\bar{s}1}_{gi}\right]\{\xi_i\} . \tag{A26}$$

Differentiation with respect to $\bar{z}$ results in

$$\left\{\frac{\partial \eta^{\bar{s}1}}{\partial \bar{z}}\right\} = \{\eta^{\bar{s}2}\} = \frac{1}{\ell_{\bar{s}}}\left[-\frac{1}{\ell_{\bar{s}}}\cdot\frac{\partial \ell_{\bar{s}}}{\partial \bar{z}}\left[G^{\bar{s}1}_{gi}\right] + \left[G^{\bar{s}2}_{gi}\right]\right]\{\xi_i\} , \tag{A27}$$

where

$$\left[G^{\bar{s}2}_{gi}\right] = \left[\Phi^{\bar{s}}_{gg}\right]^{-1}\left[\frac{\partial}{\partial \bar{z}}\phi^{\bar{s}n,\underline{local}}_{gi}\right] . \tag{A28}$$

The modal displacement matrix $\phi^{\bar{s}n,\underline{local}}$ and its derivative $\frac{\partial}{\partial \bar{z}}\phi^{\bar{s}n,\underline{local}}$ are derived from the global modal matrix ϕ as follows:

$$\left[\phi^{\bar{s}n,\underline{local}}_{gi}\right] = \left[G^{\bar{s}n1}_{gg'}\right]\left[\phi^{\bar{s}1,\underline{global}}_{g'i}\right] , \tag{A29}$$

where each of the i modal columns of $\phi^{\bar{s}1,\underline{global}}$ consists of the three <u>modal translations</u> at each of the G computing station grid points on the chord $\bar{s}$.

The transformation $G^{\bar{s}n1}$ is given by

$$[G^{\bar{s}n1}_{gg'}] = \begin{bmatrix} 0 & 1 & 0 \\ 0 & 1 & 0 \\ & \vdots & \\ & \vdots & \\ & \vdots & \\ 0 & 1 & 0 \end{bmatrix} \left[[T^{bl}_{\bar{s}}] \,\middle|\, [T^{bl}_{\bar{s}}] \,\middle|\, \cdots \,\middle|\, [T^{bl}_{\bar{s}}] \right] \begin{bmatrix} [T^{bg}_{\bar{s}1}]^T & & & & \\ & [T^{bg}_{\bar{s}2}]^T & & & \\ & & \ddots & & \\ & & & [T^{bg}_{\bar{s}g}]^T & \\ & & & & \ddots \\ & & & & [T^{bg}_{\bar{s}G}]^T \end{bmatrix} \quad \text{(A30)}$$

where T^{bl} and T^{bg} represent the coordinate transformations from the NASTRAN basic system to the local (chord) $\bar{x}\bar{y}\bar{z}$ system and the global (displacement) system, respectively.

Similarly,

$$\left[\frac{\partial}{\partial \bar{s}} \phi^{\bar{s}n,\underline{local}}_{gi} \right] = \left[G^{\bar{s}n2}_{gg'} \right] \left[\phi^{\bar{s}2,\underline{global}}_{g'i} \right] , \qquad \text{(A31)}$$

where each of the i modal columns of $\phi^{\bar{s}2,\underline{global}}$ consists of the three <u>modal rotations</u> at each of the G computing station grid points on the chord $\bar{s}$.

The transformation $G^{\bar{s}n2}$ is given by

$$[G^{\bar{s}n2}_{gg'}] = -m_1 \begin{bmatrix} 1 & 0 & 0 \\ 1 & 0 & 0 \\ \vdots & & \\ 1 & 0 & 0 \end{bmatrix} \left[[T^{b\ell}_{\bar{s}}] \,\middle|\, [T^{b\ell}_{\bar{s}}] \,\middle|\, \cdots \,\middle|\, [T^{b\ell}_{\bar{s}}] \right] \begin{bmatrix} [T^{bg}_{\bar{s}1}]^T & & & & \\ & [T^{bg}_{\bar{s}2}]^T & & & \\ & & \ddots & & \\ & & & [T^{bg}_{\bar{s}g}]^T & \\ & & & & \ddots \\ & & & & [T^{bg}_{\bar{s}G}]^T \end{bmatrix}, \quad \text{(A32)}$$

where m_1 = 1 for right handed $\bar{x}\bar{y}\bar{z}$, and
= -1 for left handed $\bar{x}\bar{y}\bar{z}$. (A33)

A.7 GENERALIZED AIRFORCE MATRICES FOR CHORDWISE STRUCTURAL MODES

Introducing relations (A26) and (A27) in equation (A20), the virtual work expression for chord $\bar{s}$ becomes

$$\delta W^{\bar{s}} = \tfrac{1}{2} \rho_{\bar{s}} V_{\bar{s}}^2 \ell_{\bar{s}}^2 \delta L \{\xi_i\}^T [G^{\bar{s}1}_{gi}]^T \left[\frac{1}{\ell_{\bar{s}}} [A^{\bar{s}1}_{gg}][G^{\bar{s}1}_{gi}] + \frac{1}{\ell_{\bar{s}}} [A^{\bar{s}2}_{gg}] \left(-\frac{1}{\ell_{\bar{s}}} \frac{\partial \ell_{\bar{s}}}{\partial \bar{z}} [G^{\bar{s}1}_{gi}] + [G^{\bar{s}2}_{gi}] \right) \right] \{\xi_i\}, \quad \text{(A34)}$$

whereby the generalized airforce matrices for chordwise structural modes can be obtained as

$$
\left.
\begin{aligned}
[Q_{ii}^{\bar{s}1}] &= \tfrac{1}{2}\rho_{\bar{s}}V_{\bar{s}}^2\ell_{\bar{s}}^2\cdot\frac{1}{\ell_{\bar{s}}}[G_{gi}^{\bar{s}1}]^T[A_{gg}^{\bar{s}1}][G_{gi}^{\bar{s}1}] = \tfrac{1}{2}\rho_{\bar{s}}V_{\bar{s}}^2\ell_{\bar{s}}^2[\bar{Q}_{ii}^{\bar{s}1}], \\
[Q_{ii}^{\bar{s}2}] &= \tfrac{1}{2}\rho_{\bar{s}}V_{\bar{s}}^2\ell_{\bar{s}}^2\cdot\frac{1}{\ell_{\bar{s}}}[G_{gi}^{\bar{s}1}]^T[A_{gg}^{\bar{s}2}]\left(-\frac{1}{\ell_{\bar{s}}}\cdot\frac{\partial\ell_{\bar{s}}}{\partial\bar{z}}[G_{gi}^{\bar{s}1}]+[G_{gi}^{\bar{s}2}]\right) \\
&= \tfrac{1}{2}\rho_{\bar{s}}V_{\bar{s}}^2\ell_{\bar{s}}^2[\bar{Q}_{ii}^{\bar{s}2}].
\end{aligned}
\right\} \quad (A35)
$$

Combining $Q^{\bar{s}1}$ and $Q^{\bar{s}2}$, the generalized airforce matrix for chord $\bar{s}$ is defined as

$$
\left.
\begin{aligned}
[Q_{ii}^{\bar{s}}] &= \tfrac{1}{2}\rho_{\bar{s},ref}V_{\bar{s},ref}^2\left(\frac{\frac{1}{2}\rho_{\bar{s}}V_{\bar{s}}^2\ell_{\bar{s}}^2}{\frac{1}{2}\rho_{\bar{s},ref}V_{\bar{s},ref}^2}\right)\left([\bar{Q}_{ii}^{\bar{s}1}]+[\bar{Q}_{ii}^{\bar{s}2}]\right), \\
&= \tfrac{1}{2}\rho_{\bar{s},ref}V_{\bar{s},ref}^2[\bar{Q}_{ii}^{\bar{s}}].
\end{aligned}
\right\} \quad (A36)
$$

A.8 BLADE GENERALIZED AIRFORCE MATRIX

The virtual work done by the aerodynamic forces on the blade is the sum total of the virtual work done by all the chordwise aerodynamic forces on their respective strips. Thus

$$
\begin{aligned}
\delta W^{blade} &= \sum_{\bar{s}=1}^{\bar{S}}\delta W^{\bar{s}} \\
&= \tfrac{1}{2}\rho_{\bar{s},ref}V_{\bar{s},ref}^2\sum_{\bar{s}}\delta L\}_i^T[\bar{Q}_{ii}^{\bar{s}}]\{\}_i\}, \qquad (A37)
\end{aligned}
$$

whereby the generalized airforce matrix for the swept blade of the advanced turbopropeller can be written as

$$
[Q_{ii}^{blade}] = \tfrac{1}{2}\rho_{\bar{s},ref}V_{\bar{s},ref}^2\sum_{\bar{s}=1}^{\bar{S}}[\bar{Q}_{ii}^{\bar{s}}] = \tfrac{1}{2}\rho_{\bar{s},ref}V_{\bar{s},ref}^2[\bar{Q}_{ii}]. \qquad (A38)
$$

APPENDIX B

CHORDWISE WEIGHTING MATRICES (SUPERSONIC)

The chordwise weighting matrices I^2_{gp} and I^1_{gp} appearing in equations (A22) of Appendix A are evaluated.

1. $[I^2_{gp}] = [\Phi^{\bar{s}}_{pg}]^T [W^2] [\Pi_{pp}]$

$$= \begin{bmatrix} I_x & I_{x^2} & I_{x\cdot\overline{3-2}} & \cdots & I_{x\cdot\overline{P-2}} \\ I_{x^2} & I_{x^3} & I_{x^2\cdot\overline{3-2}} & \cdots & I_{x^2\cdot\overline{P-2}} \\ I_{x\cdot\overline{3-2}} & I_{x^2\cdot\overline{3-2}} & I_{x\cdot\overline{3-2}\cdot\overline{3-2}} & \cdots & I_{x\cdot\overline{3-2}\cdot\overline{P-2}} \\ \vdots & \vdots & \vdots & \vdots & \vdots \\ I_{x\cdot\overline{G-2}} & I_{x^2\cdot\overline{G-2}} & I_{x\cdot\overline{G-2}\cdot\overline{3-2}} & \cdots & I_{x\cdot\overline{G-2}\cdot\overline{P-2}} \end{bmatrix}.$$

The six typical elements of I^2_{gp} are as follows, with $y = \bar{x}/\ell_{\bar{s}}$:

a) $I_x = \int_0^2 y \, dy = 2$

b) $I_{x^2} = \int_0^2 y^2 \, dy = 8/3$

c) $I_{x \cdot \overline{r-2}} = \int_0^2 y \cdot \sin\left(\frac{\overline{r-2} \cdot \pi}{2} y\right) dy$

$r > 2$

$$= \frac{4}{(r-2)\,\pi} (-1)^{\overline{r-2}+1} \quad , \quad r = 3, 4, \cdots$$

d) $I_{x^3} = \int_0^2 y^3 \, dy = 4$

e) $I_{x^2 \cdot \overline{r-2}} = \int_0^2 y^2 \cdot \sin\left(\frac{\overline{r-2} \cdot \pi}{2} y\right) dy$

$r > 2$

$$= -\frac{8}{(r-2)\,\pi} \quad , \quad r = 4, 6, 8, \cdots$$

$$= \frac{8}{(r-2)\,\pi} - \frac{32}{\left[\overline{r-2} \cdot \pi\right]^3} \quad , \quad r = 3, 5, 7, \cdots$$

f) $I_{x \cdot \overline{r-2} \cdot \overline{s-2}} = \int_0^2 y \cdot \sin\left(\frac{\overline{r-2} \cdot \pi}{2} y\right) \cdot \sin\left(\frac{\overline{s-2} \cdot \pi}{2} y\right) dy$

$r > 2$

$s > 2$

$$= 1 \quad , \quad r = s$$

$$= 0 \quad , \; r \neq s \quad \text{and} \quad (r+s) \text{ even}$$

$$= - \frac{16\,(r-2)(s-2)}{\pi^2 (r-s)^2 (r+s-4)^2} \quad .$$

2. $$I^1_{gp} = \left[\Phi^{\bar{s}}_{pg} \right]^T \left[W^1_{\sim} \right] \left[\Pi_{pp} \right]$$

$$= \begin{bmatrix} I_. & I_x & I_{\overline{3-2}} & \cdots & I_{\overline{P-2}} \\ I_x & I_{x^2} & I_{x \cdot \overline{3-2}} & \cdots & I_{x \cdot \overline{P-2}} \\ I_{\overline{3-2}} & I_{x \cdot \overline{3-2}} & I_{\overline{3-2} \cdot \overline{3-2}} & \cdots & I_{\overline{3-2} \cdot \overline{P-2}} \\ \vdots & \vdots & \vdots & \vdots & \vdots \\ I_{\overline{G-2}} & I_{x \cdot \overline{G-2}} & I_{\overline{G-2} \cdot \overline{3-2}} & \cdots & I_{\overline{G-2} \cdot \overline{P-2}} \end{bmatrix} .$$

The six typical elements of I^1_{gp} are as follows, with $y = \bar{x}/\ell_3$:

a) $$I_. = \int_0^2 dy = 2$$

b) I_x as given by typical element (a) of I^2_{gp} .

c) $$I_{\overline{r-2}} = \int_0^2 \sin\left(\frac{\overline{r-2} \cdot \pi}{2} y \right) dy$$

$r > 2$

$$= \frac{2}{(r-2)\,\pi}\left[1 - (-1)^{\overline{r-2}}\right], \quad r = 3, 4, 5, \ldots$$

d) I_{x^2} as given by typical element (b) of I^2_{gp}

e) $I_{x \cdot \overline{r-2}}$ $\quad r > 2$ as given by typical element (c) of I^2_{gp}

f) $I_{\overline{r-2} \cdot \overline{s-2}}$ $\quad r > 2$, $s > 2$

$$= \int_0^2 \sin\left(\frac{\overline{r-2} \cdot \pi}{2} y\right) \cdot \sin\left(\frac{\overline{s-2} \cdot \pi}{2} y\right) dy$$

$$= 1 \quad , \quad r = s$$

$$= 0 \quad , \quad r \neq s \; .$$

APPENDIX C

AERODYNAMIC EXCITATION PARAMETERS

C.1 GENERAL

Determination of inter-blade phase angles, excitation reduced frequencies, circumferential harmonic indices, and the relation between the cosine and sine components of applied airloads are described. All cases addressing the turbosystems with flexible or rigid hubs/disks placed in uniform or non-uniform inflow are considered.

C.2 INTER-BLADE PHASE ANGLES

The possible inter-blade angles are determined by factors concerning the nature of the imposed aerodynamic excitation. The following points are noted here to define the inter-blade phase angles:

1. At any given instant of time, equation (7) of Section 3 defines the relative velocity components at the leading edge point of any chord on the reference/modelled/n=1 blade. This blade is also identified in Figure 2.5.

2. At the same instant, the relative velocity components at the corresponding point on any other (say, $n_{th.}$) blade can also be obtained from equation (7), Section 3, when

a) $T_{\bar{s}}^{BL}$ is replaced by $T_{\bar{s}}^{BL,n}$ where

$$[T_{\bar{s}}^{BL,n}] = [T_{\bar{s}}^{BL}] \begin{bmatrix} 1 & 0 & 0 \\ 0 & \cos\eta & \sin\eta \\ 0 & -\sin\eta & \cos\eta \end{bmatrix}, \qquad (C1)$$

with

$$\eta = \frac{2\pi}{N}(n-1), \quad n = 1, 2, \ldots, N, \qquad (C2)$$

and

b) $\{WA\}$Tunnel and $O_B A$ are considered for the $n_{th.}$ blade.

3. Finally, the ratio of the oscillatory part of velocity component $VA_{\bar{y}}$ on the nth. blade to that on the (n+1)th. blade yields the inter-blade phase angle σ as

$$\frac{osc\ (VA)_{\bar{y}},\ n_{th.}\ blade}{osc\ (VA)_{\bar{y}},\ (n+1)_{th.}\ blade} = e^{i\sigma}. \qquad (C3)$$

This definition of σ is consistent with that of Ref. 12.

The above procedure is used in defining σ in each of the following cases.

C.3 RIGID HUB/DISK, UNIFORM INFLOW

Excitation Reduced Frequency

With the turbosystem axis of rotation misaligned at a small angle with the uniform inflow velocity, the only excitation frequency is given by

$$\omega = |\vec{\Omega}| \quad , \tag{C4}$$

where $\vec{\Omega}$ is the angular velocity of rotation of the turbosystem.

The corresponding reduced frequency for the blade is defined with any of its chords selected as reference:

$$k_{blade} = \frac{\omega \ell_{\bar{s},ref}}{V_{\bar{s},ref}} \quad , \tag{C5}$$

where $\ell_{\bar{s},ref}$ and $V_{\bar{s},ref}$ are the semi-chord and cascade relative inflow velocity, respectively, for the reference chord.

Reduced frequencies for other chords are scaled from the above blade value.

Inter-Blade Phase Angle

This is given by

$$\sigma_{blade} = -2\pi/N \quad , \tag{C6}$$

with N being the total number of cyclic segments in the structure.

Circumferential Harmonic Index

The only permissible value is 0 , together with the requirement that the degrees of freedom on the segment boundaries be constrained to zero.

Relation Between $\bar{P}^{kc}$ and $\bar{P}^{ks}$

These components of applied airloads are described in detail in Section 2.5. For the rigid hub/disk and uniform inflow case, $\bar{P}^{ks}$ is identically zero, and only $\bar{P}^{kc}$ exists.

C.4 RIGID HUB/DISK, NON-UNIFORM INFLOW

Excitation Reduced Frequency

The possible excitation frequencies are based on the circumferential harmonic contents of the spatially non-uniform inflow, and are given by

$$\omega = p \cdot |\vec{\Omega}| \quad , \tag{C7}$$

where p takes on the positive integer values of the above-mentioned inflow harmonics.

Reduced frequencies are as per equation (C5) with ω's from equation (C7).

Inter-Blade Phase Angle

Permissible inter-blade phase angles are obtained from $\sigma = -p \cdot 2\pi/N$. However, in order to conveniently determine the

associated structural circumferential harmonic index, especially in the flexible hub/disk non-uniform inflow case, the inter-blade phase angles are written as follows:

$$\left.\begin{aligned} k_L' &= (N-1)/2 \quad , \ N \text{ odd} \ , \\ &= N/2 \quad , \ N \text{ even} \ . \end{aligned}\right\} \qquad (C8)$$

$$\left.\begin{aligned} &\text{For} \quad 0 < p \leq k_L' \quad , \quad \sigma = -p \cdot 2\pi/N \ . \\ &\text{For} \quad k_L' + jN < p \leq k_L' + (j+1)N \ , \\ &\qquad \sigma = -p \cdot 2\pi/N + (j+1) \cdot 2\pi \ , \\ &\qquad j = 0, 1, 2, \cdots \ . \end{aligned}\right\} \qquad (C9)$$

Circumferential Harmonic Index

The only permissible value is 0, together with the requirement that the degrees of freedom on the segment boundaries be constrained to zero.

Relation Between $\bar{P}^{kc}$ and $\bar{P}^{ks}$

Only $\bar{P}^{kc}$ type loads exist.

C.5 FLEXIBLE HUB/DISK, UNIFORM INFLOW

Excitation Reduced Frequency

The only admissible frequency is

$$\omega = |\vec{\Omega}| \ , \qquad (C10)$$

with the reduced frequency given by equation (C5).

Inter-Blade Phase Angle

Only one inter-blade phase angle exists:

$$\sigma = -2\pi/N \tag{C11}$$

Circumferential Harmonic Index

The only possible index can be written as

$$k = |\sigma| / (2\pi/N) = 1 \tag{C12}$$

Relation Between $\bar{P}^{kc}$ and $\bar{P}^{ks}$

These two load components are related as

$$\bar{P}^{ks} = \pm i \, \bar{P}^{kc} \tag{C13}$$

where the + sign applies if $\sigma \leq 0$, and the - sign applies otherwise.

C.6 FLEXIBLE HUB/DISK, NON-UNIFORM INFLOW

Excitation Reduced Frequency

The possible excitation frequencies are

$$\omega = p \cdot |\vec{\Omega}| \quad , \qquad (C14)$$

where p is a positive integer reflecting the circumferential harmonic contents of the spatially non-uniform inflow.

Reduced frequencies, in turn, are obtained from equation (C5).

Inter-Blade Phase Angle

The permissible values are computed as per equations (C8) and (C9).

Circumferential Harmonic Index

For selected excitation harmonics p, the permissible circumferential harmonics representing the structural motion are given by

$$k = |\sigma| / (2\pi/N) \quad , \qquad (C15)$$

where σ's are from equations (C8) and (C9).

Relation Between $\bar{P}^{kc}$ and $\bar{P}^{ks}$

This is described by equation (C13).

REFERENCES

1. Elchuri, V., Smith, G.C.C., Gallo, A.M., and Dale, B.J., "NASTRAN Level 16 Theoretical, User's, Programmer's, and Demonstration Manuals Updates for Aeroelastic Analysis of Bladed Discs," NASA CR's 159823-159826, March 1980.

2. Smith, G.C.C., and Elchuri V., "Aeroelastic and Dynamic Finite Element Analysis of a Bladed Shrouded Disk," NASA CR 159728, March 1980.

3. Gallo, A. Michael, Elchuri, V., and Skalski, S.C., "Bladed-Shrouded-Disc Aeroelastic Analyses: Computer Program Updates in NASTRAN Level 17.7," NASA CR 165428, December 1981.

4. Elchuri, V., and Smith, G.C.C., "Finite Element Forced Vibration Analysis of Rotating Cyclic Structures," Final Technical Report, NASA CR 165430, December 1981.

5. Elchuri, V., Gallo, A.M., and Skalski, S.C., "Forced Vibration Analysis of Rotating Cyclic Structures in NASTRAN," NASTRAN Manuals, NASA CR 165429, December 1981.

6. Elchuri, V., and Smith. G.C.C., "NASTRAN Flutter Analysis of Advanced Turbopropellers," Final Technical Report, NASA CR 167926, April 1982.

7. Elchuri, V., Gallo, A.M., and Skalski, S.C., "NASTRAN Documentation for Flutter Analysis of Advanced

Turbopropellers," NASTRAN Manuals, NASA CR 167927, April 1982.

8. Elchuri, V., and Pamidi, P.R., "AIRLOADS: A Program for Oscillatory Airloads on Blades of Turbosystems in Spatially Non-Uniform Inflow," NASA CR 174968, July 1985.

9. Elchuri, V., and Pamidi, P.R., "NASTRAN Supplemental Documentation for Modal Forced Vibration Analysis of Aerodynamically Excited Turbosystems," NASA CR 174967, July 1985.

10. Rao, B.M., and Jones, W.P., "Unsteady Airloads for a Cascade of Staggered Blades in Subsonic Flow," 46th Propulsion Energetics Review Meeting, Monterey, California, September 1975.

11. Adamczyk, J.J., and Goldstein, M.E., "Unsteady Flow in a Supersonic Cascade with Subsonic Leading-Edge Locus," AIAA Journal, Vol. 16, No. 12, December 1978, pp. 1248-1254.

12. Kielb, R.E., and Kaza, K.R.V., "Aeroelastic Characteristics of a Cascade of Mistuned Blades in Subsonic and Supersonic Flows," NASA TM 82631, September 1981.

SYMBOLS

A	Chordwise aerodynamic matrix for aerodynamic modes
B	Damping matrix
B_1	Coriolis acceleration coefficient matrix
C	Matrix of modal pressure coefficients, constants
c	Chord
G	Transformation matrix
g	Structural damping
I	Chordwise weighting matrix
i	$\sqrt{-1}$
K	Stiffness matrix
k	Circumferential harmonic index, reduced frequency
l	Semichord
M	Mass matrix, cascade relative inflow Mach number
M_1	Centripetal acceleration coefficient matrix
N	Number of blades on turbosystem
n	n_{th} cyclic sector
P	Load vector
Q	Aerodynamic coefficient matrix for structural modes
T	Transformation matrix
t	Time
u	Physical degrees of freedom
V	Cascade relative inflow velocity
W	Virtual work, weighting matrix
w	Strip width, downwash velocity
$\bar{x},\bar{y},\bar{z}$	Chord local coordinates

γ	Inclination angle of turbosystem axis of rotation
η	Aerodynamic modal coordinates
Λ	Sweep angle
λ	Stagger angle
ζ	Structural modal coordinates
ρ	Mass density of flow
σ	Inter-blade phase angle
Φ	Chordwise aerodynamic modes
ϕ	Structural modes
Ψ	Pressure distribution in aerodynamic modes
Ω	Rotational speed
ω	Circular frequency

Subscripts

g	Grid point on chord, chordwise aerodynamic mode
i	Structural mode
p	Cascade theory pressure point
$\bar{s}$	Chord $\bar{s}$

Superscripts

B,b	Basic coordinate system
G,g	Global coordinate system
K	Independent solution set in 'symmetric components'
L,l	Local coordinate system
n	$n_{th.}$ cyclic sector , normal to chord
$\bar{s}$	Chord $\bar{s}$

-o
-kc
-ks
-N/2

} Fourier coefficients ('symmetric components')

1. Report No.	2. Government Accession No.	3. Recipient's Catalog No.
NASA CR 174966		

4. Title and Subtitle	5. Report Date
Modal Forced Vibration Analysis of Aerodynamically Excited Turbosystems	6. Performing Organization Code
7. Author(s)	8. Performing Organization Report No.
V. Elchuri	10. Work Unit No.
9. Performing Organization Name and Address	11. Contract or Grant No.
Aerostructures, Inc. 1225 Jeff. Davis Hwy., Suite 512 Arlington, VA 22202	NAS3-24387
12. Sponsoring Agency Name and Address	13. Type of Report and Period Covered
NASA Lewis Research Center 21000 Brookpark Road Cleveland, OH 44135	14. Sponsoring Agency Code

15. Supplementary Notes

16. Abstract

Theoretical aspects of a new capability to determine the vibratory response of turbosystems subjected to aerodynamic excitation are presented.

Turbosystems such as advanced turbopropellers with highly swept blades, and axial-flow compressors and turbines can be analyzed using this capability. The capability has been developed and implemented in the April 1984 release of the general purpose finite element program NASTRAN.

The dynamic response problem is addressed in terms of the normal modal coordinates of these tuned rotating cyclic structures. Both rigid and flexible hubs/disks are considered. Coriolis and centripetal accelerations, as well as differential stiffness effects are included.

Generally non-uniform steady inflow fields and uniform flow fields arbitrarily inclined at small angles with respect to the axis of rotation of the turbosystem are considered as the sources of aerodynamic excitation. The spatial non-uniformities are considered to be small deviations from a principally uniform inflow. Subsonic and supersonic relative inflows are addressed, with provision for linearly interpolating transonic airloads.

17. Key Words (Suggested by Author(s))	18. Distribution Statement
Forced Vibrations, Aerodynamic Excitation, Turbosystems, NASTRAN, Finite Elements, Rotating Cyclic Structures	

19. Security Classif. (of this report)	20. Security Classif. (of this page)	21. No. of pages	22. Price*